



Caique Diego de Abreu Lima

**Structural and Magnetic Study of the α -MoO₃: Effects of Doping and
Structural Defect**

Tese de doutorado

Thesis presented to the Programa de Pós-graduação em Física of PUC-Rio in partial fulfillment of the requirements for the degree of Doutor em Ciências - Física.

Advisor: Prof. Jefferson Ferraz Damasceno Félix Araújo

Co-advisor: Prof. Cleânio da Luz Lima

Rio de Janeiro

February 2025



Caique Diego de Abreu Lima

**Structural and Magnetic Study of the α -MoO₃: Effects of Doping and
Structural Defect**

Thesis presented to the Programa de Pós-graduação em Física of PUC-Rio in partial fulfillment of the requirements for the degree of Doutor em Ciências - Física. Approved by the Examination Committee:

Prof. Jefferson Ferraz Damasceno Félix Araújo

Advisor

Departamento de Física – PUC-Rio

Prof. Cleânio da Luz da Lima

Co-advisor

UFPI

Dra. Anna De Falco

Rensselaer Polytechnic Institute

Prof. Paulo de Tarso Cavalcante Freire

UFC

Prof. João Victor Barbosa Moura

UFMA

Prof. Walmir Eno Pottker

UTFPR

Prof. Marcelo Eduardo Huguenin Maia da Costa

Departamento de Física – PUC-Rio

Rio de Janeiro, February 26th, 2025

All rights reserved

Caique Diego de Abreu Lima

Graduated in physics (2019) and obtained his M.Sc. Degree in Physics (2021), both from the Universidade Federal do Piauí.

Bibliographic data

Lima, Caique

Structural and Magnetic Study of α -MoO₃: Effects of Doping and Structural Defect / Caique Diego de Abreu Lima; orientador: Jefferson Ferraz Damasceno Félix Araújo. – 2025; co-advisor: Cleânio da Luz Lima.

94 f: il. color.; 30 cm

Tese (doutorado) - Pontifícia Universidade Católica do Rio de Janeiro, Departamento de Informática, 2025.

Inclui bibliografia

1. Física – Teses. 2. α -MoO₃. 3. magnetic properties. 4. structural defects. 5. Paramagnetic. 6. diamagnetic. I. Araújo, Jefferson. II. Pontifícia Universidade Católica do Rio de Janeiro. Departamento de Física. III. Título.

CDD: 004

To my parents, for their support and
encouragement.

Acknowledgments

The completion of this thesis marks the culmination of a challenging academic journey, and several people contributed to making this moment possible. To each of them, I express my deepest gratitude.

First and foremost, I want to express my gratitude to my advisors, Jefferson Ferraz Damasceno Felix Araujo and Cleânio da Luz Lima, for their guidance, support and patience throughout the entire process. Their contributions were essential to the creation of this work, and their wise counsel guided me in the proper path.

I am thankful to my family and friends for always being there for me, showing me love, support, and empathy. To my parents, Maria Santana and Francisco Lima, in particular, for their unwavering support and belief in my abilities throughout my academic and personal lives.

I also want to express my gratitude to my lab/course colleagues for their intellectual talks, experience sharing, and support during challenging times. This journey was a lot simpler and more motivating because of you all.

Lastly, I would like to express my gratitude to Universidade Federal do Piauí (UFPI) and Pontifícia Universidade Católica do Rio de Janeiro (PUC-Rio), which gave me the tools and assistance I needed to carry out this work.

This study was financed in part by the Coordenação de Aperfeiçoamento de Pessoal de Nível Superior - Brasil (CAPES) - Finance Code 001

I sincerely thank each and every one of them.

Abstract

Lima, Caique; Araújo, Jefferson. **Structural and Magnetic Study of α -MoO₃: Effects of Doping and Structural Defect**. Rio de Janeiro, 2025. 94p. Tese de Doutorado – Departamento de Física, Pontifícia Universidade Católica do Rio de Janeiro.

This work presents a study on the structural and magnetic properties of molybdenum trioxide (MoO₃), both in its pure form and doped with iron (Fe), with the aim of expanding its industrial applications. The main goal is to enhance its magnetic properties through doping and the control of structural defects. The study is divided into three parts. In the first part, a structural and magnetic study of Fe-doped MoO₃ was conducted. The material was produced by the solid-state reaction method, involving the thermal decomposition of ammonium molybdate and mixing it with different concentrations of Fe. The resulting samples were characterized by Raman, SEM, FTIR, and XRD, confirming the orthorhombic phase. The magnetic properties were analyzed using VSM, revealing an unusual behavior in the hysteresis curve. To further investigate this phenomenon, MoO₃ was synthesized in a furnace, allowing precise control of environmental conditions, pressure, and temperature to regulate the material's structural defects. The second part of the study investigates the optimal environmental and temperature conditions for the formation of MoO₃ with different structural defects while maintaining phase purity and preventing the formation of secondary phases. Syntheses were carried out in O₂, H₂, and Ar atmospheres at temperatures of 450, 550, and 650 °C, and the samples were characterized using the same techniques as before. The results showed that secondary phases formed in H₂ and Ar atmospheres, while the material remained pure in the O₂ environment throughout the process. Finally, in the third part, MoO₃ was synthesized in an O₂ atmosphere, with variations in time and temperature, to obtain samples with different levels of structural defects. The samples, synthesized using the same method as in the second part, were characterized by Raman spectroscopy, FTIR, XRD, and XPS, and their magnetic properties were studied using VSM. The results indicated that variations in the number of structural defects among the samples are directly related to their magnetic properties, which may explain the atypical behavior observed in this material.

Keywords

α -MoO₃; magnetic properties; structural defects; paramagnetic; diamagnetic.

Resumo

Lima, Caique; Araújo, Jefferson. **Estudo Estrutural e Magnético do α -MoO₃: Efeitos de Dopagem e Defeitos Estrutural**. Rio de Janeiro, 2025. 94p. Tese de Doutorado – Departamento de Informática, Pontifícia Universidade Católica do Rio de Janeiro.

Este trabalho apresenta um estudo das propriedades estruturais e magnéticas do trióxido de molibdênio (MoO₃), tanto em sua forma pura quanto dopada com ferro (Fe), visando ampliar suas aplicações industriais. O principal objetivo é melhorar suas propriedades magnéticas por meio da dopagem e do controle de defeitos estruturais. O estudo está dividido em três partes. Na primeira parte, foi realizado um estudo estrutural e magnético do MoO₃ dopado com Fe. O material foi produzido pelo método de reação no estado sólido, envolvendo a decomposição térmica do molibdato de amônia e a mistura com diferentes concentrações de Fe. As amostras resultantes foram caracterizadas por Raman, MEV, FTIR e DRX, confirmando a fase ortorrômbica. As propriedades magnéticas foram analisadas por VSM, revelando um comportamento incomum na curva de histerese. Para investigar melhor esse fenômeno, o MoO₃ foi sintetizado em um forno, permitindo controle preciso das condições de ambiente, pressão e temperatura, a fim de controlar os defeitos estruturais. Na segunda parte, foram investigadas as condições ideais de ambiente e temperatura para a formação do MoO₃ com diferentes defeitos estruturais, mantendo a pureza da fase e evitando a formação de fases secundárias. As sínteses foram realizadas em atmosferas de O₂, H₂ e Ar, com temperaturas de 450, 550 e 650°C, sendo as amostras caracterizadas pelas mesmas técnicas mencionadas anteriormente. Os resultados mostraram que, enquanto nos ambientes de H₂ e Ar houve a formação de fases secundárias, no ambiente de O₂ o MoO₃ permaneceu puro em todo o processo. Na terceira parte, o MoO₃ foi sintetizado em atmosfera de O₂ com variações de tempo e temperatura para gerar amostras com diferentes graus de defeitos estruturais. As amostras, sintetizadas com o mesmo método da segunda parte, foram caracterizadas por espectroscopia Raman, FTIR, DRX e XPS, e as propriedades magnéticas foram novamente analisadas por VSM. Os resultados indicaram que as variações na quantidade de defeitos estruturais entre as amostras estão diretamente relacionadas às suas propriedades magnéticas, o que pode explicar o comportamento atípico observado nesse material.

Palavras-chave

α -MoO₃; propriedades magnéticas; defeitos estruturais; paramagnético; diamagnético.

Table of contents

1.1	Mo and MoO ₃	16
1.2	Structure and Oxygen Vacancies	17
1.3	MoO ₃ properties	19
1.4	Synthesis	21
1.5	Thesis outline	23
2.	Synthesis and magnetic characterization of iron-doped molybdenum trioxide (α -MoO ₃ :xFe) [81]	26
2.1	Synthesis	26
2.2	Results and discussion	26
2.2.1	X-ray Diffraction (XRD)	26
2.2.2	Scanning electron microscopy (SEM)	28
2.2.3	Raman spectroscopy	32
2.2.4	Fourier Transform Infrared spectroscopy (FTIR)	34
2.2.5	Magnetic Properties at Room Temperature	36
2.3	Final considerations	38
3	Influence of Temperature and Gas Atmosphere on the Thermal Decomposition of (NH ₄) ₆ Mo ₇ O ₂₄ •4H ₂ O [82]	39
3.1	Synthesis	39
3.2	Results and discussion	39
3.2.1	X-ray Diffraction (XRD)	39
3.2.2	Raman spectroscopy	42
3.2.3	Fourier Transform Infrared spectroscopy (FTIR)	45
3.2.4	Vibrating-sample magnetometer (VSM)	47
3.3	Final considerations	48
4	Investigating Paramagnetic to Diamagnetic Transition in MoO ₃ : Controlled Synthesis and Characterization	50
4.1	Synthesis	50
4.2	Results and discussion	50
4.2.1	X-ray Diffraction (XRD)	50
4.2.2	X-ray photoelectron spectroscopy (XPS)	52
4.2.3	Fourier Transform Infrared spectroscopy (FTIR)	55
4.2.3	Raman spectroscopy	56
4.2.4	Vibrating-sample magnetometer (VSM)	58
4.3	Final considerations	59
5	Conclusion and Future Perspectives	61

5.1 Conclusion.....	61
5.2 Future Perspectives.....	62
6 References	63
7 Appendix	77
Appendix A: Raman	77
Appendix B: XRD	81
Appendix C: Magnetic properties	87
Appendix D: XPS	92
Appendix F: Additional References	93

List of figures

Figure 1: Molybdenum trioxide structures: (a) α -MoO ₃ , (b) β -MoO ₃ , (c) h-MoO ₃	17
Figure 2: Atomic structures (side view) are illustrated as follows: (a) the pristine MoO ₃ (001) surface, (b) the surface with an oxygen vacancy at the bridge site, and (c) a detailed view of the vacancy. The oxygen vacancy is indicated by the dashed blue circle.....	18
Figure 3: Unusual transition from paramagnetic to diamagnetic behavior. Figure adapted from: [70].	21
Figure 4: Synthesis methods commonly employed for the preparation MoO ₃ . Figure adapted from: [133].	22
Figure 5: X-ray diffraction patterns of α -MoO ₃ a) pure and Fe-doped samples. The inset shows the peaks of Fe ₂ (MoO ₄) ₃ . b) Comparison of positions peaks (110), (040), and (021) of the α -MoO ₃ phase. Figure taken from: [81]	27
Figure 6: High-magnification SEM images depicting the plate-like morphology of (a) pure MoO ₃ , (b) MoO ₃ :1%Fe, (c) MoO ₃ :3%Fe, and (d) MoO ₃ :5%Fe samples are presented. Additionally, SEM images illustrating the cuboid morphology of Fe ₂ (MoO ₄) ₃ in (e) MoO ₃ :1%Fe and (f) MoO ₃ :5%Fe samples are also shown. Figure taken from: [81].....	29
Figure 7: EDS spectra accompanied by images illustrating the elemental distribution of Mo, O, and Fe in (a) pure MoO ₃ , (b) MoO ₃ :1%Fe, (c) MoO ₃ :3%Fe, and (d) MoO ₃ :5%Fe samples are provided. To enhance visualization, the Fe-rich secondary phase, identified as Fe ₂ (MoO ₄) ₃ , has been highlighted using red dashed circles. Figure taken from: [81]	30
Figure 8: Punctual EDS of a) MoO ₃ -plate in MoO ₃ :1%Fe sample, b) Fe ₂ (MoO ₄) ₃ in MoO ₃ :1%Fe sample, c) MoO ₃ -plate in MoO ₃ :5%Fe sample and d) Fe ₂ (MoO ₄) ₃ in MoO ₃ :5%Fe sample. Figure taken from: [81].....	31
Table 1: The percentage of weight contributed by each element: Mo, O, and Fe, was determined through point measurements using EDS. Table taken from: [81].	31
Table 2: Raman peak positions were observed in each sample, along with their corresponding molecular assignments. Table taken from: [81].	32
Figure 9: (a) Raman spectra of pure and Fe-doped α -MoO ₃ , (b) decomposition analysis of Raman peaks for pure MoO ₃ , (c) intensity ratio of the 285/290 cm ⁻¹ peaks, and variations in peak width at (d) 666 cm ⁻¹ and (e) 995 cm ⁻¹ are presented. Figure taken from: [81].	33
Table 3: Ratio between the intensity of peaks at 285 and 290 cm ⁻¹ , and FWHM of peaks at 666 and 995 cm ⁻¹ . Table taken from: [81]:.....	34
Figure 10: FTIR spectra of pure and Fe-doped α -MoO ₃ . Figure taken from: [81].	35
Figure 11: a) Magnetic curves of Fe-doped molybdenum trioxide (MoO ₃) samples with varying iron concentrations of 0 (pure), 1, 3, and 5 %. The magnetic curves of b) the pure sample, c) MoO ₃ :1%Fe, and d) MoO ₃ :5%Fe are shown. Figure taken from: [81].	37
Figure 12: X-ray diffraction pattern of AHM_320 precursor sample. Figure taken from: [82]. .	40
Figure 13: XRD patterns of the synthesized samples in an O ₂ environment at (a) 450, (b) 550, and (c) 650 °C are shown. Additionally, XRD patterns of samples synthesized in an H ₂ environment at (d) 450, (e) 550, and (f) 650 °C, as well as in an inert Ar environment at (g) 450, (h) 550, and (i) 650 °C. Figure taken from: [82].	41
Table 4: Sample identification, goodness of fit, and weighted residual statistical parameters facilitates the identification of phases, the composition of which is determined within the sample, as well as COD card numbers. Table taken from: [82]:.....	42
Figure 14: Raman spectra of the precursor utilized in the secondary phase of the synthesis (AHM_320) and the synthesized samples in environments containing (b) O ₂ , (c) H ₂ , and (d) Ar. Figure taken from: [82].	43

Figure 15: comparison of the Raman spectra for samples O ₂ _550, H ₂ _550, and Ar_550, with emphasis on three specific regions, is provided: (1) the lattice region at 125–250 cm ⁻¹ , (2) the 285/290 cm ⁻¹ region at 230–330 cm ⁻¹ , and (3) the 820 cm ⁻¹ region at 790–860 cm ⁻¹ Figure taken from: [82].	45
Figure 16: FTIR spectra of the precursor utilized in the secondary phase of the synthesis (AHM_320) and the resulting samples in environments containing (b) O ₂ , (c) H ₂ , and (d) Ar. Figure taken from: [82].	46
Figure 17: Comparison of Raman spectra of the samples O ₂ _550, H ₂ _550, and Ar_550. Figure taken from: [82].	47
Figure 18: Magnetic curve of the samples O ₂ _550, H ₂ _550, and Ar_550. Figure taken from: [82].	48
Figure 19: XRD pattern of α-MoO ₃ of a) all samples and high magnification of b) (020) and c) (101) peaks. Figure taken from: [128].	51
Figure 20: XPS spectra for a) 525C_4h, b) 525C_8h, c) 625C_4h, and d) 625C_8h samples. Figure taken from: [128].	52
Figure 21: XPS spectra of Mo _{3d} and peaks decomposition for a) 525C_4h, b) 525C_8h, c) 625C_4h, and d) 625C_8h samples. Figure taken from: [128].	54
Table 5: The positions of the ionization states Mo ⁴⁺ , Mo ⁵⁺ , and Mo ⁶⁺ in the Mo _{3d} _{3/2} and Mo _{3d} _{5/2} peaks are observed at 231 and 236 eV, respectively. Table taken from: [128].	54
Table 6: concentration of the areas corresponding to the ionization states Mo ⁴⁺ , Mo ⁵⁺ , and Mo ⁶⁺ in the Mo _{3d} peak at 231 and 236 eV is expressed as a percentage. Table taken from: [128].	55
Figure 22: FTIR spectra of synthesized α-MoO ₃ . Figure taken from: [128].	56
Figure 23: Raman spectra of α-MoO ₃ , showing a) spectra of all samples and high magnification of regions b) 100-500 cm ⁻¹ and c) 600-1100 cm ⁻¹ , along with the corresponding phonon modes associated with each peak. Figure taken from: [128].	57
Table 7: ratio of peak intensities at 285 cm ⁻¹ and 290 cm ⁻¹ , as well as the full width at half maximum (FWHM) of the peaks at 668 cm ⁻¹ , were evaluated. Table taken from: [128].	57
Figure 24: Magnetic curve (M-H hysteresis curves) of samples. a) Empty sample holder used to measure the sample 525C_4h, b) measurement of sample holder + 525C_4h (S+SH_525C_4h), c) 525C_4h sample (S 525_4h) after subtracting the magnetization of the sample holder. Figure taken from: [128].	58

List of tables

Table 1: The percentage of weight contributed by each element: Mo, O, and Fe, was determined through point measurements using EDS. Table taken from: [81].	31
Table 2: Raman peak positions were observed in each sample, along with their corresponding molecular assignments. Table taken from: [81].	32
Table 3: Ratio between the intensity of peaks at 285 and 290 cm^{-1} , and FWHM of peaks at 666 and 995 cm^{-1} . Table taken from: [81].	34
Table 4: Sample identification, goodness of fit, and weighted residual statistical parameters facilitates the identification of phases, the composition of which is determined within the sample, as well as COD card numbers. Table taken from: [82].	42
Table 5: The positions of the ionization states Mo^{4+} , Mo^{5+} , and Mo^{6+} in the $\text{Mo}_{3d_{3/2}}$ and $\text{Mo}_{3d_{5/2}}$ peaks are observed at 231 and 236 eV, respectively.	54
Table 6: concentration of the areas corresponding to the ionization states Mo^{4+} , Mo^{5+} , and Mo^{6+} in the Mo_{3d} peak at 231 and 236 eV is expressed as a percentage.	55
Table 7: ratio of peak intensities at 285 cm^{-1} and 290 cm^{-1} , as well as the full width at half maximum (FWHM) of the peaks at 668 cm^{-1} , were evaluated.	57

List of Abbreviations and Symbols

α -MoO ₃	Alpha Molybdenum Trioxide
XRD	X-ray Diffraction
SEM	Scanning Electron Microscopy
FTIR	Fourier Transform Infrared Spectroscopy
VSM	Vibrating Sample Magnetometry
XPS	X-ray Photoelectron Spectroscopy
EDS	Energy Dispersive Spectroscopy
AHM	Ammonium Heptamolybdate
OV _s	Oxygen Vacancies
GOF	Goodness of Fit
COD	Crystallography Open Database
SCCM	Standard Cubic Centimeters per Minute
α	Alpha (Structural Phase)
β	Beta (Structural Phase)
h	Hexagonal (Structural Phase)
Mo	Molybdenum
O	Oxygen
Fe	Iron
MoO ₃	Molybdenum Trioxide
MoO ₂	Molybdenum Dioxide
Mo ⁶⁺	Molybdenum Ion in +6 Oxidation State
Mo ⁵⁺	Molybdenum Ion in +5 Oxidation State
Mo ⁴⁺	Molybdenum Ion in +4 Oxidation State
Σ	Summation
λ	Wavelength
θ	Angle (Used in XRD Analysis)
eV	Electron Volt (Energy Measurement)
O ₂ , H ₂ , Ar	Oxygen, Hydrogen, and Argon Gas Atmospheres

“Who looks outside, dreams; who looks inside, awakes.” (Carl Jung)

1 Introduction

The year 2024 is noteworthy for its significance in the context of climate issues. According to the European Union's Earth observation program, Copernicus, 2024 was identified as the hottest year on record for the planet [1]. This unprecedented rise in global temperatures is a direct consequence of the accelerating and intensifying impacts of climate change. The elevated temperatures had substantial ramifications for the environment and society, leading to an augmented frequency of extreme natural phenomena, including storms, floods, droughts, and protracted dry spells. These events have far-reaching consequences, impacting not only biodiversity and ecosystems but also directly affecting vulnerable populations worldwide.

According to the United Nations Refugee Agency (UNHCR), approximately five million individuals were compelled to seek refuge due to climate-related disasters in 2024 alone, representing a significant increase in displacement due to environmental degradation [2]. This phenomenon underscores the necessity for the development and implementation of public policies aimed at mitigating the adverse impacts of climate change and facilitating the adaptation of populations to these new realities. The outlook for 2025 is similarly disconcerting. Projections indicate that global temperatures will persist above average and may even exceed levels recorded in 2024. This scenario underscores the pressing need for the implementation of comprehensive, global strategies aimed at mitigating the effects of climate change and reducing the damage caused to the environment and the most affected.

The quest for efficacious methodologies for combating environmental contamination, in conjunction with the progression of technologies in the domains of chemistry, physics, and biology, has been a subject of extensive discourse [3–5]. The objective of this discussion is to formulate viable alternatives that will enhance the quality of life and manage chemical pollutants, encompassing both organic and inorganic substances [6]. These pollutants have been released into the environment over time without adequate treatment, a practice perpetrated by both households and industries [7–9].

Concomitant with the rising demand for uncontaminated environments, there is a growing interest in renewable energy sources, with solar energy gaining notable prominence on a global scale [10]. The common point of interest between these two materials demands lies in the necessity for materials to exhibit strong absorption in the visible light region [11–13]. In this context, semiconductor photocatalysts, a material that absorbs light energy (usually from the sun or artificial sources) and uses that energy to drive chemical reactions, have garnered considerable

attention due to their wide range of applications, both in pollutant treatment and energy production [14–16].

Among these, titanium dioxide (TiO_2), molybdenum trioxide (MoO_3), and tungsten trioxide (WO_3) are particularly noteworthy due to their high photocatalytic activity, which is crucial for pollutant treatment, and solar energy conversion [17–20]. However, the practical applications of these materials are constrained by their requirement for ultraviolet excitation [11–13]. Consequently, researchers are actively investigating approaches to modify the properties of these materials, such as doping processes and structural alterations, to enhance their ability to efficiently absorb sunlight and generate charge carriers (electrons and holes) capable of driving chemical reactions [21,22].

1.1 Mo and MoO_3

Molybdenum (Mo) is a metal with an atomic number of 42, which places it within the block of external transition metals. Its crystal structure is classified as body-centered cubic (BCC), with a coordination number that ranges from 4 (tetrahedral) to 8 (octahedral). Its electronic configuration, $[\text{Kr}] 5s^1 4d^5$, indicates a half-filled "d" orbital in the ground state, enabling it to form compounds across a wide range of oxidation states (-2, -1, 0, +1, +2, +3, +4, +5, and +6). Among these oxidation states, the most stable are Mo^{4+} and Mo^{6+} [23–25]. Molybdenum exhibits a wide spectrum of stoichiometric forms, thereby facilitating its utilization in diverse domains, including metallic alloys, coating materials, sensors, lubricant formulations, catalysts, and others [24,26].

Molybdenum trioxide (MoO_3) is a compound with molybdenum in its highest oxidation state. It is produced on a larger scale compared to other molybdenum compounds and is considered one of the most important n-type semiconductor oxides [27]. Its oxidation state of +6 enables precise regulation of its crystal structure, morphology, oxygen vacancies, and dopant concentration, making it a versatile material for various applications in electronics and energy storage. When dissolved in a strongly alkaline medium ($\text{pH} > 8$), MoO_3 forms the tetrahedral molybdate anion (MoO_4^{2-}), with the pH level playing a crucial role in the formation of hydrated MoO_3 phases and other oxide variations [28].

MoO_3 exhibits a broad spectrum of oxidation states. Beyond the stoichiometric MoO_3 (Mo^{6+}), molybdenum can also form a class of substoichiometric oxide compounds (mixed) in the form of MoO_{3-x} (Mo^{5+}) and (Mo^{4+}). Before reaching its most reduced form, molybdenum dioxide

(MoO₂) [29,30]. In recent years, researchers have shown great interest in molybdenum trioxide (MoO₃) due to its wide range of technological applications. These applications include gas and humidity sensors [31,32], photocatalytic properties [33], photoluminescence [34], smart windows [35], antibacterial activity [36], solar cells [37], and etc. This wide range of applications can be attributed to the diverse phases and crystallinities that MoO₃ can adopt.

1.2 Structure and Oxygen Vacancies

Crystalline MoO₃ can be synthesized in three main crystal phases: orthorhombic (α -MoO₃) (Figure 1a), monoclinic (β -MoO₃) (Figure 1b), and hexagonal (h-MoO₃) (Figure 1c). The orthorhombic phase is thermodynamically stable, whereas the other two are metastable [38,39]. Each phase of MoO₃ is composed of MoO₆ octahedra (where six oxygen atoms coordinate each molybdenum atom), and the positioning and bonding of these octahedra determine the crystal structure and phase stability (Figure 1).

The monoclinic phase (β -MoO₃) is composed of MoO₆ octahedral units that share corner oxygen atoms along the c-axis, while edge-sharing occurs along the a-axis. The hexagonal phase (h-MoO₃) is formed by zigzag chains of MoO₆ octahedra, which are interconnected by corner-sharing along the c-axis. This structural characteristic of h-MoO₃ results in the presence of tunnels (approximately 3.0 Å in diameter), which likely contain cations or water molecules [40]. This feature may enhance properties of the material [41].

Finally, the orthorhombic phase of α -MoO₃ is formed by MoO₆ octahedra linked through corner and edge-sharing, creating unique double layers of distorted octahedral units (MoO₆) held together by Van der Waals forces [42]. As a result of this sharing, in each octahedron, one oxygen atom is not shared, resulting in a mixture of Mo⁶⁺, Mo⁵⁺, and Mo⁴⁺ ions, thereby creating oxygen vacancies (OVs) between the layers [43,44], where atoms or organic chains can be intercalated to modify physical and/or chemical properties of the material [42,45–51].

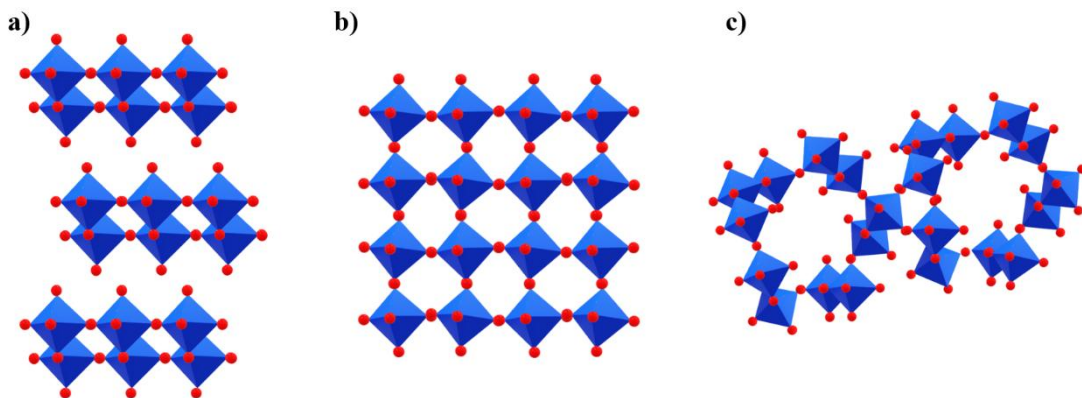


Figure 1: Molybdenum trioxide structures: (a) α -MoO₃, (b) β -MoO₃, (c) h-MoO₃.

The β - MoO_3 and h - MoO_3 phases are unstable, leading to studies on their phase transitions at high temperatures. Research has shown that β - MoO_3 transitions to α - MoO_3 at temperatures between 1123 and 1373 K [52], while h - MoO_3 undergoes this transition at approximately 675 K [53–55]. Specifically, for α - MoO_3 , Silveira *et al.* [56] reported that it remains structurally stable between 20 and 650 °C, regardless of its morphology. However, within this range, a shift in Raman band wavenumbers was observed with increasing temperature, particularly between 25 and 150 °C. Beyond 150 °C, the Raman shifts stabilized and remained relatively constant up to 400 °C.

As mentioned earlier, the formation of Mo^{4+} and Mo^{5+} on MoO_3 , can be associated with the formation of oxygen vacancies. Rellán-Piñeiro *et al.* [44], utilized advanced computational methods like density functional theory (DFT) calculations and X-ray photoelectron spectroscopy (XPS) to investigate the characteristics of vacancies in α - MoO_3 . The results of these analyses demonstrated that vacancies in α - MoO_3 can lead to the formation of two distinct configurations:

1. Two centers of Mo^{5+} : including Mo^{5+} ions coordinated to oxygen ($\text{Mo}^{5+}=\text{O}$) or vacancies ($\text{Mo}^{5+}\oplus$).

2. A single doubly reduced Mo^{4+} . Therefore, it is important to explore ways to control the oxygen vacancies in the material under study to improve magnetic response. In other words, the formation of oxygen vacancies occurs simultaneously with the transformation of Mo^{6+} ions into Mo^{5+} and Mo^{4+} ions [57]. The Figure 2 illustrates the formation of oxygen vacancies within the structure, attributable to the two configurations.

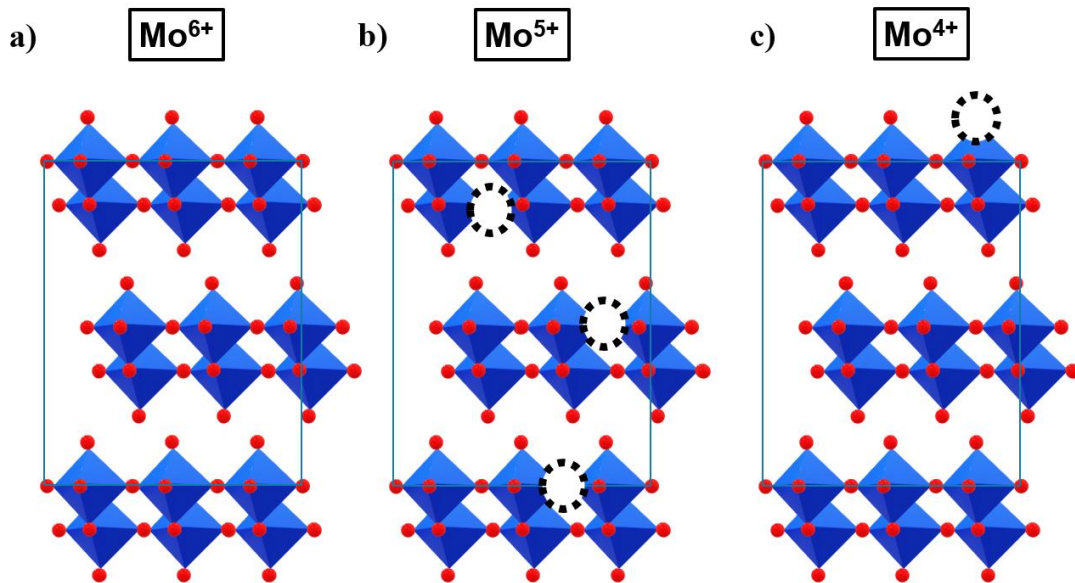


Figure 2: Atomic structures (side view) are illustrated as follows: (a) the pristine MoO_3 (001) surface, (b) the surface with an oxygen vacancy at the bridge site, and (c) a detailed view of the vacancy. The oxygen vacancy is indicated by the dashed blue circle.

Oxygen vacancies act as highly reactive sites, altering the structure, as well as the electronic and chemical properties of materials [58]. The following aspects highlight their role as key factors in catalytic applications:

1. Introducing additional energy levels within the material [58].
2. Enhancing the material's electrical conductivity [58].
3. Modulating chemical reaction rates by facilitating charge transfer involving electrons or holes [58].
4. These levels act as specific reaction sites for certain molecules in catalysis, where they function as electron scavengers, converting attached oxygen gas into superoxide radicals [58].

Several works, encompassing both experimental and theoretical approaches, have been made to modify the structures of molybdenum trioxide (MoO_3) with the aim of enhancing a spectrum of properties, including optical, electrical, and magnetic [59–61]. The importance of oxygen vacancies in the structure of MoO_3 is explored in Section 1.3, where the material's properties are discussed.

1.3 MoO_3 properties

The band gap of $\alpha\text{-MoO}_3$ is approximately 2.8 to 3.0 eV, which results in a low carrier concentration and conductivity. Consequently, its application in devices is unfeasible. However, studies have demonstrated that the formation of oxygen vacancies within the structure can effectively enhance the carrier concentration, thereby improving the material's electrical properties [62–64]. Moreover, oxygen vacancies have been observed to augment the interlayer spacing, thereby enhancing the electrochemical performance of the material. Furthermore, oxygen vacancies have been shown to reduce the energy required for reactions, thereby enhancing the material's gas detection capabilities [57].

In a recent study, Zhang *et al.* [65] utilized a synthetic approach to generate oxygen vacancies in $\alpha\text{-MoO}_3$ nanobelts, with the objective of enhancing the material's electrochemical properties. This strategy resulted in a substantial enhancement in the material's electrical conductivity and an augmentation in its active sites [65]. Building on this finding, Liu *et al.* [66] investigated the effects of the increased active sites induced by oxygen vacancies in photocatalytic applications. They synthesized $\alpha\text{-MoO}_3$ with oxygen vacancies through a solvothermal treatment

using hydrogen peroxide regulation. The oxygen vacancies demonstrated a marked improvement in the photocatalytic degradation of dye and tetracycline. Additionally, they found that the vacancies contribute to light absorption in the visible region and play a crucial role in suppressing the recombination of photoexcited carriers [66]. However, oxygen vacancies have also been demonstrated to modify the magnetic properties of MoO₃ (such as the intensity of magnetization and the hysteresis curve), in addition to altering its electrical properties (such as conductivity and resistivity), as evidenced by studies in the field.

Ijeh *et al.* [67] meticulously investigated the magnetic characteristics of pure α -MoO₃ and copper-doped α -MoO₃ at room temperature, employing a Vibrating Sample Magnetometer (VSM). Their investigations revealed that pure MoO₃ samples exhibited antiferromagnetic behavior, in contrast to copper-doped samples, which displayed ferromagnetic behavior [67]. Furthermore, a potential increase in magnetization was observed as the dopant concentration increased [68–70]. The enhancement of magnetization has been observed in various studies through the incorporation of different materials via doping [68–70].

Nevertheless, the literature reports an unusual magnetic behavior of α -MoO₃ (Figure 3). Kamoun *et al.* [70] investigated the magnetic properties of α -MoO₃ doped with cobalt and nickel. Employing the Vibrating Sample Magnetometer (VSM) technique, they discovered that at room temperature, for low dopant concentrations, the material exhibited ferromagnetic behavior. However, at high dopant concentrations, as the applied magnetic field was increased to a certain critical value (measured in Oersteds, Oe), the magnetization turned negative, and the material exhibited diamagnetic behavior. While this behavior has been observed in various studies with

different materials, such as MoO₃, TiO₂, MoS₂, and carbon nanotubes [70–74], understanding the occurrence of these behaviors remains a challenge.

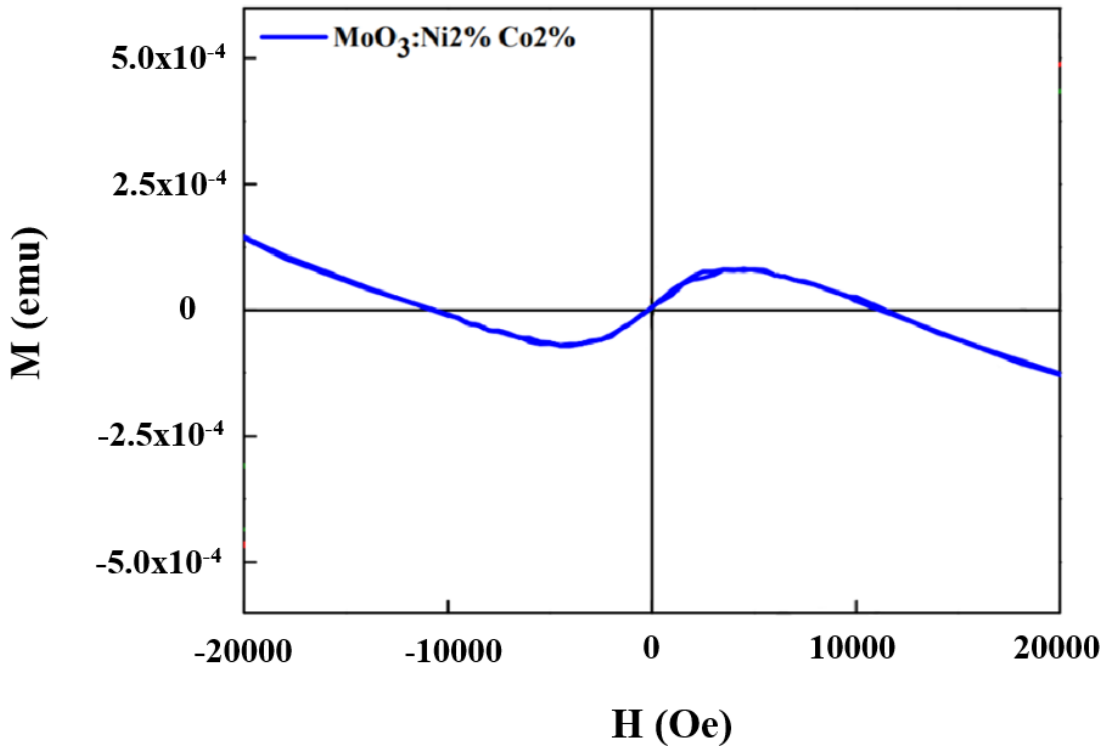


Figure 3: Unusual transition from paramagnetic to diamagnetic behavior. Figure adapted from: [70].

In the literature, various studies associate the magnetic behavior of molybdenum with its ions (Mo⁴⁺, Mo⁵⁺, and Mo⁶⁺). Specifically, it is reported that since MoO₃ is formed, as mentioned before, by Mo⁶⁺ ions, a paramagnetic behavior is expected [68,70,75]. However, many studies observe ferromagnetic or diamagnetic behavior for this compound [68,70,75], which may be associated with the formation of Mo⁵⁺ ions. Therefore, this study will investigate how the doping process and structural defects (oxygen vacancies) influence the magnetic properties of MoO₃.

1.4 Synthesis

The structure, crystalline phase, size, shape, morphology, and structural defects are among the characteristics of the material that determine its properties and applications. Modifications of these parameters can be made during the synthesis route. Consequently, a wide variety of methods have been employed in the production of MoO₃ to modify or enhance the material for specific applications. Among the synthesis routes used for the production of MoO₃, the most common are

sol-gel, hydrothermal methods, thermal evaporation, calcination, solvothermal, co-precipitation, among others (Figure 4).

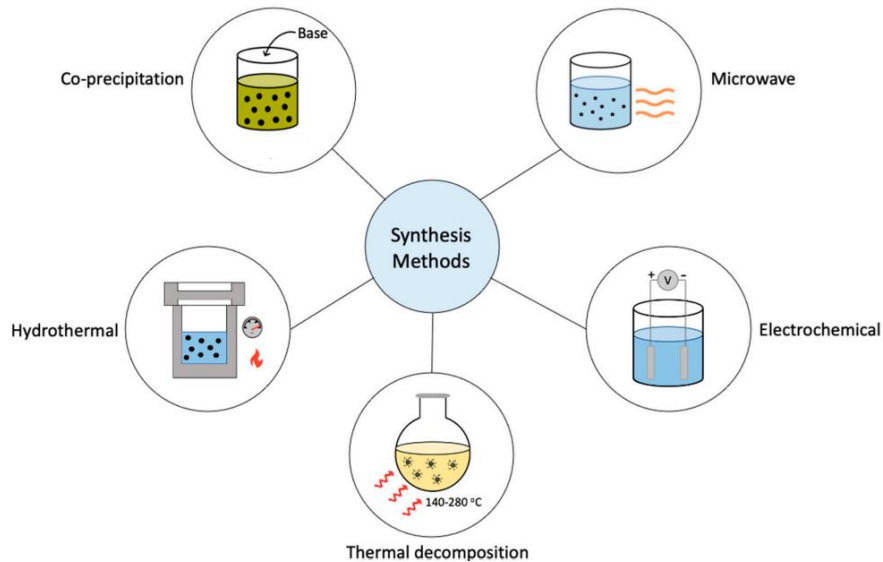


Figure 4: Synthesis methods commonly employed for the preparation MoO₃. Figure adapted from: [133].

Among the processes mentioned, the hydrothermal method is distinguished as the most prevalent for the production of MoO₃ [76]. This method enables precise control over the crystal structure, encompassing both stable and metastable forms [76]. Furthermore, by adjusting experimental parameters such as temperature, pressure, and reaction time, it is possible to modify material characteristics, including size, morphology, and shape [76]. Additionally, the hydrothermal method is a cost-effective and sustainable synthesis technique that ensures high-quality chemical homogeneity. However, certain applications require the presence of active sites within the material structure. Typically, this is achieved through thermal treatment of MoO₃, a process that increases the overall production cost [76].

Although these synthesis routes are highly effective in producing MoO₃, the primary objective of this work is to generate oxygen vacancies within the material. With this aim, a synthesis route capable of producing MoO₃ with a high concentration of oxygen vacancies was pursued.

Studies on techniques for obtaining materials with control over the creation of oxygen vacancies are still ongoing. Chithambararaj *et al.* [77] investigated the thermal decomposition of ammonium heptamolybdate (HMA) in the temperature range of 50 to 675 °C and observed that the α -MoO₃ phase is formed from 325 °C onwards. When analyzing the XRD results and

comparing them with crystallographic data from the literature, they observed a decrease in the material's stoichiometry, indicating an increase in oxygen vacancies with increasing temperature. These results demonstrate the significant role of temperature in controlling the concentration of vacancies [77]; consequently, control over the formation of Mo^{4+} and Mo^{5+} ions is achieved.

Furthermore, it is known that the environment also influences the creation of oxygen vacancies [78]. Consequently, a method that can be employed to control these vacancies involves the thermal treatment of the material at high temperatures while controlling the environment [79,80]. Silva *et al.* [78] conducted Raman spectroscopy and XRD experiments, manipulating temperature and atmosphere conditions. They varied the temperature in the range of 100 - 400 °C under three different environments: 100 % He, 20 % O_2/He , and 5 % H_2/He . Consequently, due to the high exposure to oxygen in an O_2 atmosphere, they observed a filling of vacancies within the structure. On the other hand, exposure to H_2 resulted in the formation of water and vacancies [78].

It has been well established that removing oxygen atoms from lattice sites to form a gas phase is an effective method for generating oxygen vacancies [57]. Thermal treatment in a reducing environment can facilitate the incorporation of oxygen vacancies and allowing precise control over their concentration on the surface of metal oxides by adjusting the annealing temperature [57]. Thus, for this study, thermal treatment was selected as the synthesis route due to its simplicity, low cost, and efficiency in creating oxygen vacancies.

1.5 Thesis outline

In this study, MoO_3 crystals were synthesized via the thermal decomposition of ammonium heptamolybdate and subsequently characterized in terms of their structural and magnetic properties. The thesis is organized into three primary chapters, with Chapters 2, 3, and 4 comprising published and submitted articles. Finally, Chapter 5 presents a comprehensive conclusion for the doctoral research.

The structure of the thesis is as follows:

Chapter 2 presents a method to enhance the magnetic properties of MoO_3 through the synthesis, characterization, and magnetic analysis of pure $\alpha\text{-MoO}_3$ and $\alpha\text{-MoO}_3$ doped with varying concentrations of iron. Furthermore, the chapter identifies an unusual magnetic phenomenon observed in certain metal oxides, including MoO_3 , and proposes an explanation for

this behavior. This proposal subsequently serves as the foundational basis for the subsequent research outlined in Chapter 3. The work under consideration was published in Solid State Sciences and is entitled "Synthesis and magnetic characterization of iron-doped molybdenum trioxide (α -MoO₃:xFe)"[81].

Chapter 3 describes the first attempt to elucidate this phenomenon, which was accomplished by modifying the oxygen vacancies in the material. Efforts to control these vacancies were made by adjusting the temperature and the environmental conditions during the synthesis process. To achieve precise control over these environmental conditions, the materials were synthesized in a furnace, where control over temperature, pressure, and atmosphere could be maintained. The present study focuses on the synthesis of MoO₃ with varying levels of vacancies, as these samples would serve as the foundation for the subsequent study. The research in focus has been published in the journal Solid State Sciences, under the title "Influence of temperature and gas atmosphere on the thermal decomposition of (NH₄)₆Mo₇O₂₄•4H₂O" [82].

Chapter 4 provides a study of the influence of oxygen vacancies and, consequently, the formation of Mo⁴⁺ and Mo⁵⁺ ions on the magnetic properties of MoO₃. The synthesis conditions for the samples were selected based on the work presented in Chapter 3. This portion of the research is under submission in Solid State Sciences, with the title "Magnetic Transition in MoO₃: Influence of Mo⁵⁺/Mo⁶⁺ Ratios on Paramagnetic to Diamagnetic Behavior". Lastly, chapter 5 presents a general conclusion for the study.

In the appendix an exposition of the methodology and physics employed in the main characterization techniques used in this work, can be found.

1.1 Objectives

The objective of this study is to synthesize and control the structural properties of pure molybdenum trioxide (MoO_3). Subsequently, the research will concentrate on examining the structure, morphology, and composition of the material through the utilization of an array of characterization techniques, including Raman spectroscopy, Fourier Transform Infrared Spectroscopy (FTIR), XRD, Scanning electron microscopy (SEM), Energy Dispersive Spectroscopy (EDS), and XPS. With precise control over the material's structure, the research aims to enhance the magnetic properties through structural defects or doping processes, targeting potential future applications. Furthermore, the investigation will encompass an examination of the magnetic properties of MoO_3 .

- Synthesize MoO_3 through solid-state reaction methods;
- Investigate the structure, morphology, and composition of the synthesized material;
- Modify synthesis parameters to introduce structural defects;
- Dope the material with iron;
- Examine the magnetic properties resulting from structural defects and doping;
- Explore the mechanism underlying the magnetic response of MoO_3 .

2. Synthesis and magnetic characterization of iron-doped molybdenum trioxide (α -MoO₃:xFe) [81]

The combination of specific properties, including room-temperature ferromagnetism and semiconducting behavior, is widely regarded as essential for applications in spintronic and magneto-optic devices [74]. Therefore, developing strategies to effectively enhance ferromagnetism in metallic materials has become a focal point of research interest [74]. Controlled doping of atoms or ions within materials has emerged as a promising approach for fine-tuning material properties [49,68,83,84]. In this context, transition metal oxide compounds, such as TiO₂, WO₃, MoO₃, and CeO₂, have gained prominence due to their advantageous electronic structures and robust physical properties [85–89]. Among these, molybdenum trioxide (MoO₃) has drawn particular attention due to its extensive range of technological applications. Building on this, the objective of this chapter is to synthesize MoO₃ doped with Fe, aiming to enhance its magnetic properties while maintaining favorable electrical characteristics.

2.1 Synthesis

The preparation of iron-doped molybdenum trioxide (Fe:MoO₃) was carried out through a solid-state reaction, which involved the use of ammonium heptamolybdate tetrahydrate [(NH₄)₆Mo₇O₂₄•4H₂O] (Vetec – 99 %) and nonahydrate iron nitrate [Fe(NO₃)₃•9H₂O] (NEON – 98 %) as precursors. In the synthesis process, four ceramic crucibles with lids were employed, into each of which 1 g of (NH₄)₆Mo₇O₂₄•4H₂O was introduced, followed by the addition of Fe(NO₃)₃•9H₂O in weight proportions of 0, 1, 3, and 5 %, respectively. Subsequently, 10 mL of methanol were mixed with each crucible to obtain a homogeneous suspension. The crucibles containing the solutions were then heated to 450 °C for 6 h.

2.2 Results and discussion

2.2.1 X-ray Diffraction (XRD)

XRD analysis was carried out using a third-generation Malvern Panalytical diffractometer equipped with Cu-K, scanning in the 2 theta range from 2° to 70°. Figure 5 displays the XRD powder analysis results for both pure MoO₃ and Fe-doped MoO₃ samples at room temperature.

The X-ray diffraction patterns depicted in Figure 5 (a) reveal the presence of the orthorhombic phase of MoO_3 with the Pbnm space group for both pure and Fe-doped samples. This observation aligns well with the data provided in the ICSD Card No. 35076 [90–92], which serves as a reference for the orthorhombic phase of MoO_3 .

In pure MoO_3 , no additional phases were detected. However, in the MoO_3 :1% Fe, MoO_3 :3% Fe, and MoO_3 :5% Fe samples, extra peaks were observed in the analysis. These peaks correspond to the monoclinic $\text{Fe}_2(\text{MoO}_4)_3$ phase, which belongs to the $\text{P2}_1/\text{a}$ space group, as confirmed by reference (ICSD Card No. 100606) [93,94]. These findings indicate that doping MoO_3 with Fe promotes the formation of $\text{Fe}_2(\text{MoO}_4)_3$ within the material. Consequently, Fe-doped MoO_3 samples exhibit a mixture of two crystalline phases: the orthorhombic MoO_3 and the newly formed monoclinic $\text{Fe}_2(\text{MoO}_4)_3$.

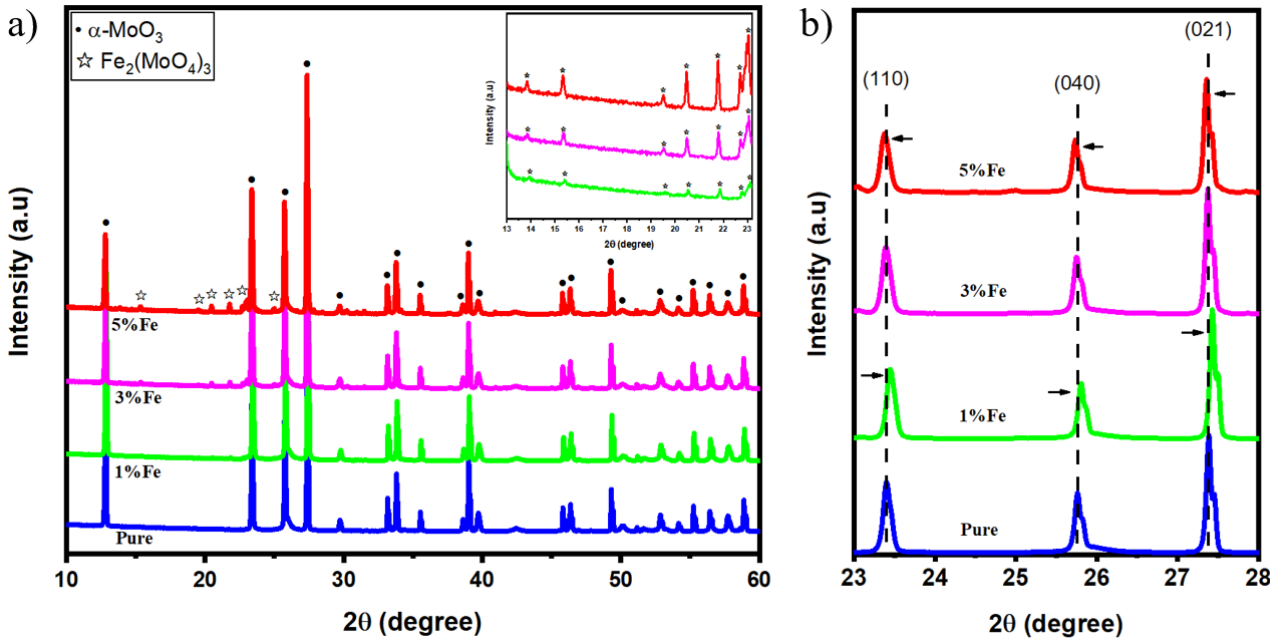


Figure 5: X-ray diffraction patterns of $\alpha\text{-MoO}_3$ a) pure and Fe-doped samples. The inset shows the peaks of $\text{Fe}_2(\text{MoO}_4)_3$. b) Comparison of positions peaks (110), (040), and (021) of the $\alpha\text{-MoO}_3$ phase. Figure taken from: [81]

Figure 5 (b) depicts the displacements of the peaks (110), (040), and (021) within the $\alpha\text{-MoO}_3$ phase. The arrows point in the direction of the shifts in 2θ values relative to the planes of the pristine sample, denoted by a vertical dashed line. A comparative examination of the diffractograms between the MoO_3 :1 % sample and the pure MoO_3 sample reveals that these planes exhibit shifts toward higher 2θ values. This shift can be ascribed to a compression of the lattice parameters along the a, b, and c axes. Conversely, when contrasting the MoO_3 :3% and MoO_3 :5%

samples with the pure MoO₃ sample, the observed values shift towards lower 2θ values, signifying an expansion of the lattice parameters.

A comparable phenomenon was documented by Wan and Leonard [95] in their investigation of the β-Mo₂C structure with increasing Fe dopant. They noted that as the concentration of Fe dopant in the precursors increased, the (010) peak shifted towards higher 2θ angles, reaching a maximum when the Fe:Mo ratio was 0.08:1. Beyond this ratio, an additional phase of molybdenum carbide (γ-MoC) emerged, and the (010) peak shifted towards smaller 2θ angles [95]. This trend was also evident in the (002) and (011) peaks. To determine the precise lattice parameters and unit cell, they utilized the PDXL software in their XRD peak analysis. Their findings indicated that smaller iron atoms may randomly substitute molybdenum atoms within the crystal structure. In the context of our research, the observed shift towards higher 2θ angles in the MoO₃:1 % Fe sample can be attributed to the substitution of smaller Fe ions (Fe³⁺ with an atomic radius of approximately 64.5 pm [96]) for Mo ions (Mo⁶⁺ with an atomic radius of approximately 65.0 pm [96]) in the crystal structure, driven by their similar atomic radii.

2.2.2 Scanning electron microscopy (SEM)

SEM images were captured with a FEI Quanta 450 FEG microscope, and EDS data for elemental mapping was collected using an X-ray detector model 150 from Oxford, which was connected to the Quanta 450 FEG microscope. The SEM images illustrate the influence of dopants on the morphology of both pure and Fe-doped MoO₃ samples. In Figure 6 (a–f), high-magnification SEM images are presented, showing (a) the pure MoO₃ sample, (b) MoO₃:1%Fe, (c) MoO₃:3%Fe, and (d) MoO₃:5%Fe samples. These images reveal that all the samples predominantly exhibit a plate-like morphology, consistent with prior research [97–99]. However, the doped samples display a combination of MoO₃ plates interspersed with occasional cuboid morphologies of Fe₂(MoO₄)₃, as depicted in Figure 6 (e, f) [100]. The presence of cuboid structures can be attributed to the incorporation of Fe dopants into the MoO₃ lattice, leading to the formation of the secondary phase Fe₂(MoO₄)₃.

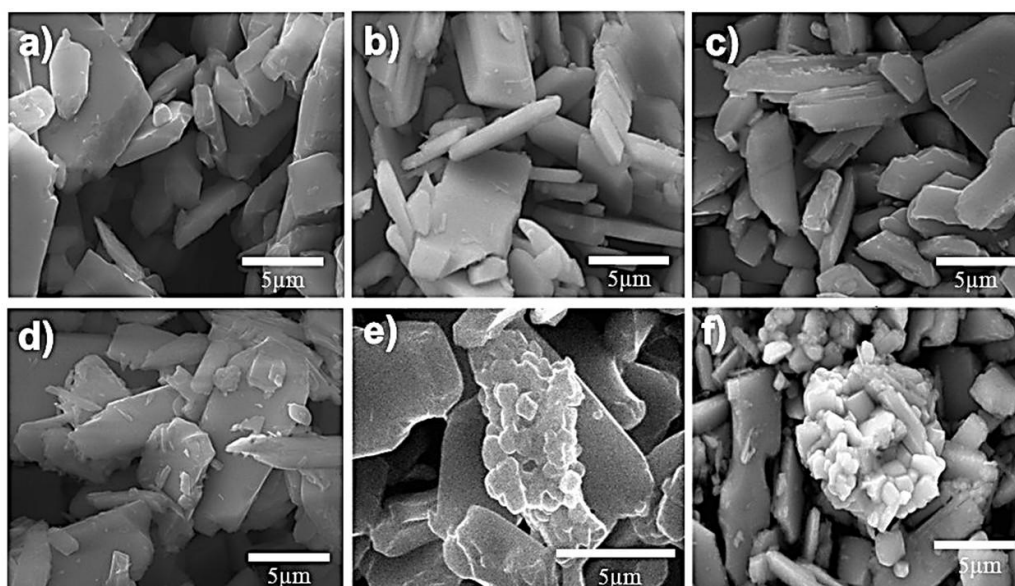


Figure 6: High-magnification SEM images depicting the plate-like morphology of (a) pure MoO_3 , (b) MoO_3 :1%Fe, (c) MoO_3 :3%Fe, and (d) MoO_3 :5%Fe samples are presented. Additionally, SEM images illustrating the cuboid morphology of $\text{Fe}_2(\text{MoO}_4)_3$ in (e) MoO_3 :1%Fe and (f) MoO_3 :5%Fe samples are also shown. Figure taken from: [81].

In Figure 7 (a-d), the EDS results are presented to depict the spatial distribution of Mo, O, and Fe elements within the samples. It is observable that in the MoO_3 :1%Fe sample, the Fe distribution appears predominantly uniform throughout the sample, with sporadic small island-like regions displaying elevated Fe density, as highlighted by red dashed circles. Elemental mapping suggests that Fe is evenly distributed throughout the MoO_3 samples, with a minimal concentration of a Fe-rich secondary phase, possibly $\text{Fe}_2(\text{MoO}_4)_3$, as detected by XRD. However, in the case of the MoO_3 :3%Fe and MoO_3 :5%Fe samples, the presence of these island-like regions rich in Fe becomes more pronounced, signifying an increased formation of the secondary phase [$\text{Fe}_2(\text{MoO}_4)_3$], consistent with the XRD results.

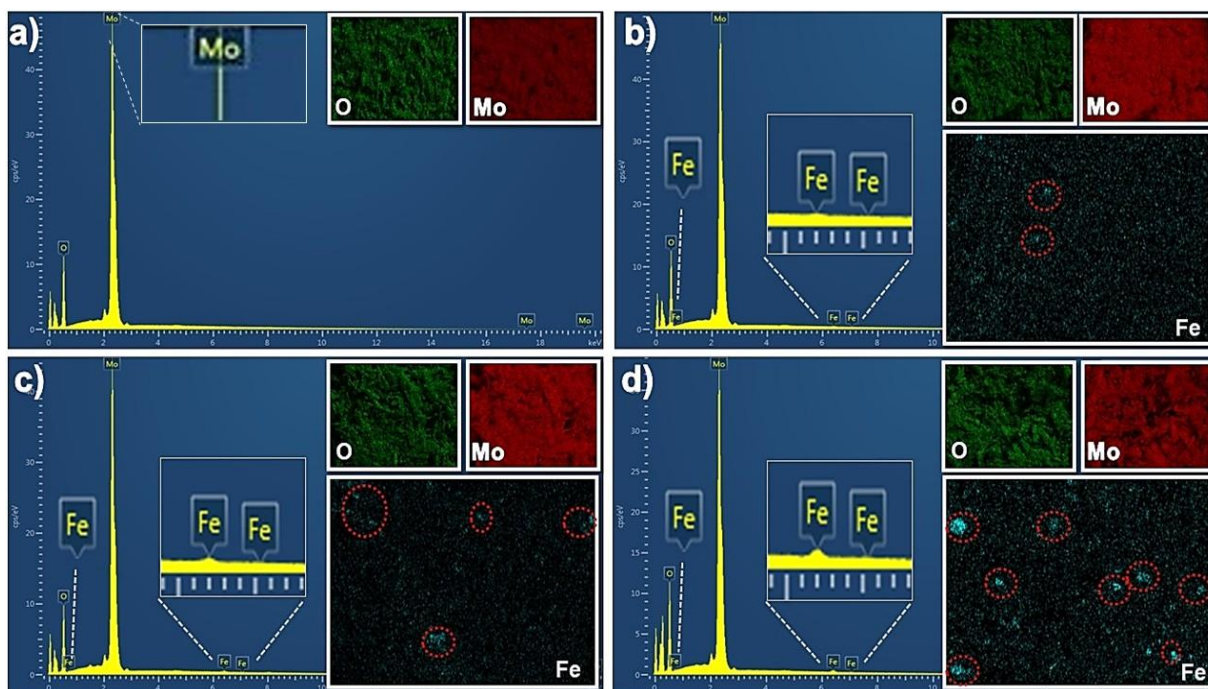


Figure 7: EDS spectra accompanied by images illustrating the elemental distribution of Mo, O, and Fe in (a) pure MoO_3 , (b) MoO_3 :1%Fe, (c) MoO_3 :3%Fe, and (d) MoO_3 :5%Fe samples are provided. To enhance visualization, the Fe-rich secondary phase, identified as $\text{Fe}_2(\text{MoO}_4)_3$, has been highlighted using red dashed circles. Figure taken from: [81]

To gain a deeper understanding of the Fe distribution in the two phases, localized EDS measurements were conducted on two representative samples, MoO_3 :1%Fe and MoO_3 :5%Fe, as shown in Figure 8. These samples were selected to represent lower and higher Fe concentrations, respectively. In Figure 8, specific measurement points labeled as I, II, III, IV, and V were identified, and the corresponding measured values are detailed in Table 1. EDS was utilized as the analytical technique, offering a qualitative assessment of the elemental composition within the samples. It's worth noting, however, that EDS has limitations when it comes to quantitative analysis accuracy.

Upon analyzing the values presented in the Table 1, it becomes evident that two distinct phases are present: the first phase corresponds to MoO_3 , and the second phase corresponds to $\text{Fe}_2(\text{MoO}_4)_3$. Within the MoO_3 phase, a minor amount of Fe is detectable, suggesting the incorporation of iron into the structure through doping. Furthermore, there is a noticeable increase in the concentration of Fe within the MoO_3 crystals in the case of the MoO_3 :5%Fe sample compared to the MoO_3 :1%Fe sample, indicating that Fe concentration increases with higher dopant levels. The introduction of Fe into the MoO_3 phase does not result in significant alterations in the lattice parameters, owing to the extremely low concentration of Fe. Therefore, there are no

significant changes in lattice parameters or crystal structure. As for the second phase, $\text{Fe}_2(\text{MoO}_4)_3$, similar values for the element percentages are observed in both the MoO_3 :1%Fe and MoO_3 :5%Fe samples. This suggests that only a small portion of the iron introduced during the synthesis serves as a dopant in the material, while a substantial portion contributes to the formation of a larger quantity of the second phase, $\text{Fe}_2(\text{MoO}_4)_3$.

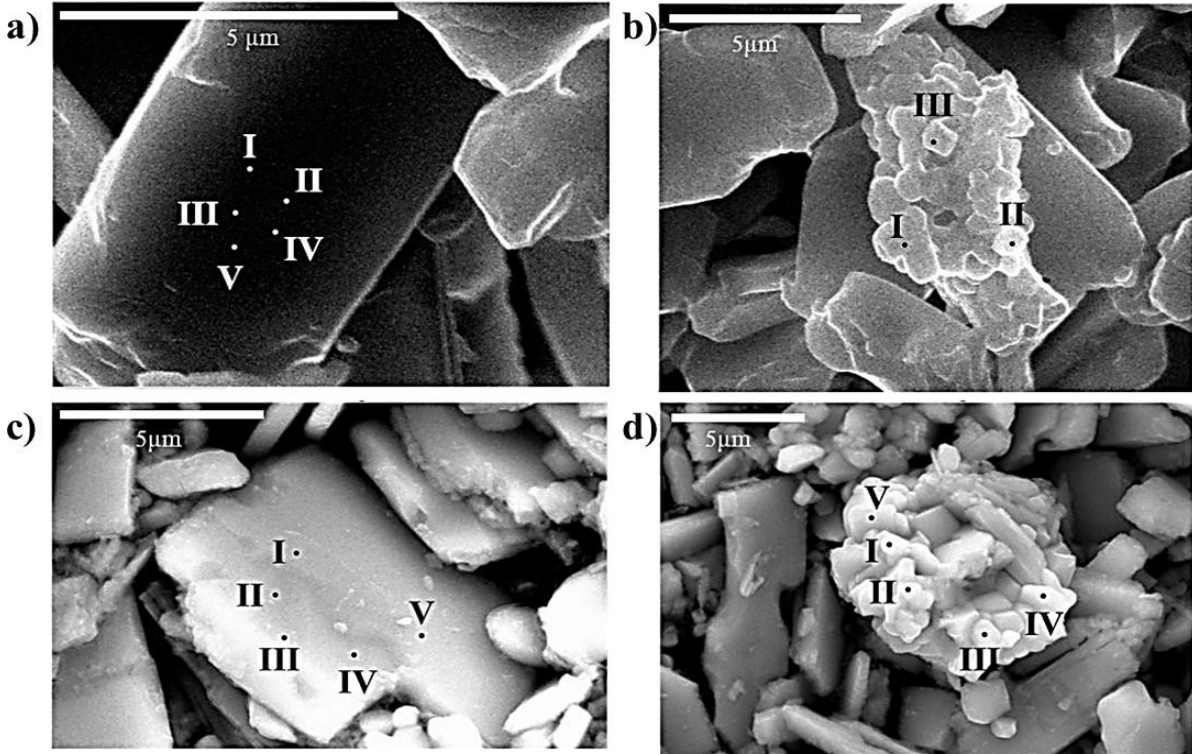


Figure 8: Punctual EDS of a) MoO_3 -plate in MoO_3 :1%Fe sample, b) $\text{Fe}_2(\text{MoO}_4)_3$ in MoO_3 :1%Fe sample, c) MoO_3 -plate in MoO_3 :5%Fe sample and d) $\text{Fe}_2(\text{MoO}_4)_3$ in MoO_3 :5%Fe sample. Figure taken from: [81].

Table 1: The percentage of weight contributed by each element: Mo, O, and Fe, was determined through point measurements using EDS. Table taken from: [81].

	MoO_3 - (MoO_3 :1%Fe)			$\text{Fe}_2(\text{MoO}_4)_3$ (MoO_3 :1%Fe)			MoO_3 -plate (MoO_3 :5%Fe)			$\text{Fe}_2(\text{MoO}_4)_3$ (MoO_3 :5%Fe)		
	Mo (%)	O (%)	Fe (%)	Mo (%)	O (%)	Fe (%)	Mo (%)	O (%)	Fe (%)	Mo (%)	O (%)	Fe (%)
I	83.0	17.0	0	51.4	33.9	14.7	56.1	43.4	0.5	43.2	45.8	11.0
II	79.5	20.4	0.1	48.8	36.0	15.2	55.4	44.1	0.5	41.7	46.8	11.6
III	80.3	19.4	0.3	45.7	41.9	12.4	55.9	43.8	0.3	42.8	43.9	13.3
IV	78.2	21.4	0.3	-	-	-	55.6	44.2	0.6	46.7	40.6	12.7
V	73.9	25.9	0.2	-	-	-	56.2	43.4	0.4	47.3	38.0	14.7

2.2.3 Raman spectroscopy

Raman measurements were conducted using a Bruker Senterra Spectrometer equipped with a CCD system (Olympus BX50). Three accumulations were performed, with a 60-second acquisition time. The laser employed operated at 785 nm and used a 100X focusing lens within a range of 85 - 1200 cm^{-1} . The Raman spectra for both pure and Fe-doped MoO_3 samples are displayed in Figure 9 (a). In accordance with previous research [90], the Raman peaks are attributed to the orthorhombic phase of MoO_3 in all four samples. The specific peak assignments can be found in Table 2.

Table 2: Raman peak positions were observed in each sample, along with their corresponding molecular assignments. Table taken from: [81].

MoO_3 Raman bands (cm^{-1})	Representation	Attribution
154	A_g/B_{1g}	T_b^*
196	B_{2g}	τ O=Mo=O
216	A_g	R_c **
243	B_{3g}	τ O=Mo=O
290	B_{3g}	ω O=Mo=O
338	A_g/B_{1g}	δ O-Mo-O
365	-	-
379	B_{1g}	δ O=Mo=O
471	A_g/B_{1g}	ν, δ O-Mo-O
666	B_{2g}/B_{3g}	ν O-Mo-O
820	A_g/B_{1g}	ν_s O=Mo=O
995	A_g	ν_{as} O=Mo=O

$\nu \rightarrow$ Stretching vibration, $\nu_s \rightarrow$ Symmetric stretching, $\nu_{as} \rightarrow$ Asymmetric stretching

$\tau \rightarrow$ Twisting vibration, $\omega \rightarrow$ Wagging vibration, $\delta \rightarrow$ Bending vibration,

$T_b \rightarrow$ Translational mode along the b-axis, $R_c \rightarrow$ Rotational mode around the c-axis

The $\text{MoO}_3:5\%\text{Fe}$ sample exhibits five new peaks (Figure 9 (a)), which are characteristic of the monoclinic phase of $\text{Fe}_2(\text{MoO}_4)_3$ [101]. These additional peaks are not present in the $\text{MoO}_3:1\%\text{Fe}$ and $\text{MoO}_3:3\%\text{Fe}$ samples. This is because the quantity of the secondary phase

($\text{Fe}_2(\text{MoO}_4)_3$) in these two samples is insufficient to be detected by Raman spectroscopy. However, changes were observed in the intensity ratio of peaks at 285 and 290 cm^{-1} (Figure 9 (c)), as well as in the full width at half maximum (FWHM) of the peaks at 666 (Figure 9 (d)) and 995 cm^{-1} (Figure 9 (e)). The peaks underwent deconvolution (Figure 9 (b)), and the resulting values have been compiled in Table 3.

Dieterle *et al.* [102] conducted a research study centered on the preparation of MoO_{3-x} samples, subjecting them to varying temperature and gas atmosphere conditions. A comprehensive characterization was performed, utilizing techniques such as XRD, SEM, diffuse reflection UV-vis spectroscopy, and Raman spectroscopy. The primary objective was to investigate the properties of these samples in relation to different concentrations of oxygen vacancies. The researchers successfully established a linear relationship between the Raman band intensity ratios at 285 and 295 cm^{-1} and the sample's oxygen-to-metal ratio. This discovery suggests that the Raman band intensity ratio can serve as an effective method for determining the oxygen stoichiometry in MoO_{3-x} .

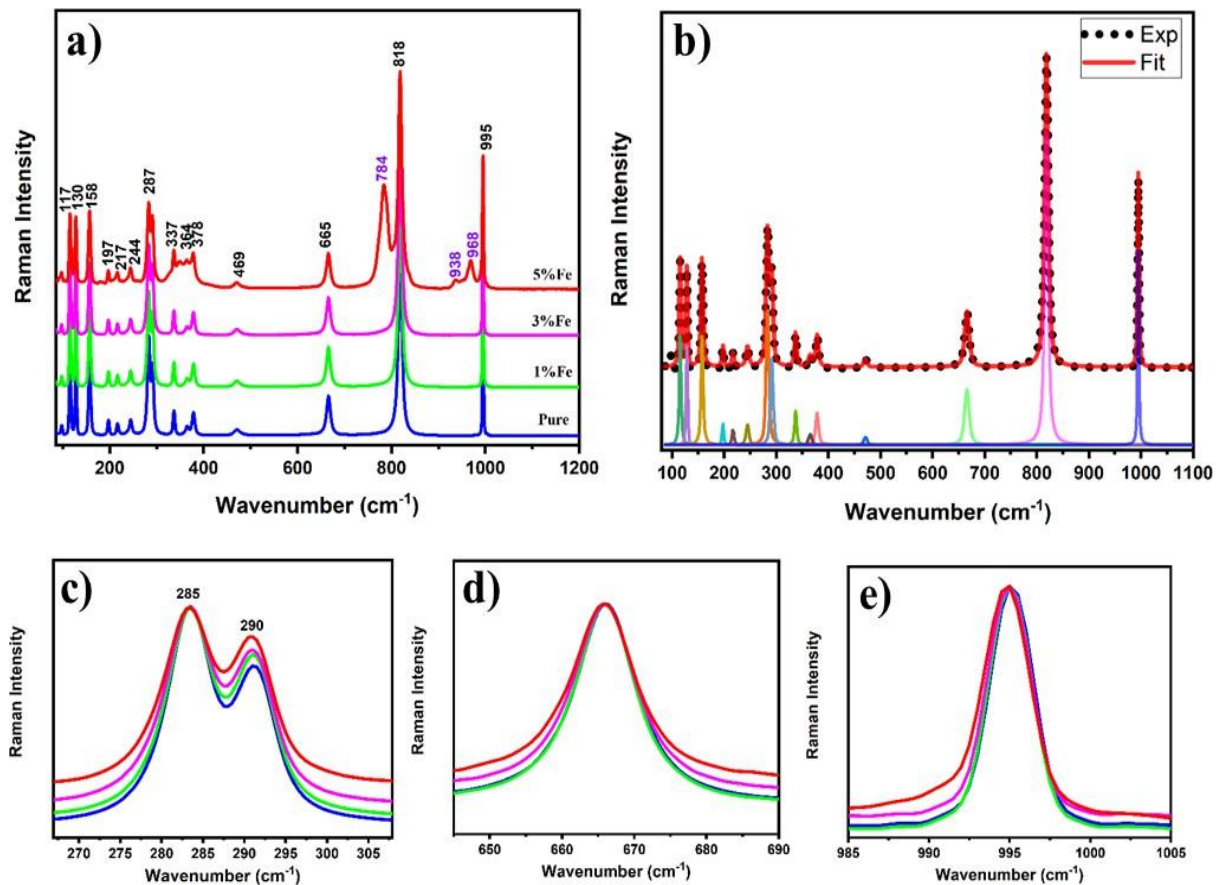


Figure 9: (a) Raman spectra of pure and Fe-doped α - MoO_3 , (b) decomposition analysis of Raman peaks for pure MoO_3 , (c) intensity ratio of the 285/290 cm^{-1} peaks, and variations in peak width at (d) 666 cm^{-1} and (e) 995 cm^{-1} are presented. Figure taken from: [81].

As previously outlined in Dieterle’s work [102], alterations in the intensity ratio of peaks at 285 and 290 cm^{-1} , along with subtle variations in the full width at half maximum (FWHM) of the peaks at 666, 820, and 995 cm^{-1} , signify changes in oxygen vacancies. These changes in Raman peaks at 820 and 995 cm^{-1} are associated with the distances between Mo=O bonds along the a and b-axes, which are shorter than the Mo-O bond distance along the c-axis [102,103]. The Raman bands at 820 and 996 cm^{-1} are attributed to the stretching vibration of terminal Mo=O bonds along the a and b-axes [102,104]. Conversely, the oxygen atoms acting as bridges, with longer bond distances along the c-axis, form the weakest bonds [102,105]. This suggests that the preferential generation of oxygen vacancies in the oxide matrix (MoO_3) occurs along the c-axis, a finding supported by XRD results obtained by [102,103]. Consequently, it’s expected that when bridging oxygen is lost, the Mo atom will shift towards the terminal oxygen in the b- direction, weakening the bond with the terminal oxygen atom along the a-axis [102,103].

Considering the relatively minor variation in stoichiometry across the sample series, only slight changes are anticipated in the Raman bands associated with localized vibrations, such as those at 666, 823, or 995 cm^{-1} [102]. The intensity and width of the prominent bands at 823 and 995 cm^{-1} are likely to increase due to differences in crystallization levels and oxygen/metal ratios [102]. However, it’s important to note that while these changes have been observed, our work does not fully elucidate the exact mechanism by which dopants influence oxygen vacancies. Consequently, further research is needed to draw more definitive conclusions on this matter.

Table 3: Ratio between the intensity of peaks at 285 and 290 cm^{-1} , and FWHM of peaks at 666 and 995 cm^{-1} . Table taken from: [81]:

Doping (%)	Intensity Ratio 285/290	FWHM 666 cm^{-1}	FWHM 995 cm^{-1}
0	1.51	10.02	3.16
1	1.41	10.00	3.18
3	1.43	10.30	3.24
5	1.31	10.49	3.44

2.2.4 Fourier Transform Infrared spectroscopy (FTIR)

FTIR spectra were acquired utilizing a Perkin Elmer Spectra-two spectrophotometer operating in ATR mode, covering a spectral range from 600 to 4000 cm^{-1} . The data were collected at a resolution of 4 cm^{-1} , with each spectrum resulting from the accumulation of 60 scans. The

FTIR spectrum for Fe-doped MoO₃ microcrystals is displayed in Figure 10. This figure presents absorption peaks within the 500-1200 cm⁻¹ range, corresponding to characteristic vibrations of metal-oxygen bonds, including stretching and bending modes. Specifically, the band at 981 cm⁻¹ signifies the presence of the layered orthorhombic phase and corresponds to Mo=O stretching [38,106]. The bands at 810 and 845 cm⁻¹ are associated with the stretching mode of oxygen in Mo–O–Mo bonds [38,43,90,107,108]. The band at 555 cm⁻¹ can be attributed to the vibration of O linked to three metal atoms, denoted as O–3Mo vibration [38,108]. Notably, due to the low concentration of dopants, no bands indicative of iron-related bonds are detected in the FTIR spectrum.

With the increase in the Fe concentration used, it becomes evident that the bands at 810 cm⁻¹, which are associated with the O-Mo-O group, maintain their positions without any noticeable shift. However, there is a notable shift to higher wavenumber values in the spectral band occurring at 981 cm⁻¹, related to the Mo=O bond. This observation indicates that the higher concentration of incorporated iron ions directly influences the Mo=O bond within the structure.

These results are consistent with the findings obtained through Raman spectroscopy. Specifically, in this analysis, changes are observed exclusively in the peaks associated with the Mo=O bond, resulting in modifications in the full width at half maximum (FWHM) of the material.

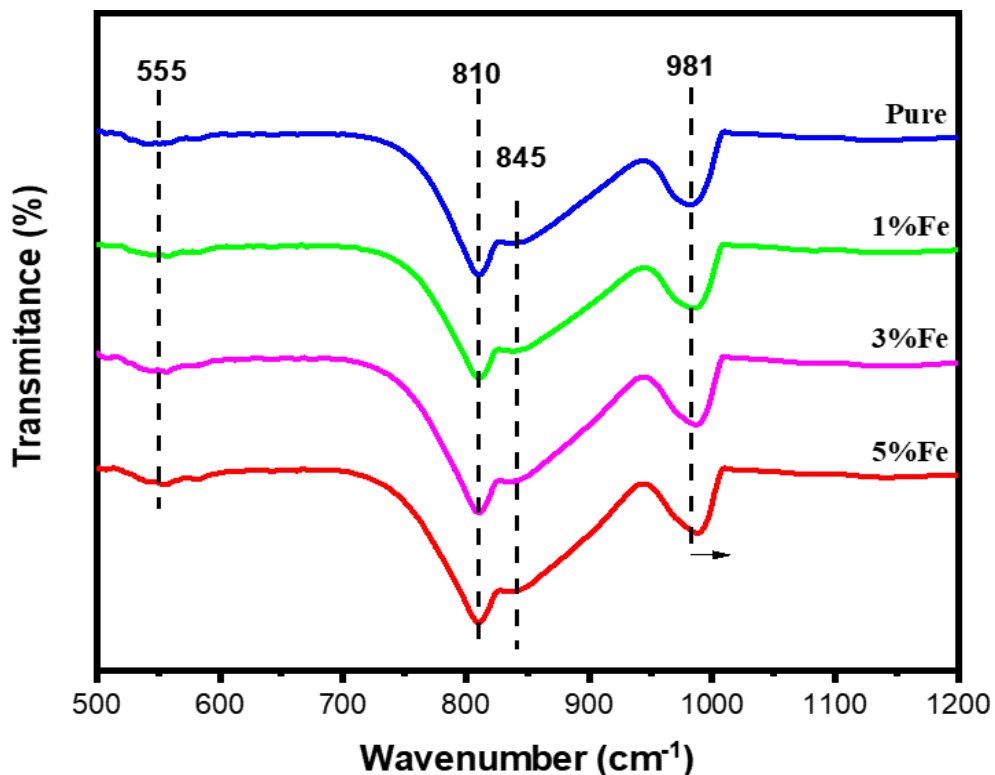


Figure 10: FTIR spectra of pure and Fe-doped α-MoO₃. Figure taken from: [81].

2.2.5 Magnetic Properties at Room Temperature

VSM measurements were analyzed using a Quantum Design PPMS® Dy- naCool (9T) at room temperature, where an external field of up to $\pm 9,000$ Oe was applied. The Fe-doped MoO_3 samples were measured in powder form and positioned in a sample holder. Figure 11 (a) illustrates the magnetic curves for these samples, revealing a noticeable change in magnetization in the presence of an applied magnetic field of 10,000 Oe due to the presence of Fe. In Figure 11 (b), representing pure $\alpha\text{-MoO}_3$, it can be observed that magnetization is negative for magnetic fields exceeding 2,900 Oe, and conversely, it becomes positive for negative fields below -3,050 Oe. A similar magnetic behavior was observed by Raj *et al.* [109], and this phenomenon might be attributed to the diamagnetic properties of Mo^{6+} . Nevertheless, further research is warranted to provide a comprehensive explanation for this observation [110–112].

The magnetization curve depicted in Figure 11 (b) reveals that the magnetization remains positive and relatively stable within the range of magnetic fields spanning from 700 to 1,000 Oe. Moving on to Figure 11 (c), the magnetization curve for $\text{MoO}_3:1\%\text{Fe}$ is presented, showing a positive magnetization for positive magnetic fields, in contrast to the behavior observed in the pure sample. Moreover, it's worth noting that the magnetization does not reach saturation even in the presence of 10,000 Oe.

In Figure 11 (a), it's noticeable that the magnetization curve of $\text{MoO}_3:1\% \text{Fe}$ exhibits higher magnetization compared to that of $\text{MoO}_3:3\% \text{Fe}$, even though it has a higher Fe percentage. $\text{MoO}_3:5\% \text{Fe}$, on the other hand, displays a substantial increase in magnetization compared to the other samples. This suggests that this increased in magnetization can be attributed to the greater presence of iron in this sample, as observed in the SEM measurements. Additionally, in $\text{MoO}_3:3\% \text{Fe}$ samples (Figure 11 (d)), it's noteworthy that the magnetization does not saturate even in the presence of a 10,000 Oe magnetic field. The behavior observed for different Fe concentrations indicates the existence of a competitive mechanism among various iron sites in the sample. Regarding the primary and secondary phases, it is challenging to distinguish these two phases in the magnetic curves of the doped samples. Further investigations are warranted to provide a comprehensive explanation for these findings.

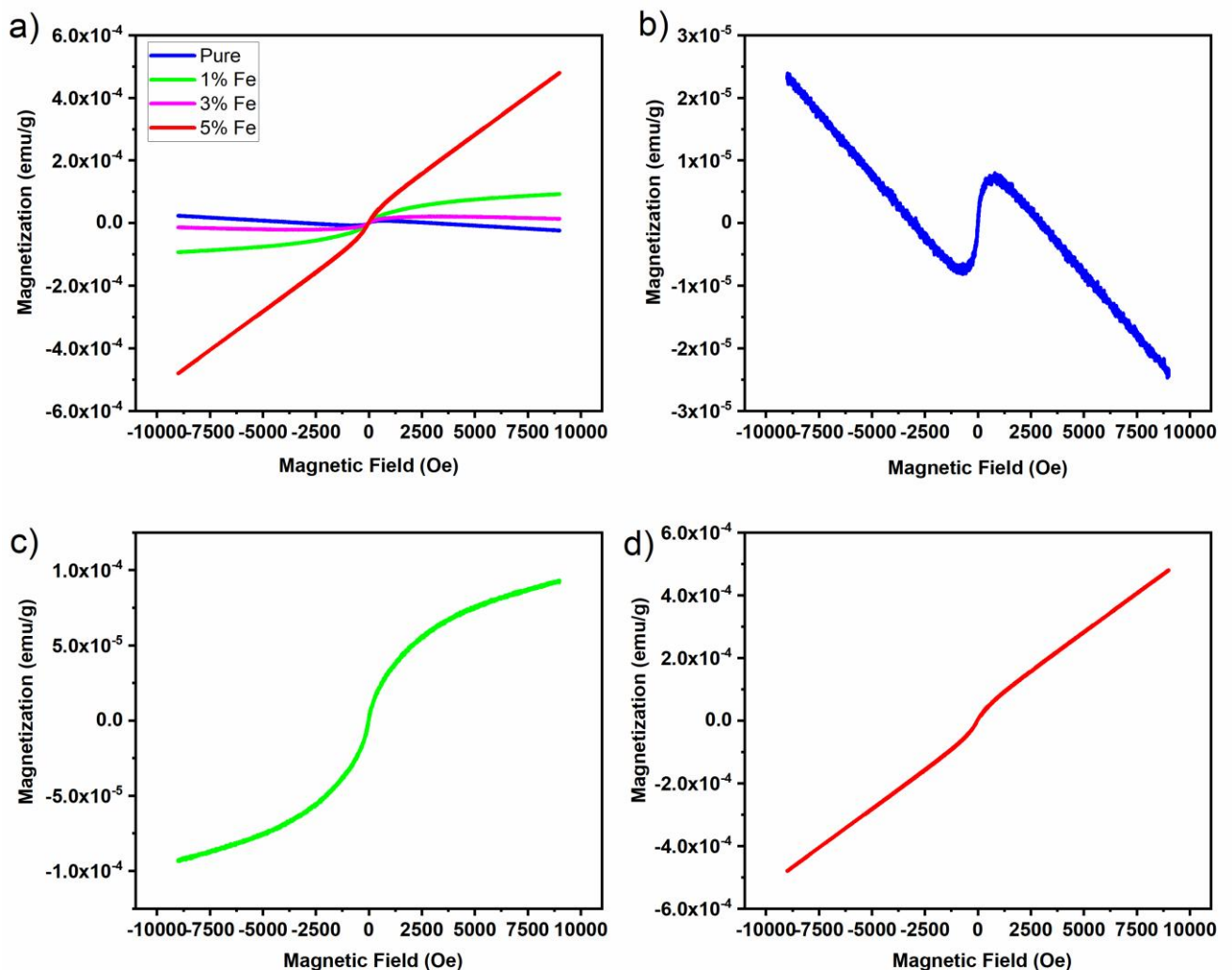


Figure 11: a) Magnetic curves of Fe-doped molybdenum trioxide (MoO_3) samples with varying iron concentrations of 0 (pure), 1, 3, and 5 %. The magnetic curves of b) the pure sample, c) $\text{MoO}_3:1\% \text{Fe}$, and d) $\text{MoO}_3:5\% \text{Fe}$ are shown. Figure taken from: [81].

2.3 Final considerations

In summary, this chapter presents a study of synthesis and characterization of $\text{MoO}_3:\text{xFe}$ ($x = 0, 1, 3, \text{ and } 5 \%$) and explores the influence of varying Fe content on structural and magnetic properties. The Fe-doped MoO_3 microcrystals, synthesized via a solid-state reaction, exhibit an orthorhombic structure and give rise to a secondary phase ($\text{Fe}_2(\text{MoO}_4)_3$) in the Fe-doped samples. SEM images confirm the presence of two distinct morphologies in the samples: a plate-like structure, present in all samples, and a cuboid-like morphology observed in the Fe-doped samples. EDS measurements provide insights into the elemental concentration of Mo, O, and Fe within the samples. In the Fe-doped samples, Fe is predominantly distributed homogeneously throughout the sample, with the formation of small island-like regions in $\text{MoO}_3\text{-}1\%\text{Fe}$, consisting of Fe atom clusters. Similar observations were made for $\text{MoO}_3\text{:}3\%\text{Fe}$ and $\text{MoO}_3\text{:}5\%\text{Fe}$, with a higher prevalence of island-like formations. Raman and FTIR spectroscopy are employed to identify oxygen vacancies within the structure, and this is confirmed by punctual EDS analysis.

Magnetic measurements reveal an increase in the magnetization of iron-doped samples compared to the undoped sample. As for the undoped sample, it exhibits a combination of paramagnetic and diamagnetic behavior, a phenomenon that has been previously documented in the literature [70–74]. However, the explanation for this behavior remains unclear. Our hypothesis is that this observation is linked to the formation of oxygen vacancies, which, in turn, is closely associated with the generation of Mo^{5+} ions. We believe that these Mo^{5+} ions may be responsible for this magnetic activity. To deepen our understanding of this behavior, we are conducting studies to investigate how Mo^{5+} ions influence the magnetic response of the material. To achieve this, we are synthesizing MoO_3 samples with variations in the concentration of oxygen vacancies. These variations are achieved through the modification of parameters such as time, temperature, and atmosphere during the material synthesis process.

3 Influence of Temperature and Gas Atmosphere on the Thermal Decomposition of $(\text{NH}_4)_6\text{Mo}_7\text{O}_{24}\cdot 4\text{H}_2\text{O}$ [82]

The objective of this chapter is to investigate the effect of temperature and reaction environments on formation of oxygen vacancies on MoO_3 . To accomplish this, AMH was subjected under controlled heating at temperatures of 450, 550, and 650 °C, in different environments encompassing H_2 , O_2 , and the inert gas Ar, over a 6 hours period. The thermal decomposition process took place within a quartz tube housed in a furnace, ensuring precise control over the thermal profile. Subsequent characterization of the samples involved a comprehensive analysis using various techniques, XRD, Raman spectroscopy and FTIR.

3.1 Synthesis

The samples were prepared via a two-step synthesis process, starting with tetrahydrate ammonium heptamolybdate (AHM) as the precursor compound. Initially, AHM was subjected to a heating process in a furnace at 320 °C for one hour. This was done to facilitate the evaporation of NH_4 , thereby preventing contamination of the vacuum pump that would be used in subsequent phases. Subsequently, the resulting material was transferred to furnace, where precise control over temperature, pressure, and atmosphere conditions was maintained.

Within the furnace, the samples were subjected to a series of distinct atmospheres, comprising oxygen, hydrogen, and an inert argon gas, with a flow rate of 13 standard cubic centimeters per minute (SCCM) for each. Subsequently, the pressure within the reaction chamber was adjusted to approximately 2 Pa in order to optimize the reaction conditions and to minimize deviations from excessive pressures. Once a stable pressure was achieved, the samples were subjected to temperatures of 450, 550, and 650 °C for a duration of six hours each.

3.2 Results and discussion

3.2.1 X-ray Diffraction (XRD)

Figure 12 illustrates the X-ray diffraction (XRD) pattern of the precursor samples utilized in the secondary synthesis phase, designated as AHM_320. Subsequently, Figures 13 panels a to

c, d to f, and g to i, depict samples synthesized under O₂, H₂, and inert Ar atmospheres, respectively. The pronounced sharp peaks observed in the XRD spectra suggest the presence of a well-ordered structure over a wide range.

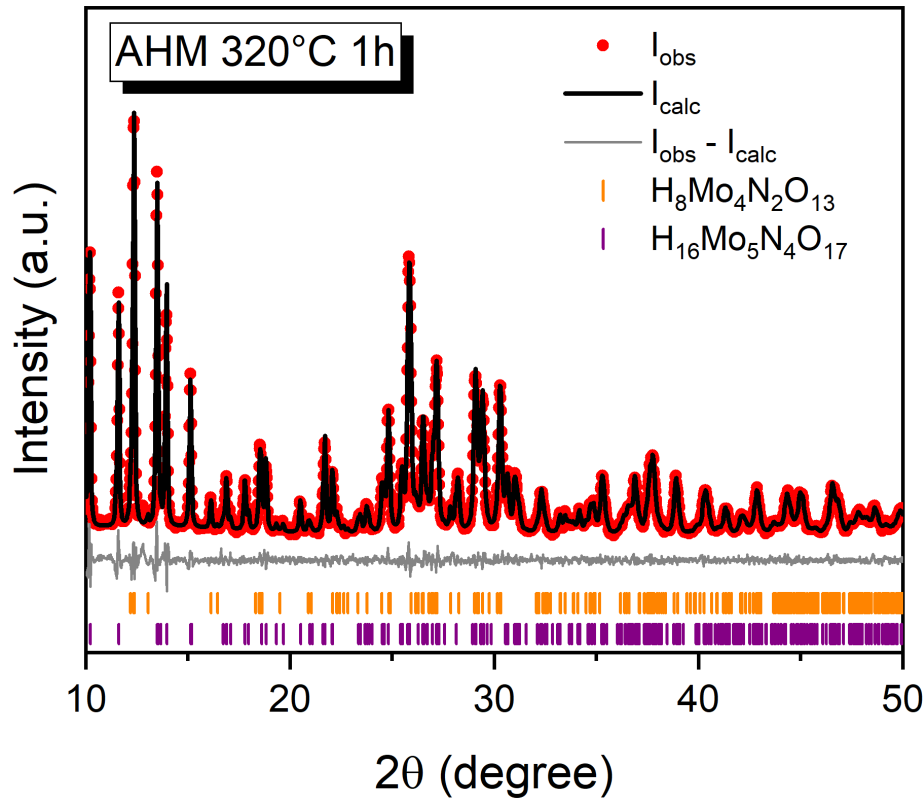


Figure 12: X-ray diffraction pattern of AHM_320 precursor sample. Figure taken from: [82].

The distinctive XRD reflections were then compared with the data set available in the Crystallography Open Database (COD), as detailed in Table 4. It is noteworthy that while the majority of samples exhibited a mixture of phases, those synthesized in an oxygen environment appeared to be predominantly single-phased. To perform a quantitative analysis of the phase composition, Rietveld refinement [113] was conducted on the diffraction patterns using the General Structure Analysis System (GSAS II) [114]. The statistical parameters, including the goodness of fit (GOF) and weighted residual, presented in Table 4, demonstrate the high quality of the refinements and the reliability of the determined phase fractions. The peaks observed in the precursor sample (Figure 12) were assigned to COD entries No. 1000271 [115] and No. 1000283 [116], respectively.

The peaks observed in the samples synthesized under oxygen conditions were identified with the Chemical Abstracts Service (CAS) number 9009669 [117]. In samples synthesized in H₂ environments at 450°C and 550°C, additional peaks were assigned to COD card No. 1521062 [113]. At 650°C, the initial MoO₃ phase appeared to undergo a transformation into MoO₂, with

peaks assigned to both Mo_4O_{11} (COD card No. 1521062) and MoO_2 (COD card No. 644064 [118]).

The X-ray diffraction (XRD) pattern of samples synthesized in an inert Ar environment at 450°C revealed the presence of a triphasic system, including an intermediate monoclinic phase of the Mo_4O_{11} compound. In addition to the aforementioned orthorhombic Mo_4O_{11} and MoO_3 phases, peaks were assigned to COD card No. 1527634 [119]. At elevated temperatures, the monoclinic phase appeared to undergo a transformation into the previously identified orthorhombic phase, as indicated by COD card No. 1521062.

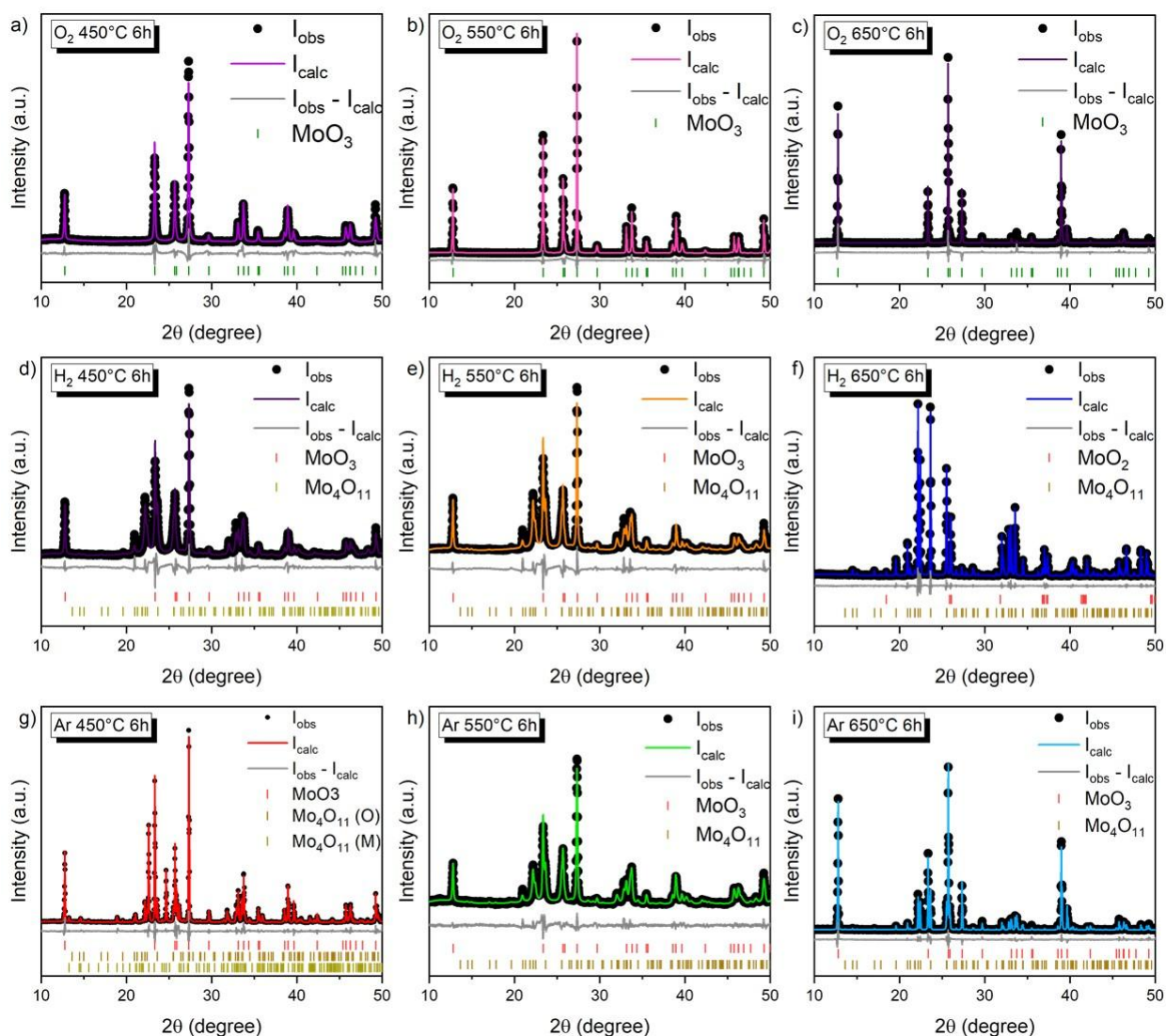


Figure 13: XRD patterns of the synthesized samples in an O_2 environment at (a) 450, (b) 550, and (c) 650 $^\circ\text{C}$ are shown. Additionally, XRD patterns of samples synthesized in an H_2 environment at (d) 450, (e) 550, and (f) 650 $^\circ\text{C}$, as well as in an inert Ar environment at (g) 450, (h) 550, and (i) 650 $^\circ\text{C}$. Figure taken from: [82].

Table 4: Sample identification, goodness of fit, and weighted residual statistical parameters facilitates the identification of phases, the composition of which is determined within the sample, as well as COD card numbers. Table taken from: [82]:

Sample	GOF	R_{wp}	Phases	Phase fraction	COD database card number
AHM 320 °C 1 h	1.69	5.317	$H_8Mo_4N_2O_{13}$	61.1	1000283
			$H_{16}Mo_5N_4O_{17}$	38.9	1000271
O ₂ 450 °C 6 h	3.16	10.943	MoO ₃	100	9009669
O ₂ 550 °C 6 h	3.36	11.336	MoO ₃	100	9009669
O ₂ 650 °C 6 h	3.83	17.742	MoO ₃	100	9009669
H ₂ 450 °C 6 h	4.19	11.993	MoO ₃	56.2	9009669
			Mo ₄ O ₁₁ (M)	43.8	1527634
H ₂ 550 °C 6 h	4.71	12.249	MoO ₃	56.3	9009669
			Mo ₄ O ₁₁ (M)	43.7	1527634
H ₂ 650 °C 6 h	2.44	7.400	MoO ₂	12.2	1548687
			Mo ₄ O ₁₁ (M)	87.8	1527634
Ar 450 °C 6 h	3.46	9.846	MoO ₃	64.8	9009669
			Mo ₄ O ₁₁ (M)	25.2	1527634
			Mo ₄ O ₁₁ (O)	10.0	1521062
Ar 550 °C 6 h	2.09	7.848	MoO ₃	49.6	9009669
			Mo ₄ O ₁₁ (M)	50.4	1527634
Ar 650 °C 6 h	2.86	11.257	MoO ₃	71.4	9009669
			Mo ₄ O ₁₁ (M)	28.6	1527634

3.2.2 Raman spectroscopy

The Raman spectra of the synthesized samples is presented in Figure 14. Figure 14 (a) corresponds to the precursor samples used in the secondary phase of synthesis (AHM_320). Figures 14 (b-d) respectively show spectra from samples synthesized in O₂, H₂, and inert Ar environments. The observed Raman peak positions and their molecular assignments are detailed

in Table 2 (section 2.2.3). In samples synthesized under O₂ conditions, the Raman spectra reveal 12 distinct peaks consistent with the orthorhombic phase of MoO₃ (α -MoO₃), as documented in literature [90]. Conversely, in samples synthesized under H₂ conditions, the formation of α -MoO₃ occurs specifically at 550 °C. At 450 and 650 °C, the Raman spectra indicate the presence of α -MoO₃ with characteristic MoO₄ vibrational modes [120,121], and MoO₂ phases [122,123], respectively.

Samples synthesized in an inert Ar environment at 450 °C exhibit a Raman spectrum similar to those synthesized under H₂ at the same temperature, indicating a comparable phase mixture. However, at higher temperatures (550 and 650°C), the Raman spectra of Ar_550 and Ar_650 samples prominently display characteristic peaks of the α -MoO₃ phase. These findings align well with the results obtained from XRD analysis.

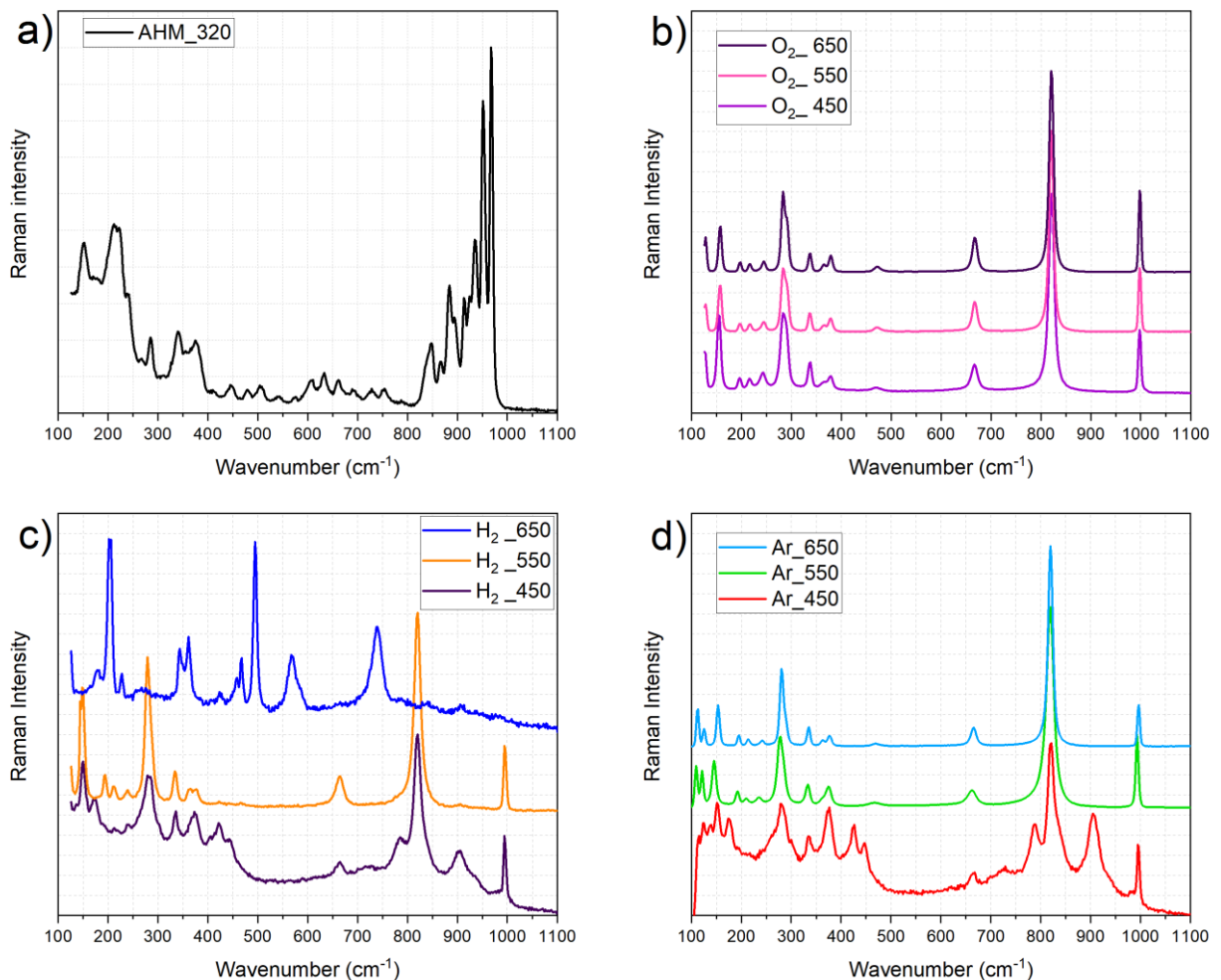


Figure 14: Raman spectra of the precursor utilized in the secondary phase of the synthesis (AHM_320) and the synthesized samples in environments containing (b) O₂, (c) H₂, and (d) Ar. Figure taken from: [82].

At 550 °C, molybdenum trioxide (MoO_3) production has been identified as pivotal, even under conditions with reduced oxygen levels. Therefore, a comparative analysis was conducted among materials synthesized at this temperature in O_2 , H_2 , and Ar environments to determine the optimal sample set for magnetic study. Figure 15 (a) presents the Raman spectra comparison for the H_2 _550, Ar_550, and O_2 _550 samples. To highlight changes in the spectra, Figure 15 (b) zooms into specific regions denoted as "Lattice" (125 - 250 cm^{-1}), "285/290" (240 - 320 cm^{-1}), and "820" (780 - 860 cm^{-1}).

Comparing the O_2 _550 sample with H_2 _550 and Ar_550 samples, a noticeable shift in peak positions towards lower wavenumbers in the "Lattice" region is observed, marked by dashed lines indicating peak positions in each sample. This shift suggests the formation of a secondary phase in the H_2 _550 and Ar_550 samples. Another distinguishable feature is the ratio of peak intensities at 285 and 290 cm^{-1} (285/290 region), which is indicative of the oxygen/molybdenum ratio [102]. This ratio shows variations due to the absence of oxygen in Ar and H_2 environments. Furthermore, the peak at 820 cm^{-1} (related to symmetric bonding of terminal oxygen), known to be sensitive to oxygen vacancies according to Isaias and Dieterle [78,102], also exhibits differences among the samples, supporting previous observations. However, detailed investigations are necessary to accurately quantify oxygen vacancies and determine the oxygen/molybdenum ratios [78].

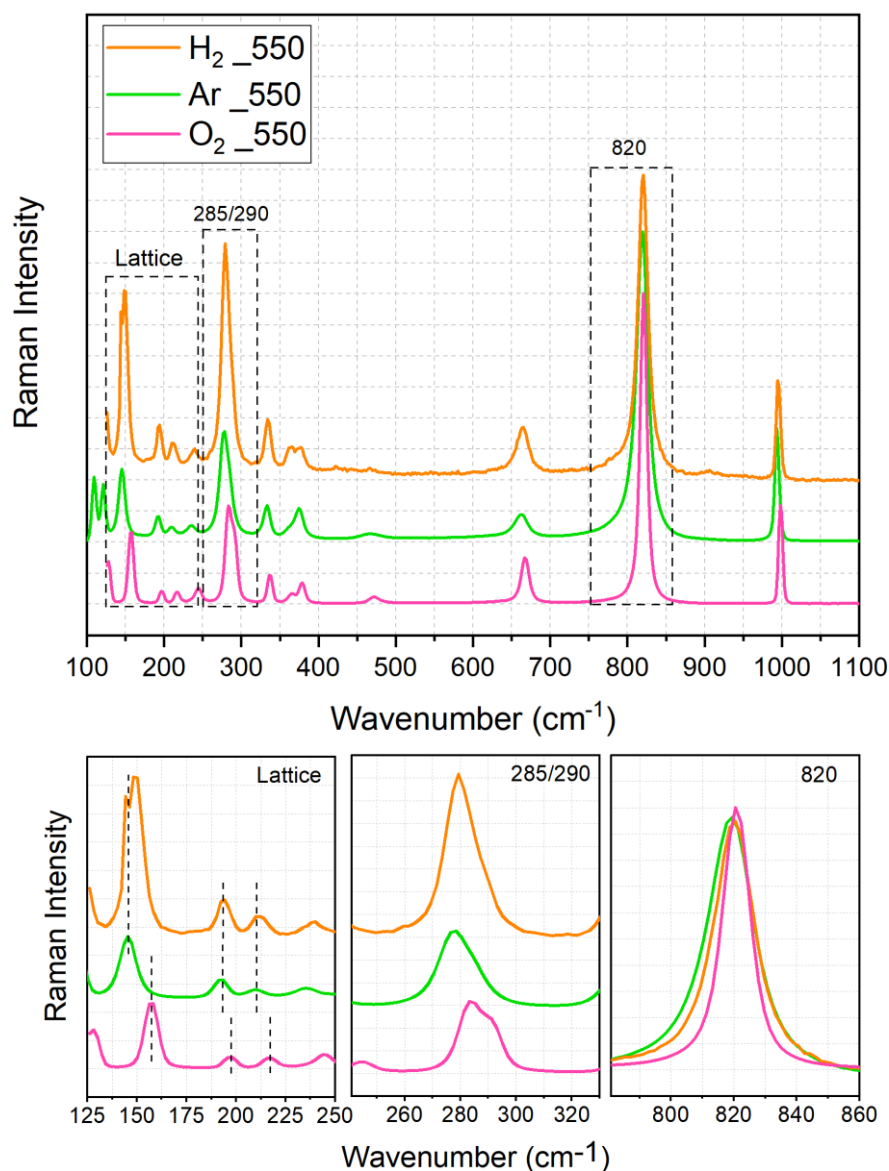


Figure 15: comparison of the Raman spectra for samples O₂_550, H₂_550, and Ar_550, with emphasis on three specific regions, is provided: (1) the lattice region at 125–250 cm⁻¹, (2) the 285/290 cm⁻¹ region at 230–330 cm⁻¹, and (3) the 820 cm⁻¹ region at 790–860 cm⁻¹ Figure taken from: [82].

3.2.3 Fourier Transform Infrared spectroscopy (FTIR)

Figure 16 depicts the FTIR spectra of the synthesized samples. Figure 16 (a) depicts the spectrum of AHM_320, while Figures 16 panels b to d illustrate the spectra of samples synthesized under O₂, H₂, and Ar environments, respectively. The spectra display bands between 967 and 983 cm⁻¹ and 809 and 850 cm⁻¹, which are indicative of the orthorhombic phase of MoO₃. These bands are attributed to the Mo=O stretching vibration and the stretching mode of Mo–O–Mo, respectively [38,106,107]. All spectra exhibit the characteristic FTIR features of α-MoO₃, thereby

confirming the predominant phase present in the samples. Notably, the AHM_320 spectrum exhibits bands that are consistent with the precursor nature of AHM. The H₂_650 spectrum displays bands characteristic of MoO₂, which aligns with findings from Raman and XRD analyses. These analyses indicate that the MoO₂ phase forms at higher temperatures under a hydrogen atmosphere [124–127]. This consistency across FTIR, Raman, and XRD spectra serves to reinforce the phase identification and synthesis conditions of the materials under study.

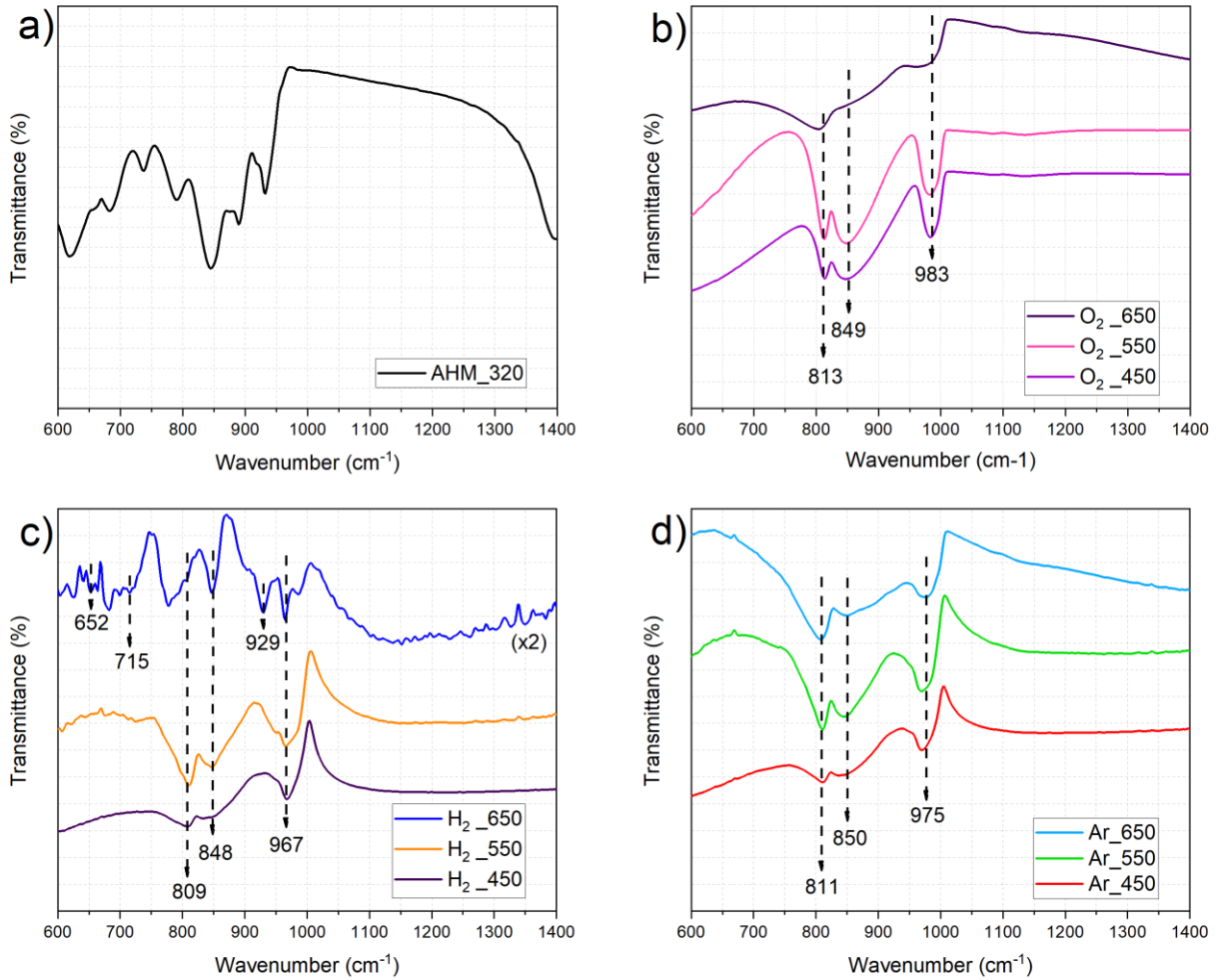


Figure 16: FTIR spectra of the precursor utilized in the secondary phase of the synthesis (AHM_320) and the resulting samples in environments containing (b) O₂, (c) H₂, and (d) Ar. Figure taken from: [82].

Figure 17 presents a comparative analysis of samples synthesized at 550 °C in three distinct environments, employing a methodology analogous to that employed in the Raman analysis. Upon examination of the spectra, it becomes evident that the band at 813 cm⁻¹ remains consistent across the O₂_550, H₂_550, and Ar_550 samples. However, the bands at 850 cm⁻¹ and 981 cm⁻¹ exhibit a notable shift towards lower wavenumbers in the H₂_550 and Ar_550 samples in comparison to the O₂_550 sample. As indicated in the literature, the band at 965–983 cm⁻¹ is

attributed to the stretching vibration of Mo=O bonds, which is characteristic of the layered orthorhombic phase where oxygen atoms are not shared [38,106]. In contrast, the band at 850 cm^{-1} is linked to the presence of oxygen atoms bridging two octahedral units (Mo-O-Mo) [107]. Therefore, the observed differences among the samples are primarily manifested in these two spectral regions. The observed spectral shifts indicate variations in the bonding environments and structural configurations of the molybdenum oxide phases synthesized under different gas atmospheres. The stability of the band at 813 cm^{-1} indicates the presence of a consistent structural element across all samples. In contrast, the shifts observed in the other bands reflect differences in oxygen bonding and coordination states, which are influenced by the synthesis environment.

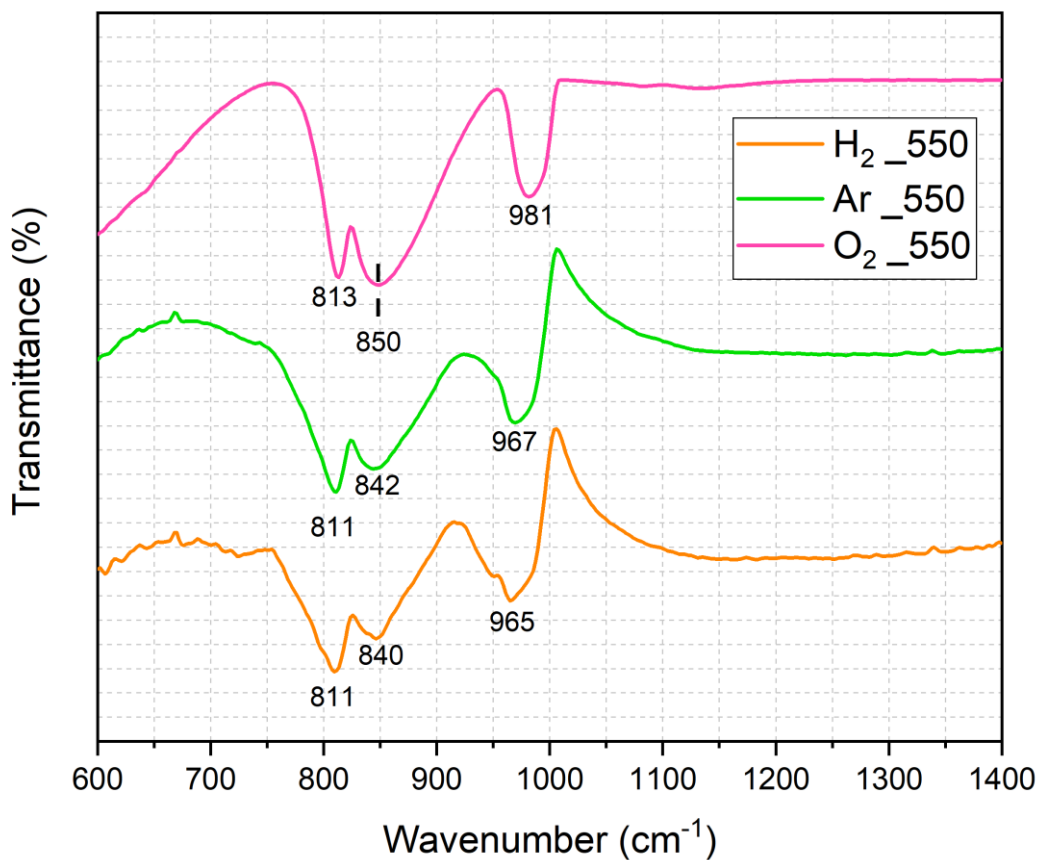


Figure 17: Comparison of Raman spectra of the samples O₂_550, H₂_550, and Ar_550. Figure taken from: [82].

3.2.4 Vibrating-sample magnetometer (VSM)

Figure 18 illustrates the magnetic properties of MoO₃ particles synthesized under distinct gas environments (H₂_550, O₂_550, and Ar_550), as quantified by a vibrating sample magnetometer (VSM, Dynacool, Quantum Design). The magnetization curves were obtained after background subtraction relative to the powder sample holder connected to the brass sample holder.

In general, the magnetic signals from the samples are relatively weak. The H₂_550 and O₂_550 samples display the hallmarks of paramagnetic behavior, as evidenced by a linear magnetization curve. In contrast, the Ar_550 sample evinces paramagnetic behavior with a modest ferromagnetic contribution, as indicated by the presence of hysteresis and a coercivity of approximately 250 Oe.

A comparison of the magnetization values of the three samples reveals that the Ar_550 sample exhibits the highest magnetization, followed by the H₂_550 sample and then the O₂_550 sample. It is important to note that attributing the observed magnetic behavior solely to the composition or synthesis environment of MoO₃ is challenging due to the presence of a secondary phase (Mo₄O₁₁(M)), particularly in the Ar_550 (50.4%) and H₂_550 (43.7 %) samples. However, it is observed that as the quantity of the secondary phase increases, there is a corresponding increase in the magnetization of the material. It can thus be concluded that the enhanced magnetic responses observed in the Ar_550 and H₂_550 samples are likely attributed to the contribution of the Mo₄O₁₁(M) phase. This indicates that the presence and proportion of the secondary phase affect the magnetic properties of the synthesized MoO₃ particles in different gas environments.

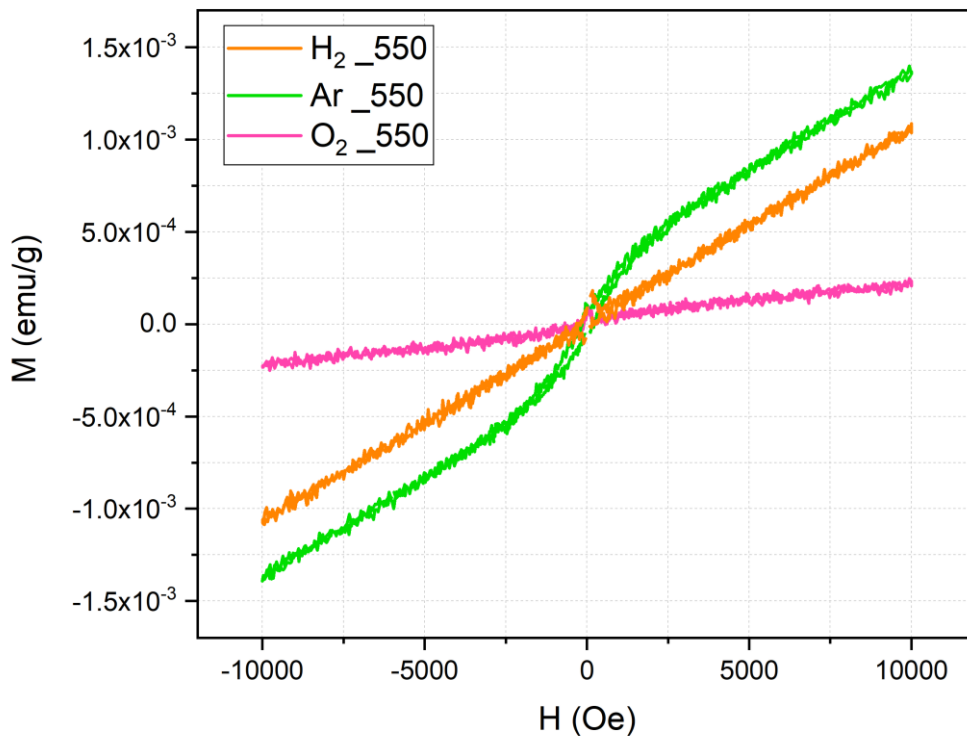


Figure 18: Magnetic curve of the samples O₂_550, H₂_550, and Ar_550. Figure taken from: [82].

3.3 Final considerations

This study examines the influence of temperature and gas atmosphere on the thermal decomposition of HMA. The atmospheres under investigation included H₂, O₂, and Ar at temperatures of 450, 550, and 650 °C. The synthesis method employed influenced the materials obtained within the same temperature range. It was observed that the composition of the resulting products, which consisted of molybdenum oxides with varying stoichiometries, was strongly dependent on the reactive atmosphere and the specific temperature applied. In the O₂ environment, the most efficient formation of the orthorhombic phase of MoO₃ occurred without the formation of additional phases. Conversely, environments containing H₂ and Ar led to the formation of the Mo₄O₁₁ phase in conjunction with MoO₃, with the exception of samples produced in H₂ at 650 °C, where MoO₃ was completely reduced to MoO₂, resulting in a phase mixture with Mo₄O₁₁. The proportion of the Mo₄O₁₁ phase produced varied with each gas environment and temperature, influencing the magnetic properties of the resultant material.

The sample synthesized in an O₂ environment at 550 °C exhibits a lower magnetization compared to samples synthesized in H₂ and Ar at the same temperature. However, it is unclear whether this difference is due to modifications of ions in MoO₃ or due to the presence of a second phase found in the samples. In light of the aforementioned results from Raman, X-ray diffraction (XRD), and Fourier-transform infrared spectroscopy (FTIR), it can be concluded that the O₂ environment is the most suitable for the study of magnetic properties dependent on Mo⁶⁺ and Mo⁵⁺ ions in MoO₃. Further adjustments of parameters are necessary to obtain a wider range of different samples. Consequently, in the subsequent phase of the study, MoO₃ will be synthesized through thermal decomposition of AHM in an O₂ environment, with the parameters of time and temperature being varied.

4 Investigating Paramagnetic to Diamagnetic Transition in MoO₃: Controlled Synthesis and Characterization [128]

This chapter investigates the transition from paramagnetic to diamagnetic behavior in MoO₃, a phenomenon documented in previous literature where MoO₃'s magnetic response shifts from paramagnetic at low fields to diamagnetic at high fields. To explore this phenomenon, MoO₃ samples were synthesized with controlled Mo⁶⁺ and Mo⁵⁺ concentrations while maintaining high crystallinity. These samples were prepared in furnace under an oxygen environment at temperatures of 550 and 650 °C for durations of 4 and 8 hours. Characterization of the resulting samples was conducted using powder XRD, XPS, and VSM.

4.1 Synthesis

The MoO₃ samples were synthesized via a two-stage process involving the thermal decomposition of AHM. In the initial stage, AHM was heated to 320 °C and maintained for one hour to facilitate the evaporation of ammonia and prevent the potential contamination of the subsequent process equipment. Subsequently, in the second stage, the processed sample was introduced into a furnace and heated at temperatures of 525 and 625 °C for durations of 4 and 8 hours at each temperature, respectively.

The synthesis process was conducted in an oxygen-rich environment, with an oxygen concentration of 13 standard cubic SCCM and a pressure of 2 Torr. These parameters were meticulously selected to ensure the formation of α -MoO₃ with high crystallinity and purity, as previously reported. The resulting samples were designated as 525C_4h, 525C_8h, 625C_4h, and 625C_8h, respectively, based on their synthesis time and temperature conditions.

4.2 Results and discussion

4.2.1 X-ray Diffraction (XRD)

Figure 19 depicts the X-ray diffraction (XRD) patterns of the synthesized samples, which were analyzed at room temperature. All diffraction peaks are in precise correspondence with those of orthorhombic MoO₃ (α -MoO₃) with the space group Pbnm, as corroborated by COD card No.

9009669 [117]. The absence of additional phases and the presence of sharp, well-defined peaks indicate a high degree of structural order and long-range crystallinity.

Figure 19 (a) offers a comparative view of the diffraction peaks for the four samples. To facilitate the visualization of alterations in the XRD patterns, the regions delineated by dashed squares in Figure 19 (a) have been magnified and presented in Figures 19 (b, c). These figures focus on the (020) and (101) planes, respectively. It is anticipated that variations in the peaks along the b-axis will occur as a result of modifications introduced during the synthesis process. These peaks reflect the anisotropic growth of the structure, which is attributed to the stacking of MoO_6 octahedral layers. It is possible that these layers may vary under different synthesis conditions. The observed slight modifications in all directions suggest changes in the a, b, and c lattice parameters, which are likely associated with the formation of Mo^{5+} ions, as corroborated by the XPS results (Figure 20).

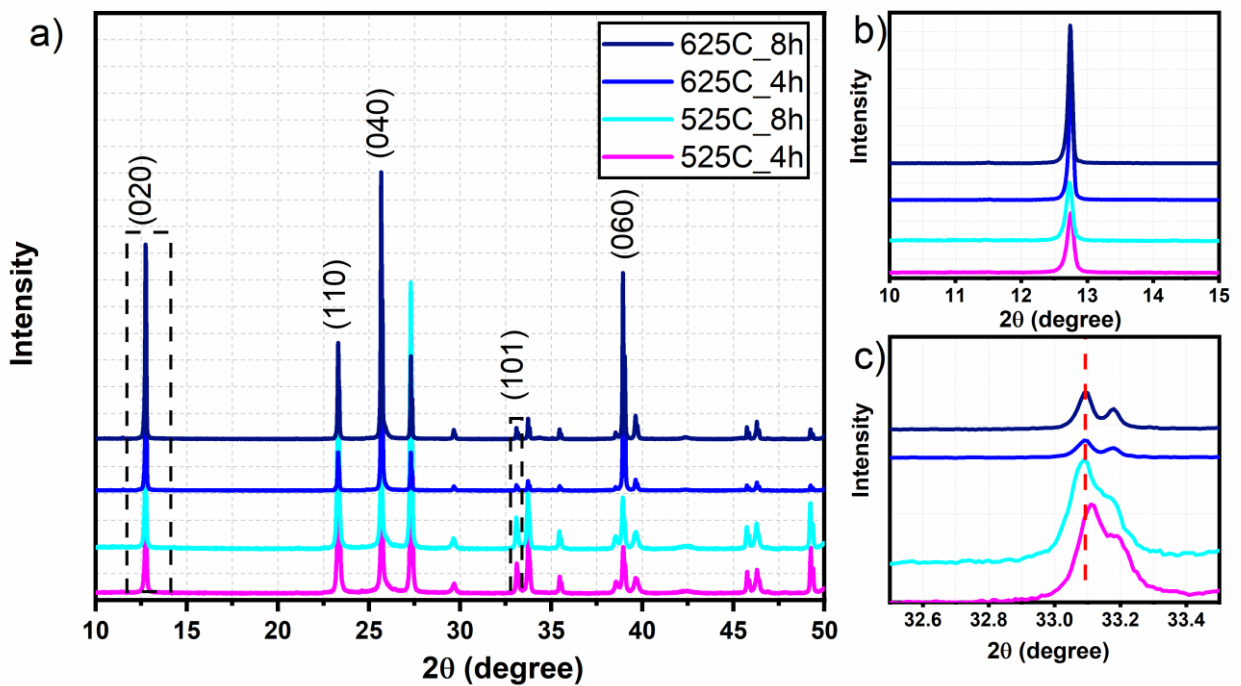


Figure 19: XRD pattern of $\alpha\text{-MoO}_3$ of a) all samples and high magnification of b) (020) and c) (101) peaks. Figure taken from: [128].

A comparison of the (101) peak positions reveals a slight variation in the position for sample 525C_4h relative to the other samples (525C_8h, 625C_4h, and 625C_8h). This shift may be attributed to the formation of Mo^{5+} ions, which are larger than Mo^{6+} ions and lead to an expansion in the coordination environment [75]. As a result, peaks in samples with higher concentrations of Mo^{5+} ions shift towards lower 2θ values. These observations are corroborated by the XPS analyses presented in section 4.2.2.

4.2.2 X-ray photoelectron spectroscopy (XPS)

X-ray photoelectron spectroscopy (XPS) was employed for the analysis of the chemical composition of the MoO₃ samples. Figure 20 presents the XPS spectra for the four samples, confirming the presence of molybdenum (Mo), oxygen (O), and carbon (C) in all samples. The Mo 3d orbital exhibits spin-orbit coupling, which results in the emergence of two distinct components. The Mo 3d_{5/2} and Mo 3d_{3/2} orbitals are separated by an energy difference (Δ) of 3.18 eV and exhibit a relative intensity ratio of 0.67, which reflects the respective probabilities of the two components. The binding energies for these components are 233 eV for Mo 3d_{5/2} and 236 eV for Mo 3d_{3/2} [129,130].

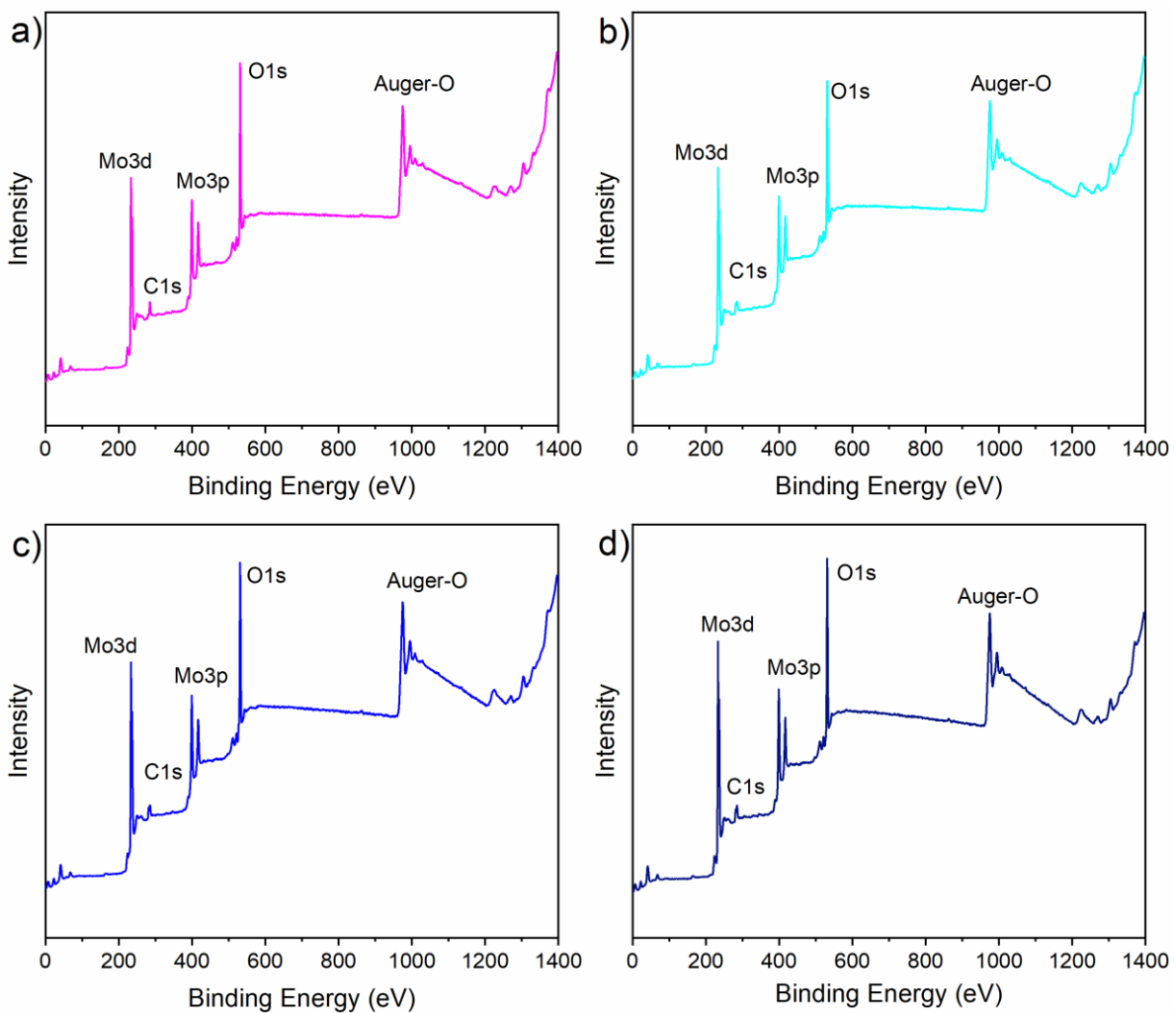


Figure 20: XPS spectra for a) 525C_4h, b) 525C_8h, c) 625C_4h, and d) 625C_8h samples. Figure taken from: [128].

Figure 21 presents a high-resolution view of the peaks along with their deconvolution. Each peak can be deconvoluted into three distinct components, as detailed in Table 5, which

provides the positions and corresponding oxidation states of these components. Figure 21 additionally demonstrates the manner in which the intensity of the peaks fluctuates in response to temperature and synthesis time. Table 6 illustrates the areas of the deconvoluted peaks, which facilitates the estimation of the concentration of each ionization state across the samples. As anticipated, the concentration of the Mo^{4+} peak is notably lower than that of the others. As stated by Rellán-Piñero *et al.* [44], as well as density functional theory calculations and X-ray photoelectron spectroscopy (XPS), demonstrate that $\alpha\text{-MoO}_3$ can manifest two distinct vacancy configurations. In the first configuration, two Mo^{5+} centers are formed, resulting in an oxygen vacancy configuration ($\text{Mo}^{5+} \oplus$) with a neighboring cation acquiring a 5+ character ($\text{Mo}^{5+} \oplus(\text{O})\text{-Mo}^{5+} \oplus(=\text{O})$). In the second configuration, a single doubly reduced Mo^{4+} ion is present. The stoichiometric ratio between Mo^{5+} and Mo^{4+} is approximately 93:7, as reported in reference [44].

Moreover, the Mo^{4+} peak area remains largely unaltered across all four samples, suggesting that Mo^{4+} has a negligible influence on the observed structural alterations and magnetic characteristics. In light of these observations, the subsequent analysis will focus on the Mo^{6+} and Mo^{5+} peaks. A review of Table 6 reveals a clear correlation between synthesis time and temperature with the concentration of Mo^{5+} peaks. As both synthesis time and temperature increase, the concentration of Mo^{5+} peaks rises, while the concentration of Mo^{6+} peaks declines. These trends align with the findings of the XRD analysis.

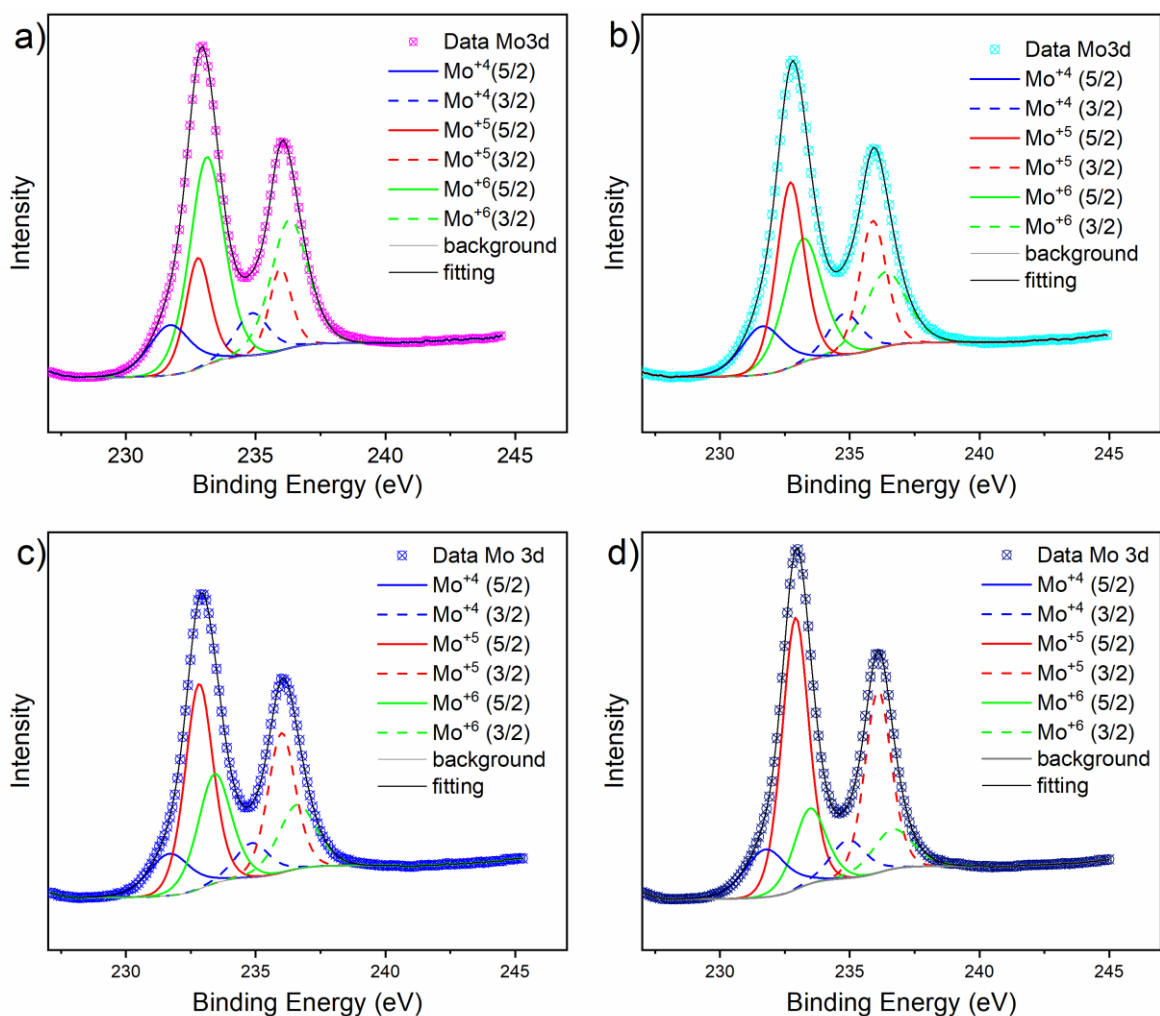


Figure 21: XPS spectra of Mo_{3d} and peaks decomposition for a) 525C_4h, b) 525C_8h, c) 625C_4h, and d) 625C_8h samples. Figure taken from: [128].

Table 5: The positions of the ionization states Mo⁴⁺, Mo⁵⁺, and Mo⁶⁺ in the Mo_{3d}_{3/2} and Mo_{3d}_{5/2} peaks are observed at 231 and 236 eV, respectively. Table taken from: [128].

Samples	Position of peaks (eV)					
	Mo ⁴⁺ (5/2)	Mo ⁴⁺ (3/2)	Mo ⁵⁺ (5/2)	Mo ⁵⁺ (3/2)	Mo ⁶⁺ (5/2)	Mo ⁶⁺ (3/2)
525C_4h	231.69	234.87	232.77	235.95	233.12	236.30
525C_8h	231.63	234.81	232.71	235.89	233.20	236.38
625C_4h	231.68	234.86	232.82	235.99	233.42	236.60
625C_8h	231.76	234.94	232.91	236.09	233.47	236.65

Table 6: concentration of the areas corresponding to the ionization states Mo⁴⁺, Mo⁵⁺, and Mo⁶⁺ in the Mo₃d peak at 231 and 236 eV is expressed as a percentage. Table taken from: [128].

Samples	Concentration of Mo3d peaks (%)					
	Mo ⁴⁺ (5/2)	Mo ⁴⁺ (3/2)	Mo ⁵⁺ (5/2)	Mo ⁵⁺ (3/2)	Mo ⁶⁺ (5/2)	Mo ⁶⁺ (3/2)
525C_4h	10.47	7.01	13.70	9.18	35.71	23.93
	17.48		22.88		59.64	
525C_8h	10.20	6.84	26.08	17.47	23.60	15.81
	17.04		43.55		39.41	
625C_4h	9.44	6.33	30.83	20.66	19.60	13.14
	15.77		51.49		32.74	
625C_8h	10.27	6.88	37.21	24.93	12.40	8.31
	17.15		62.14		20.71	

4.2.3 Fourier Transform Infrared spectroscopy (FTIR)

Figure 22 depicts the FTIR spectra of synthesized samples in the range of 400 to 1100 cm⁻¹. The spectra exhibit five prominent vibrational bands at 440, 569, 813, 848, and 981 cm⁻¹, which are indicative of the orthorhombic crystal structure of MoO₃ [131]. The band at 981 cm⁻¹ corresponds to Mo=O stretching, thereby confirming the presence of the layered orthorhombic phase [38,106]. The crystallinity of the samples synthesized at 525 °C is indicated by a sharper appearance of the band. In comparison, those produced at 625 °C display a broader band, suggesting that the synthesis temperature influences the crystallinity. The most intense band, observed at 848 cm⁻¹, is associated with the stretching mode of oxygen in Mo-O-Mo bonds, as previously reported in the literature [38,43,90,107,108]. In the samples synthesized at 625 °C, the intensity of this band is observed to decrease in comparison to the other bands. However, its position remains consistent across all samples, indicating that there is no shift in wavenumber. It is noteworthy that the peak at 813 cm⁻¹, which also corresponds to Mo-O-Mo bonds [38,43,90,107,108], exhibits a significant shift to lower wavenumbers in samples synthesized at 625 °C compared to those produced at 525 °C. Lastly, the band at 569 cm⁻¹ is attributed to the oxygen atom bonded to three molybdenum atoms [38,108]. These observations indicate that while

the synthesis temperature influences the crystallinity and specific vibrational modes, it does not affect the orthorhombic phase of the MoO₃ crystal structure.

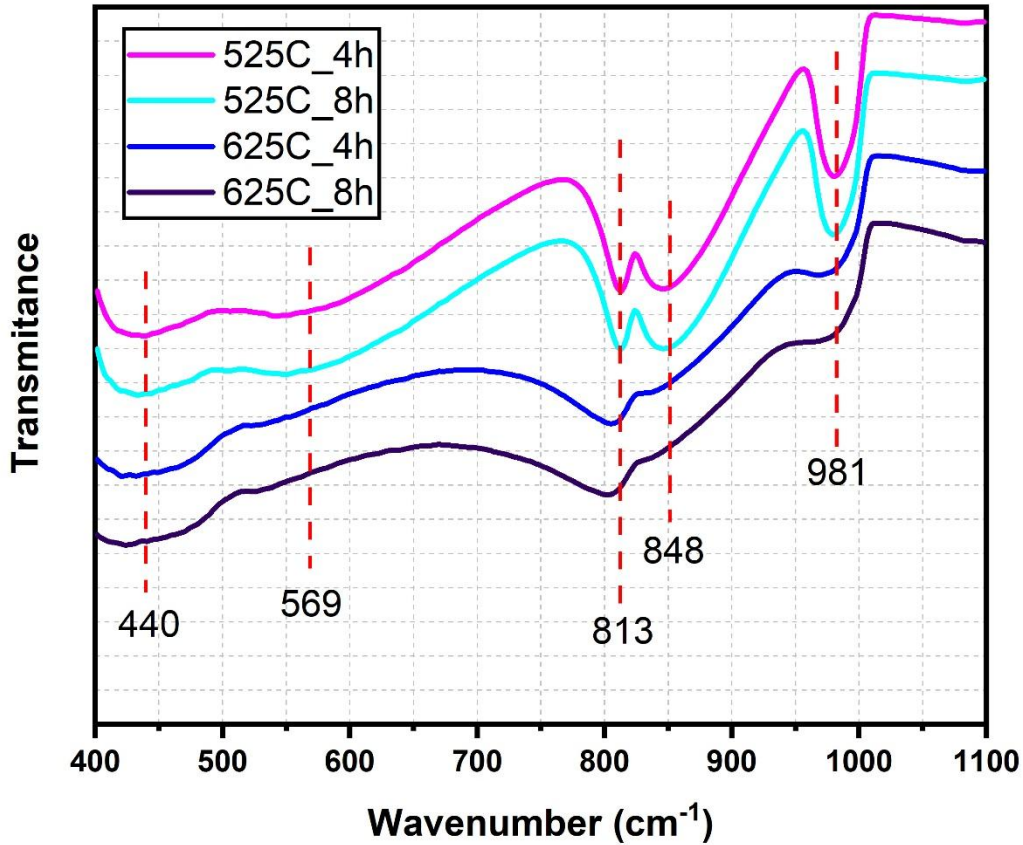


Figure 22: FTIR spectra of synthesized α -MoO₃. Figure taken from: [128].

4.2.3 Raman spectroscopy

In Figure 23 (a) shows the Raman spectra of the synthesized samples. The spectra show 15 peaks corresponding to the α -MoO₃ phase [90]. These results agree with the literature [82,90,131] and confirm the results of FTIR and XRD analyses. All these results are in agreement with section 2.2.3 and summarized in Table 2.

The XRD and FTIR analyses indicate that there have been structural changes in the MoO₃ crystal, which are associated with the concentration of Mo⁵⁺ ions present in the samples. It can be reasonably deduced that alterations in the intensity ratio of the Raman peaks at 285 and 290 cm⁻¹

, as well as changes in the full width at half maximum (FWHM) of the Raman peak at 820 cm^{-1} , will occur due to their sensitivity to oxygen vacancies [78,102]. One potential explanation for these observations is intervalent charge transfer (IVCT), which occurs near the 633 nm laser excitation energy, as detailed in [78,102]. However, only minor variations were observed in the intensity ratios of the 285/290 peaks and in the FWHM of the 820 cm^{-1} peaks across the samples (Table 7). As stated by Dieterle *et al.* [102], a ratio of less than 2.47 between the two peaks makes it challenging to distinguish between them, necessitating the use of supplementary techniques to ascertain the quantity of oxygen vacancies and the formation of Mo^{5+} ions.

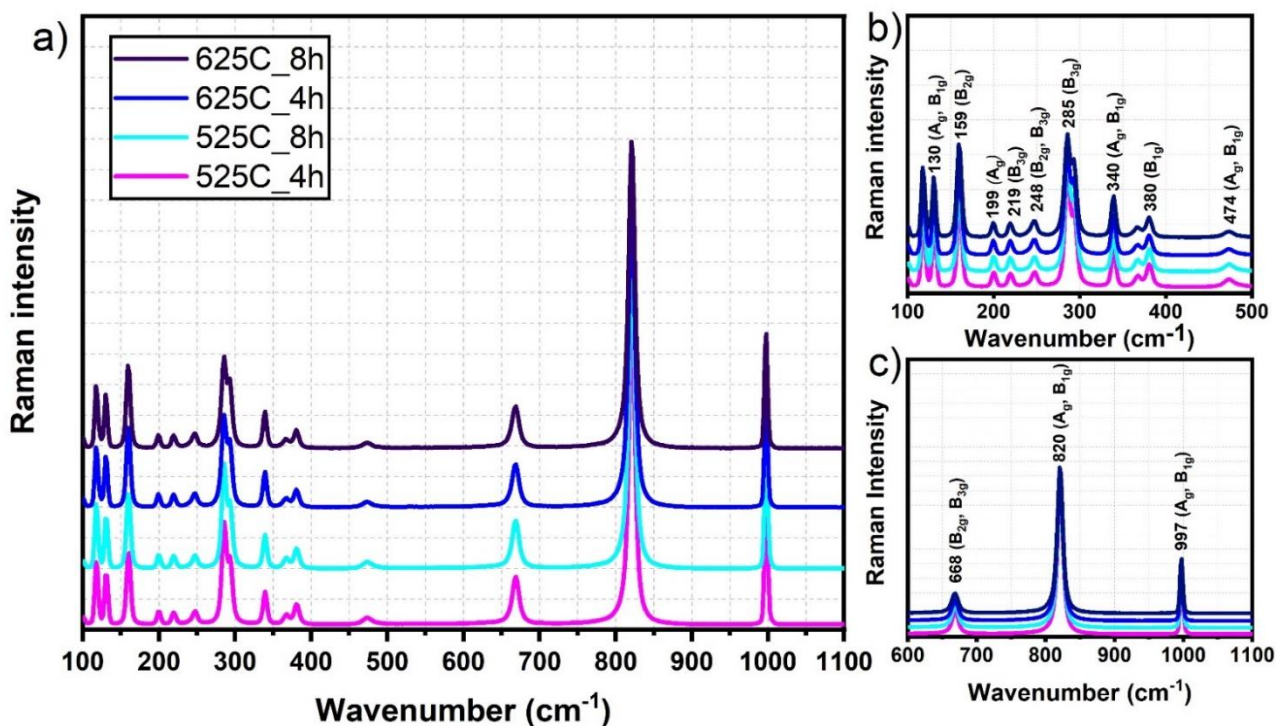


Figure 23: Raman spectra of $\alpha\text{-MoO}_3$, showing a) spectra of all samples and high magnification of regions b) 100-500 cm^{-1} and c) 600-1100 cm^{-1} , along with the corresponding phonon modes associated with each peak. Figure taken from: [128].

Table 7: ratio of peak intensities at 285 cm^{-1} and 290 cm^{-1} , as well as the full width at half maximum (FWHM) of the peaks at 668 cm^{-1} , were evaluated. Table taken from: [128].

Samples	Intensity peak ratio of 285/290	FWHM of peak at 668 cm^{-1}
525C_4h	1.46	11.44
525C_8h	1.28	11.14
625C_4h	1.12	11.08
625C_8h	1.01	10.96

4.2.4 Vibrating-sample magnetometer (VSM)

Figure 24 illustrates the findings of magnetic studies conducted on a range of MoO_3 samples synthesized for this purpose. Given the relatively weak magnetic signal of MoO_3 , the magnetism of each empty sample holder (SH) was recorded initially as a baseline measurement. Subsequently, measurements were conducted with the sample positioned on the sample holder (S+SH), followed by the subtraction of the background signal from the SH. Figure 24 (a) depicts the M-H hysteresis curves for the empty sample holder (SH), while Figure 24 (b) illustrates the curves for the sample holder containing 525C_4h (S+SH). Figure 24 (c) illustrates the magnetization of 525C_4h after background subtraction. The same methodology was subsequently employed for the remaining samples, and Figure 24 (d) depicts the hysteresis curves for 525C_4h, 525C_8h, 625C_4h, and 625C_8h following background subtraction.

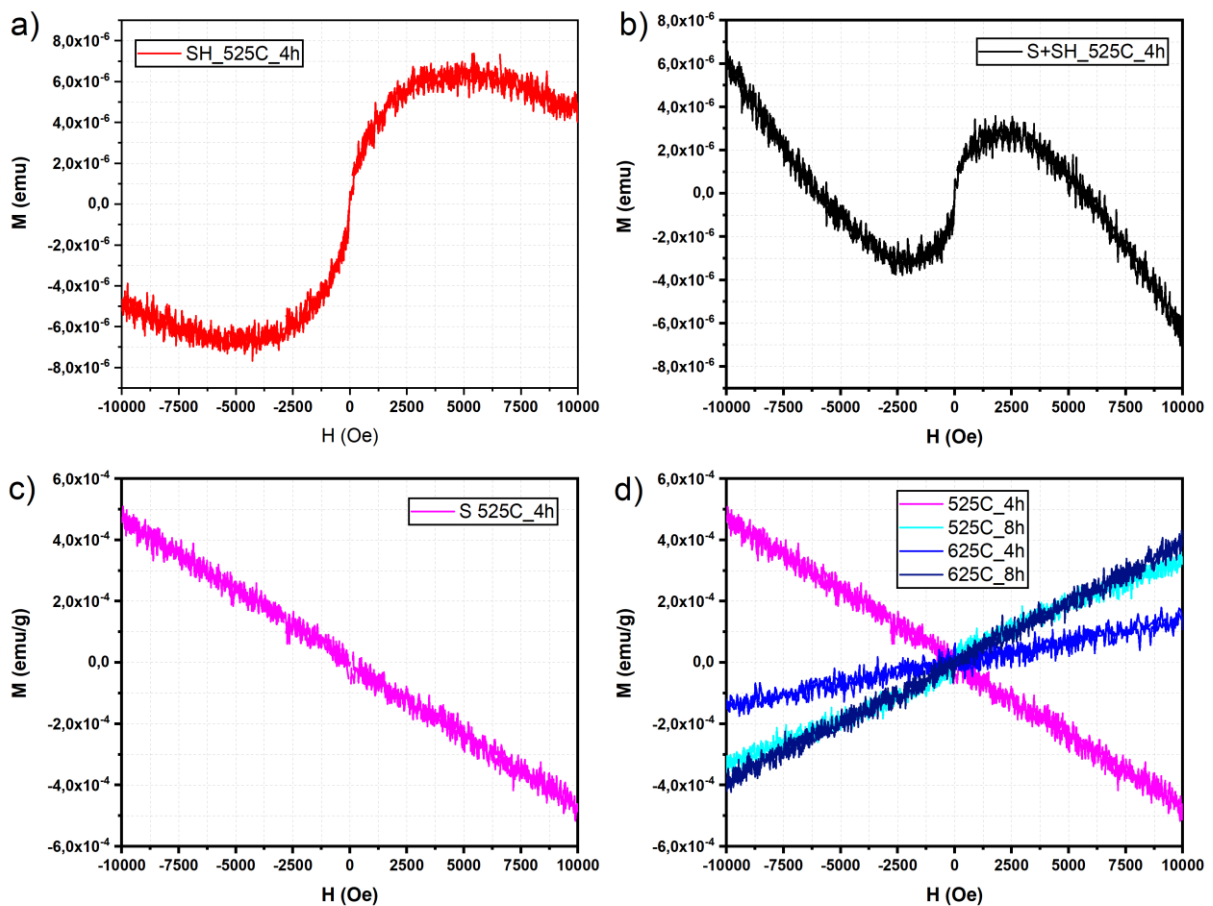


Figure 24: Magnetic curve (M-H hysteresis curves) of samples. a) Empty sample holder used to measure the sample 525C_4h, b) measurement of sample holder + 525C_4h (S+SH_525C_4h), c) 525C_4h sample (S 525_4h) after subtracting the magnetization of the sample holder. Figure taken from: [128].

A quantitative analysis of the S+SH measurements presented in Figure 24 (b) reveals that the material exhibits a paramagnetic response within the field range of -2500 to +2500 Oe. However, at higher applied field strengths, a transition to diamagnetic behavior is observed. This phenomenon has been previously reported in studies of MoO₃ [70] and other materials, such as TiO₂ [85], MoS₂ [74], C₁₂Li [71], and carbon nanotubes [73]. In the present study, the observed shift in magnetic behavior is attributed to the weak magnetic response of MoO₃, which is comparable to the diamagnetic response of the sample holder (SH). By subtracting the magnetization of the SH from the combined SH+S measurement, the intrinsic magnetization of each sample is isolated, revealing diamagnetic behavior for the 525C_4h sample and paramagnetic behavior for the other samples.

The extant literature suggests that molybdenum (Mo) in the MoO₃ structure typically exhibits a +6 oxidation state, which is generally associated with paramagnetic behavior [68,70,75]. Nevertheless, some studies have documented instances of ferromagnetic behavior, which have been attributed to non-stoichiometry in the material [68,70,75]. In the present study, both diamagnetic and paramagnetic behaviors were observed in MoO₃ (Figure 24 (d)). These magnetic properties are ascribed to the presence of Mo⁶⁺ ions and the formation of oxygen vacancies, which are directly linked to the creation of Mo⁵⁺ ions. The elevated concentration of Mo⁶⁺ in the 525C_8h sample gives rise to a paramagnetic response, whereas the elevated concentration of Mo⁵⁺ in the 525C_4h sample results in a diamagnetic response. Nevertheless, an examination of the 625C_4h and 625C_8h samples (Figure 24 (d)), which contain considerable quantities of Mo⁵⁺, still points to paramagnetic behavior. This indicates the presence of a critical concentration of Mo⁵⁺ ions, beyond which the material's magnetic properties undergo a transition, resulting in a shift from paramagnetic to diamagnetic behavior.

4.3 Final considerations

In this study the transition between paramagnetic and diamagnetic behavior in MoO₃ was examined. To clarify this transition, MoO₃ was synthesized under varying time and temperature conditions, with the objective of adjusting the Mo⁶⁺ and Mo⁵⁺ concentration in each sample. XRD analysis confirmed the successful synthesis of the material and indicated slight alterations in the diffraction patterns. FTIR revealed spectral changes associated with the synthesis temperature, while Raman spectroscopy exhibited minimal variations. XPS demonstrated that modifications in synthesis conditions effectively altered the concentrations of Mo⁶⁺ and Mo⁵⁺. The magnetic

measurements indicated that MoO₃ displays a paramagnetic response at low-applied magnetic fields, which transitions to diamagnetic at higher fields. However, after accounting for the magnetic response of the sample holder, this effect was negated, revealing a singular magnetic response. This observation can be attributed to the low-intensity magnetic signal of MoO₃, which is obscured by the sample holder's response at higher fields. Furthermore, the results of VSM indicated that the magnetic behavior of MoO₃, whether paramagnetic or diamagnetic, is dependent on the concentration of Mo⁵⁺ ions.

5 Conclusion and Future Perspectives

5.1 Conclusion

This thesis investigated the synthesis, characterization, doping, and structural modifications of molybdenum trioxide (MoO_3). Initially, MoO_3 samples doped with varying percentages of Fe were synthesized using the solid-state reaction method, and their crystalline structures were confirmed through X-ray diffraction (XRD), Raman spectroscopy, and Fourier-transform infrared (FTIR) spectroscopy, all indicating the orthorhombic phase ($\alpha\text{-MoO}_3$) with the formation of a secondary $\text{Fe}_2(\text{MoO}_3)_4$ phase. Additionally, scanning electron microscopy was employed to study the material's morphology, while its magnetic properties were analyzed using a vibrating sample magnetometer. SEM results revealed the presence of regions with high Fe concentration, attributed to the secondary phase, which increased with higher dopant concentrations. This rise in secondary phase formation, and consequently in Fe concentration, was reflected in the magnetic measurements, where the magnetization of the material increased with doping levels. However, the pure sample exhibited paramagnetic behavior, which shifted to diamagnetic as the applied magnetic field strength increased. This behavior, reported in the literature, is explained by the non-stoichiometry of this type of semiconductor (in the case of MoO_3 , due to the formation of Mo^{5+} ions). To confirm this hypothesis, pure MoO_3 samples with induced structural defects were synthesized in a chemical vapor deposition chamber, varying the time, temperature, and synthesis environment. The resulting samples were characterized by Raman spectroscopy, FTIR, XRD, XPS, and VSM. The samples' phase and purity were confirmed, and structural defects (formation of Mo^{5+} ions) were quantified. Based on the obtained results, it was inferred that the transition from paramagnetic to diamagnetic response is not related to the formation of Mo^{5+} ions within the structure, but rather to the weak magnetic intensity of the sample being confused with that of the sample holder. Nevertheless, structural defects were found to influence the magnetic response of the material: MoO_3 with a high concentration of Mo^{5+} exhibited paramagnetic behavior, whereas those with low Mo^{5+} concentration displayed diamagnetic behavior.

5.2 Future Perspectives

The results obtained for this thesis open several future perspectives with the aims to investigate the relationship between structural defects in MoO_3 , specifically the formation of oxygen vacancies, and the generation of Mo^{5+} and Mo^{4+} ions, as well as changes in crystallite size, morphology, and atomic bonding within the material. To achieve this, various MoO_3 samples will be synthesized under different temperature and time conditions to produce a diverse set of samples for analysis. Electron Paramagnetic Resonance (EPR) spectroscopy will then be employed to quantify the concentration of oxygen vacancies in each sample. Based on these vacancy concentrations, the proportion of Mo^{5+} and Mo^{4+} ions will be determined using XPS. Subsequently, XRD analysis will be conducted to assess how vacancies influence crystallite size. Finally, Raman and FTIR spectroscopy studies will examine the effects of these vacancies on atomic bonding within the material. With a well-established control over the structure of MoO_3 , the material will be further applied to the fabrication of thin films and the synthesis of MoS_2 .

6 References

- [1] COPERNICUS, Climate Data from the Copernicus Climate Change Service (C3S), (2024).
- [2] ACNUR – AGÊNCIA DA ONU PARA REFUGIADOS, Relatório global sobre refugiados 2024, (2024).
- [3] M. Huston, M. Debella, M. Dibella, A. Gupta, Green Synthesis of Nanomaterials, (2021) 1–29.
- [4] H.N.Ğ. Lu, A.A. Güngör, S.İ. Nce, Synthesis of Nanoparticles by Green Synthesis Method, 1 (2017) 6–9.
- [5] A.I. Journal, A. Gour, N.K. Jain, Advances in green synthesis of nanoparticles, *Artif. Cells, Nanomedicine, Biotechnol.* 47 (2019) 844–851. <https://doi.org/10.1080/21691401.2019.1577878>.
- [6] PATRICIA MAGALHÃES PEREIRA, ADSORÇÃO DE MOLIBDATO EM MINERAIS DE ARGILA DELAMINADOS E AMORFIZADOS., Universidade Federal do Pará - UFPA, 2012.
- [7] N. Jafari, Review of pollution sources and controls in Caspian Sea region, 2 (2010) 25–29.
- [8] H. Freeman, T. Harten, J. Springer, P. Randall, M. Ann, K. Stone, H. Freeman, T. Harten, J. Springer, P. Randall, M.A. Curran, K. Stone, I. Pollution, P.A. Critical, H. Freeman, T. Harten, J. Springer, P. Randall, M.A. Curran, K. Stone, Industrial Pollution Prevention ! A Critical Review Industrial Pollution Prevention! A Critical Review, 3289 (2012). <https://doi.org/10.1080/10473289.1992.10467016>.
- [9] S. Ui, Industrial pollutants and animal health - A review, 75 (2005).
- [10] N. Kannan, D. Vakeesan, Solar energy for future world : - A review, 62 (2016) 1092–1105. <https://doi.org/10.1016/j.rser.2016.05.022>.
- [11] M. Antoniadou, M.K. Arfanis, I. Ibrahim, P. Falaras, Bifunctional g-C₃N₄ / WO₃ Thin Films for Photocatalytic Water Purification, (2019).
- [12] A.A. Journal, Synthesis, Characterization, and Properties of Few-Layer MoO₃, (2013). <https://doi.org/10.1002/asia.201300470>.
- [13] S.M. Hong, S. Lee, H.J. Jung, Y. Yu, J.H. Shin, K. Kwon, M.Y. Choi, Simple Preparation of Anatase TiO₂ Nanoparticles via Pulsed Laser Ablation in Liquid Simple Preparation of

- Anatase TiO₂ Nanoparticles via Pulsed Laser Ablation in Liquid, (2013).
<https://doi.org/10.5012/bkcs.2013.34.1.279>.
- [14] A. Mills, S. Le Hunte, An overview of semiconductor photocatalysis, 108 (2000) 1–35.
- [15] D. Zhu, Q. Zhou, Environmental Nanotechnology, Monitoring & Management Action and mechanism of semiconductor photocatalysis on degradation of organic pollutants in water treatment: A review, Environ. Nanotechnology, Monit. Manag. 12 (2019) 100255.
<https://doi.org/10.1016/j.enmm.2019.100255>.
- [16] B. Fang, Z. Xing, D. Sun, Z. Li, W. Zhou, Hollow semiconductor photocatalysts for solar energy conversion, Adv. Powder Mater. 1 (2022) 100021.
<https://doi.org/10.1016/j.apmate.2021.11.008>.
- [17] N. Moo, E. Catalysis, Nanostructured MoO₃ for Efficient Energy and Environmental Catalysis, (n.d.) 1–26.
- [18] J. Wang, C. Liu, Preparation of 2D WO₃ Nanomaterials with Enhanced Catalytic Activities: Current Status and Perspective, (2015) 335–350.
<https://doi.org/10.1002/cben.201500014>.
- [19] A. Ayati, A. Ahmadpour, F.F. Bamoharram, B. Tanhaei, M. Mänttari, Chemosphere A review on catalytic applications of Au / TiO₂ nanoparticles in the removal of water pollutant, Chemosphere 107 (2014) 163–174.
<https://doi.org/10.1016/j.chemosphere.2014.01.040>.
- [20] A.M. Mostafa, S.A. Yousef, W.H. Eisa, M.A. Ewaida, E.A. Al-ashkar, WO₃ quantum dot: Synthesis, characterization and catalytic activity, J. Mol. Struct. 1185 (2019) 351–356.
<https://doi.org/10.1016/j.molstruc.2019.03.007>.
- [21] K. Gomathi, S. Padmanathan, A. Mossad, A.T. Rajamanickam, Construction of Ni doped MoO₃ nanostructures and their application as counter electrode in dye-sensitized solar cells, Inorg. Chem. Commun. 135 (2022) 109079.
<https://doi.org/10.1016/j.inoche.2021.109079>.
- [22] T. Wo, M. Radecka, P. Sobas, M. Wierzbicka, M.Å. Rekas, Photoelectrochemical properties of undoped and Ti-doped WO₃, 364 (2005) 85–92.
<https://doi.org/10.1016/j.physb.2005.03.039>.
- [23] N. Gavrilova, M. Myachina, D. Harlamova, V. Nazarov, Synthesis of Molybdenum Blue Dispersions Using Ascorbic Acid as Reducing Agent, (2020) 15–17.

- [24] J. D. Lee, *Química inorgânica não tão concisa*, 5 th, Edgard Blücher Ltda., 1931.
- [25] I.M. Association, *Molybdenum and its applications*, (n.d.).
- [26] Friedo Huber, Universität Dortmund, *Gmelin Handbook of inorganic Chemistry*, 8th editio, Springer-Verlag Berlin Heidelberg GmbH, 1990.
- [27] X. Yang, H. Ding, D. Zhang, X. Yan, C. Lu, J. Qin, R. Zhang, H. Tang, H. Song, Hydrothermal synthesis of MoO₃ nanobelt-graphene composites, *Cryst. Res. Technol.* 46 (2011) 1195–1201. <https://doi.org/10.1002/crat.201100302>.
- [28] C. Zollfrank, K. Gutbrod, P. Wechsler, J. Peter, Antimicrobial activity of transition metal acid MoO₃ prevents microbial growth on material surfaces, *Mater. Sci. Eng. C* 32 (2012) 47–54. <https://doi.org/10.1016/j.msec.2011.09.010>.
- [29] M.T. Greiner, L. Chai, M.G. Helander, W.M. Tang, Z.H. Lu, Metal/metal-oxide interfaces: How metal contacts affect the work function and band structure of MoO₃, *Adv. Funct. Mater.* 23 (2013) 215–226. <https://doi.org/10.1002/adfm.201200993>.
- [30] T. Ressler, J. Wienold, R.E. Jentoft, T. Neisius, Bulk Structural Investigation of the Reduction of MoO₃ with Propene and the Oxidation of MoO₂ with Oxygen, 83 (2002) 67–83. <https://doi.org/10.1006/jcat.2002.3659>.
- [31] L. Khandare, S.S. Terdale, D.J. Late, Ultra-fast α -MoO₃ nanorod-based Humidity sensor, *Adv. Device Mater.* 2 (2016) 15–22. <https://doi.org/10.1080/20550308.2016.1221605>.
- [32] K. Galatsis, Y.X. Li, W. Wlodarski, E. Comini, G. Faglia, G. Sberveglieri, Semiconductor MoO₃-TiO₂ thin film gas sensors, *Sensors Actuators, B Chem.* 77 (2001) 472–477. [https://doi.org/10.1016/S0925-4005\(01\)00737-7](https://doi.org/10.1016/S0925-4005(01)00737-7).
- [33] H. Hu, C. Deng, J. Xu, K. Zhang, M. Sun, Metastable h-MoO₃ and stable α -MoO₃ microstructures: controllable synthesis, growth mechanism and their enhanced photocatalytic activity, *J. Exp. Nanosci.* 10 (2015) 1336–1346. <https://doi.org/10.1080/17458080.2015.1012654>.
- [34] J. Song, X. Ni, D. Zhang, H. Zheng, Fabrication and photoluminescence properties of hexagonal MoO₃ rods, *Solid State Sci.* 8 (2006) 1164–1167. <https://doi.org/10.1016/j.solidstatesciences.2006.05.002>.
- [35] M. Morita, S. Toyoda, H. Kiuchi, T. Abe, K. Kumagai, T. Saida, K. Fukuda, Chromogenic Amorphous MoO₃-xNanosheets and Their Nanostructured Films for Smart Window

- Applications, ACS Appl. Nano Mater. (2021). <https://doi.org/10.1021/acsnm.1c01428>.
- [36] N. Desai, S. Mali, Chemically Grown MoO₃ Nanorods for Antibacterial Activity Study, J. Nanomed. Nanotechnol. 06 (2015) 1–8. <https://doi.org/10.4172/2157-7439.1000338>.
- [37] H.Y. Chen, H.C. Su, C.H. Chen, K.L. Liu, C.M. Tsai, S.J. Yen, T.R. Yew, Indium-doped molybdenum oxide as a new p-type transparent conductive oxide, J. Mater. Chem. (2011). <https://doi.org/10.1039/c0jm03815f>.
- [38] A. Chithambararaj, A.C. Bose, Hydrothermal synthesis of hexagonal and orthorhombic MoO₃ nanoparticles, J. Alloys Compd. 509 (2011) 8105–8110. <https://doi.org/10.1016/j.jallcom.2011.05.067>.
- [39] D. Mariotti, H. Lindström, A.C. Bose, K. Ostrikov, Monoclinic β -MoO₃ nanosheets produced by atmospheric microplasma: Application to lithium-ion batteries, Nanotechnology 19 (2008). <https://doi.org/10.1088/0957-4484/19/49/495302>.
- [40] Y. Xu, L. Xie, Y. Zhang, X. Cao, Hydrothermal synthesis of hexagonal MoO₃ and its reversible electrochemical behavior as a cathode for Li-ion batteries, Electron. Mater. Lett. (2013). <https://doi.org/10.1007/s13391-013-3030-5>.
- [41] W. Pan, R. Tian, H. Jin, Y. Guo, L. Zhang, X. Wu, L. Zhang, Z. Han, G. Liu, J. Li, G. Rao, H. Wang, W. Chu, Structure, Optical, and Catalytic Properties of Novel Hexagonal Metastable β -MoO₃ Nano- and Microrods Synthesized with Modified Liquid-Phase Processes, (2010) 6202–6208. <https://doi.org/10.1021/cm102703s>.
- [42] K. Hosono, I. Matsubara, N. Murayama, S. Woosuck, N. Izu, Synthesis of polypyrrole/MoO₃ hybrid thin films and their volatile organic compound gas-sensing properties, Chem. Mater. 17 (2005) 349–354. <https://doi.org/10.1021/cm0492641>.
- [43] L. Seguin, M. Figlarz, R. Cavagnat, J.C. Lassègues, Infrared and Raman spectra of MoO₃ molybdenum trioxides and MoO₃ · xH₂O molybdenum trioxide hydrates, Spectrochim. Acta Part A Mol. Biomol. Spectrosc. 51 (1995) 1323–1344. [https://doi.org/10.1016/0584-8539\(94\)00247-9](https://doi.org/10.1016/0584-8539(94)00247-9).
- [44] M. Rellán-Piñeiro, N. López, One Oxygen Vacancy, Two Charge States: Characterization of Reduced α -MoO₃(010) through Theoretical Methods, J. Phys. Chem. Lett. 9 (2018) 2568–2573. <https://doi.org/10.1021/acs.jpcllett.8b00536>.
- [45] A. Nirmal Paul Raj, R. Biju Bennie, C. Joel, S. Hari Kengaram, S. Daniel Abraham, Systematic analysis and the effect of Mn doping on structural, optical and magnetic

- properties of MoO₃ nanoparticles, *Solid State Commun.* 341 (2022) 114532. <https://doi.org/10.1016/j.ssc.2021.114532>.
- [46] T.A. Kerr, H. Wu, L.F. Nazar, Concurrent polymerization and insertion of aniline in molybdenum trioxide: Formation and properties of a [poly(aniline)]_{0.24}MoO₃ nanocomposite, *Chem. Mater.* 8 (1996) 2005–2015. <https://doi.org/10.1021/cm960071q>.
- [47] T.A. Kerr, F. Leroux, L.F. Nazar, Surfactant-Mediated Incorporation of Poly(p - phenylene) into MoO₃, *Chem. Mater.* 10 (1998) 2588–2591. <https://doi.org/10.1021/cm980222k>.
- [48] N. Sukpirom, C.O. Oriakhi, M.M. Lerner, Preparation of layered nanocomposites of PEO with MnPS₃, CdPS₃, and MoO₃ by melt intercalation, *Mater. Res. Bull.* 35 (2000) 325–331. [https://doi.org/10.1016/S0025-5408\(00\)00216-6](https://doi.org/10.1016/S0025-5408(00)00216-6).
- [49] A. Boukhachem, O. Kamoun, C. Mrabet, C. Mannai, N. Zouaghi, A. Yumak, K. Boubaker, M. Amlouk, Structural, optical, vibrational and photoluminescence studies of Sn-doped MoO₃ sprayed thin films, *Mater. Res. Bull.* 72 (2015) 252–263. <https://doi.org/10.1016/j.materresbull.2015.08.011>.
- [50] C.D.A. Lima, J.V.B. Moura, G.S. Pinheiro, J.F.D.F. Araujo, S.B.S. Gusmão, B.C. Viana, P.T.C. Freire, C. Luz-Lima, Co-doped α -MoO₃ hierarchical microrods: Synthesis, structure and phonon properties, *Ceram. Int.* 47 (2021) 27778–27788. <https://doi.org/10.1016/j.ceramint.2021.06.205>.
- [51] N.A. Chernova, M. Roppolo, A.C. Dillon, M.S. Whittingham, Layered vanadium and molybdenum oxides: Batteries and electrochromics, *J. Mater. Chem.* 19 (2009) 2526–2552. <https://doi.org/10.1039/b819629j>.
- [52] L. Wang, G.H. Zhang, Y.J. Sun, X.W. Zhou, K.C. Chou, Preparation of Ultrafine β -MoO₃ from Industrial Grade MoO₃ Powder by the Method of Sublimation, *J. Phys. Chem. C* (2016). <https://doi.org/10.1021/acs.jpcc.6b05982>.
- [53] I.B. Troitskaia, T.A. Gavrilova, A.P. Zubareva, D.Y. Troitskii, S.A. Gromilov, Thermal transformations of the composition and structure of hexagonal molybdenum oxide, *J. Struct. Chem.* (2015). <https://doi.org/10.1134/S0022476615020122>.
- [54] A. Chithambararaj, A.C. Bose, Investigation on structural, thermal, optical and sensing properties of meta-stable hexagonal moO₃ nanocrystals of one dimensional structure, *Beilstein J. Nanotechnol.* (2011). <https://doi.org/10.3762/bjnano.2.62>.

- [55] S.R. Dhage, M.S. Hassan, O.B. Yang, Low temperature fabrication of hexagon shaped h-MoO₃ nanorods and its phase transformation, *Mater. Chem. Phys.* (2009). <https://doi.org/10.1016/j.matchemphys.2008.10.076>.
- [56] J. V. Silveira, L.L. Vieira, J.M. Filho, A.J.C. Sampaio, O.L. Alves, A.G. Souza Filho, Temperature-dependent Raman spectroscopy study in MoO₃ nanoribbons, *J. Raman Spectrosc.* 43 (2012) 1407–1412. <https://doi.org/10.1002/jrs.4058>.
- [57] C. Cheng, A. Wang, M. Humayun, C. Wang, Recent advances of oxygen vacancies in MoO₃: preparation and roles, *Chem. Eng. J.* 498 (2024). <https://doi.org/10.1016/j.cej.2024.155246>.
- [58] K. Ye, K. Li, Y. Lu, Z. Guo, N. Ni, H. Liu, Y. Huang, H. Ji, P. Wang, Trends in Analytical Chemistry An overview of advanced methods for the characterization of oxygen vacancies in materials, *Trends Anal. Chem.* 116 (2019) 102–108. <https://doi.org/10.1016/j.trac.2019.05.002>.
- [59] J.P. Jegal, H.K. Kim, J.S. Kim, K.B. Kim, One-pot synthesis of mixed-valence MoO_x on carbon nanotube as an anode material for lithium ion batteries, *J. Electroceramics* 31 (2013) 218–223. <https://doi.org/10.1007/s10832-013-9821-0>.
- [60] Y.S. Jung, S. Lee, D. Ahn, A.C. Dillon, S.H. Lee, Electrochemical reactivity of ball-milled MoO_{3-y} as anode materials for lithium-ion batteries, *J. Power Sources* 188 (2009) 286–291. <https://doi.org/10.1016/j.jpowsour.2008.11.125>.
- [61] M. Vasilopoulou, A.M. Douvas, D.G. Georgiadou, L.C. Palilis, S. Kennou, L. Sygellou, A. Soultati, I. Kostis, G. Papadimitropoulos, D. Davazoglou, P. Argitis, The influence of hydrogenation and oxygen vacancies on molybdenum oxides work function and gap states for application in organic optoelectronics, *J. Am. Chem. Soc.* 134 (2012) 16178–16187. <https://doi.org/10.1021/ja3026906>.
- [62] X. Hou, M. Ruan, L. Zhou, J. Wu, B. Meng, W. Huang, K. Zhong, Superior lithium storage performance in MoO₃ by synergistic effects: Oxygen vacancies and nanostructures, *J. Energy Chem.* 78 (2023) 91–101. <https://doi.org/10.1016/j.jechem.2022.11.011>.
- [63] C. Cheng, A. Wang, M. Humayun, C. Wang, Recent advances of oxygen vacancies in MoO₃: preparation and roles, *Chem. Eng. J.* 498 (2024) 155246. <https://doi.org/10.1016/j.cej.2024.155246>.
- [64] H.S. Kim, J.B. Cook, H. Lin, J.S. Ko, S.H. Tolbert, V. Ozolins, B. Dunn, Oxygen vacancies

- enhance pseudocapacitive charge storage properties of MoO_{3-x}, *Nat. Mater.* 16 (2017) 454–462. <https://doi.org/10.1038/NMAT4810>.
- [65] Y. Zhang, P. Chen, Q. Wang, Q. Wang, K. Zhu, K. Ye, G. Wang, D. Cao, J. Yan, Q. Zhang, High-Capacity and Kinetically Accelerated Lithium Storage in MoO₃ Enabled by Oxygen Vacancies and Heterostructure, *Adv. Energy Mater.* 11 (2021) 1–11. <https://doi.org/10.1002/aenm.202101712>.
- [66] Q. Liu, Y. Wu, J. Zhang, K. Chen, C. Huang, H. Chen, X. Qiu, Plasmonic MoO_{3-x} nanosheets with tunable oxygen vacancies as efficient visible light responsive photocatalyst, *Appl. Surf. Sci.* 490 (2019) 395–402. <https://doi.org/10.1016/j.apsusc.2019.06.099>.
- [67] R.O. Ijeh, A.C. Nwanya, A.C. Nkele, I.G. Madiba, A.K.H. Bashir, A.B.C. Ekwealor, R.U. Osuji, M. Maaza, F. Ezema, Optical, electrical and magnetic properties of copper doped electrodeposited MoO₃ thin films, *Ceram. Int.* 46 (2020) 10820–10828. <https://doi.org/10.1016/j.ceramint.2020.01.093>.
- [68] A. Boukhachem, M. Mokhtari, N. Benameur, A. Ziouche, M. Martínez, P. Petkova, M. Ghamnia, A. Cobo, M. Zergoug, M. Amlouk, Structural optical magnetic properties of Co doped α -MoO₃ sprayed thin films, *Sensors Actuators, A Phys.* 253 (2017) 198–209. <https://doi.org/10.1016/j.sna.2016.11.032>.
- [69] B.A. Davis, B. Chakraborty, N. Kalarikkal, L.M. Ramaniah, Room temperature ferromagnetism in carbon doped MoO₃ for spintronic applications: A DFT study, *J. Magn. Magn. Mater.* 502 (2020) 166503. <https://doi.org/10.1016/j.jmmm.2020.166503>.
- [70] O. Kamoun, A. Boukhachem, S. Alleg, B. Jeyadevan, M. Amlouk, Physical study of nano-structured MoO₃ films codoped with cobalt and nickel in which there is a ferro-diamagnetic transition, *J. Alloys Compd.* 741 (2018) 847–854. <https://doi.org/10.1016/j.jallcom.2018.01.231>.
- [71] K. Mukai, T. Inoue, Magnetic susceptibility measurements on Li-intercalated graphite: Paramagnetic to diamagnetic transitions in C₁₂Li induced by magnetic field, *Carbon N. Y.* 123 (2017) 645–650. <https://doi.org/10.1016/j.carbon.2017.08.012>.
- [72] J. Barzola-Quiquia, M. Stiller, P.D. Esquinazi, A. Molle, R. Wunderlich, S. Pezzagna, J. Meijer, W. Kossack, S. Buga, Unconventional Magnetization below 25 K in Nitrogen-doped Diamond provides hints for the existence of Superconductivity and

- Superparamagnetism, *Sci. Rep.* 9 (2019) 1–15. <https://doi.org/10.1038/s41598-019-45004-6>.
- [73] C. Rivera-Cárcamo, C. Scarfiello, A.B. García, Y. Tison, H. Martinez, W. Baaziz, O. Ersen, C. Le Berre, P. Serp, Stabilization of Metal Single Atoms on Carbon and TiO₂ Supports for CO₂ Hydrogenation: The Importance of Regulating Charge Transfer, *Adv. Mater. Interfaces* 8 (2021) 1–17. <https://doi.org/10.1002/admi.202001777>.
- [74] S.W. Han, Y. Park, Y.H. Hwang, S. Jekal, M. Kang, W.G. Lee, W. Yang, G. Do Lee, S.C. Hong, Electron beam-formed ferromagnetic defects on MoS₂ surface along 1 T phase transition, *Sci. Rep.* 6 (2016) 4–11. <https://doi.org/10.1038/srep38730>.
- [75] G.S. Zakharova, C. Täschner, V.L. Volkov, I. Hellmann, R. Klingeler, A. Leonhardt, B. Büchner, MoO_{3-δ} nanorods: Synthesis, characterization and magnetic properties, *Solid State Sci.* 9 (2007) 1028–1032. <https://doi.org/10.1016/j.solidstatesciences.2007.07.022>.
- [76] A. Chithambararaj, N. Rajeswari Yogamalar, A.C. Bose, Hydrothermally Synthesized h-MoO₃ and α-MoO₃ Nanocrystals: New Findings on Crystal-Structure-Dependent Charge Transport, *Cryst. Growth Des.* 16 (2016) 1984–1995. <https://doi.org/10.1021/acs.cgd.5b01571>.
- [77] A.C. Bararaj, D.B. Mathi, N.R. Yogamalar, A.C. Bose, Structural evolution and phase transition of [NH₄]₆Mo₇O₂₄·4H₂O to 2D layered MoO_{3-x}, *Mater. Res. Express* 2 (2015) 1–10. <https://doi.org/10.1088/2053-1591/2/5/055004>.
- [78] I. de Castro Silva, A.C. Reinaldo, F.A. Sigoli, I.O. Mazali, Raman spectroscopy-in situ characterization of reversibly intercalated oxygen vacancies in α-MoO₃, *RSC Adv.* 10 (2020) 18512–18518. <https://doi.org/10.1039/d0ra01207f>.
- [79] J. Yang, X. Xiao, P. Chen, K. Zhu, K. Cheng, K. Ye, G. Wang, D. Cao, J. Yan, Creating oxygen-vacancies in MoO_{3-x} nanobelts toward high volumetric energy-density asymmetric supercapacitors with long lifespan, *Nano Energy* 58 (2019) 455–465. <https://doi.org/10.1016/j.nanoen.2019.01.071>.
- [80] Y. Hu, X. Liu, S. Xu, W. Wei, G. Zeng, H. Yuan, Q. Gao, J. Guo, M. Chao, E. Liang, Improving the Thermal Expansion and Capacitance Properties of MoO₃ by Introducing Oxygen Vacancies, *J. Phys. Chem. C* 125 (2021) 10817–10823. <https://doi.org/10.1021/acs.jpcc.1c02405>.
- [81] C.D.A. Lima, João Victor Barbosa Moura, Cleânio Luz-Lima, A.D.C. Maciel, L.I.M.

- Sinimbu, João F. Chaves, J.D.S. Oliveira, A.R. Syed, R.L. Sommer, A. Ghosh, C.L.R. Fragoso, M. Cremona, O. Baffa, J. Ferraz, Synthesis and magnetic characterization of iron-doped molybdenum trioxide (α -MoO₃:xFe), *Submetido Em J. Solid State Chem.* (2023).
- [82] C.D.A. Lima, T.C.V. de Carvalho, M.E.H. Maia da Costa, C. Luz-Lima, S.D.T. de Barros, J.V.B. Moura, Z.S. Viegas, Y.D.R. Machado, B.G. Silva, R.L. Sommer, A. Ghosh, J.F.D.F. Araujo, Influence of temperature and gas atmosphere on the thermal decomposition of (NH₄)₆Mo₇O₂₄.4H₂O, *Solid State Sci.* 153 (2024) 107557. <https://doi.org/10.1016/J.SOLIDSTATESCIENCES.2024.107557>.
- [83] Z. Zhang, W. Li, T.W. Ng, W. Kang, C.S. Lee, W. Zhang, Iron(II) molybdate (FeMoO₄) nanorods as a high-performance anode for lithium ion batteries: Structural and chemical evolution upon cycling, *J. Mater. Chem. A* 3 (2015) 20527–20534. <https://doi.org/10.1039/c5ta05723j>.
- [84] G.D. Park, S.H. Choi, Y.C. Kang, Electrochemical properties of ultrafine TiO₂-doped MoO₃ nanoplates prepared by one-pot flame spray pyrolysis, *RSC Adv.* 4 (2014) 17382–17386. <https://doi.org/10.1039/c4ra01780c>.
- [85] T.G. Oliveira, Y. Guerra, S. Araujo-Barbosa, S.B.S. Gusmão, A.O. Lobo, E.C. Silva-Filho, F.E.P. Santos, R. Peña-García, B.C. Viana, Titanate nanotubes and their magnetic properties: Effect of ion exchange and calcination temperature, *J. Mater. Res.* (2023) 1–17. <https://doi.org/10.1557/s43578-023-00893-2>.
- [86] Z. Yang, D. Gao, J. Zhang, Q. Xu, S. Shi, K. Tao, D. Xue, Realization of high Curie temperature ferromagnetism in atomically thin MoS₂ and WS₂ nanosheets with uniform and flower-like morphology, *Nanoscale* 7 (2015) 650–658. <https://doi.org/10.1039/c4nr06141a>.
- [87] S.W. Han, Y. Park, Y.H. Hwang, S. Jekal, M. Kang, W.G. Lee, W. Yang, G. Do Lee, S.C. Hong, Electron beam-formed ferromagnetic defects on MoS₂ surface along 1 T phase transition, *Sci. Rep.* 6 (2016) 4–11. <https://doi.org/10.1038/srep38730>.
- [88] C. Rivera-Cárcamo, C. Scarfiello, A.B. García, Y. Tison, H. Martínez, W. Baaziz, O. Ersen, C. Le Berre, P. Serp, Stabilization of Metal Single Atoms on Carbon and TiO₂ Supports for CO₂ Hydrogenation: The Importance of Regulating Charge Transfer, *Adv. Mater. Interfaces* 8 (2021). <https://doi.org/10.1002/admi.202001777>.
- [89] S. Kumar, Y.J. Kim, B.H. Koo, C.G. Lee, Structural and magnetic properties of Ni doped

- CeO₂ nanoparticles, *J. Nanosci. Nanotechnol.* 10 (2010) 7204–7207. <https://doi.org/10.1166/jnn.2010.2751>.
- [90] A. Klinbumrung, T. Thongtem, S. Thongtem, Characterization of orthorhombic α -MoO₃ microplates produced by a microwave plasma process, *J. Nanomater.* (2012). <https://doi.org/10.1155/2012/930763>.
- [91] L. Mai, B. Hu, W. Chen, Y. Qi, C. Lao, R. Yang, Y. Dai, Z.L. Wang, Lithiated MoO₃ nanobelts with greatly improved performance for lithium batteries, *Adv. Mater.* (2007). <https://doi.org/10.1002/adma.200700883>.
- [92] L. Kihlberg, least squares refinement of the structure of Mo₁₇O₄₇, *Acta Chem. Scand.* 19 (1963) 760–762. <https://doi.org/10.3891/acta.chem.scand.19-0760>.
- [93] K. Seevakan, A. Manikandan, P. Devendran, S.A. Antony, T. Alagesan, One-Pot Synthesis and Characterization Studies of Iron Molybdenum Mixed Metal Oxide (Fe₂(MoO₄)₃) Nano-Photocatalysts, *Adv. Sci. Eng. Med.* 8 (2016) 566–572. <https://doi.org/10.1166/ asem.2016.1884>.
- [94] M. Merkelbach, E. Kemp, R. To, T.H.E. Public, K. Eichensehr, T.C. Morphology, T.S. Council, B. Cohen, I. Lee, International Committee of the Red Cross, THE CRYSTAL STRUCTURE AND TWINNING BEHAVIOR OF FERRIC MOLYBDATE, Fe₂(MoO₄)₃, VA. *J. Int. Law* 15 (1979) 1–50. <https://ssrn.com/abstract=1148799> <https://www.eisf.eu/library/duty-of-care-a-review-of-the-dennis-v-norwegian-refugee-council-ruling-and-its-implications/>.
- [95] C. Wan, B.M. Leonard, Iron-Doped Molybdenum Carbide Catalyst with High Activity and Stability for the Hydrogen Evolution Reaction, *Chem. Mater.* 27 (2015) 4281–4288. <https://doi.org/10.1021/acs.chemmater.5b00621>.
- [96] H. Xian, H. Guo, J. Xia, Q. Chen, Y. Luo, R. Song, T. Li, E. Traversa, Iron-Doped MoO₃ Nanosheets for Boosting Nitrogen Fixation to Ammonia at Ambient Conditions, *ACS Appl. Mater. Interfaces* 13 (2021) 7142–7151. <https://doi.org/10.1021/acsami.0c19644>.
- [97] L. Guo, L. Cao, J. He, J. Huang, Y. Wang, J. Li, K. Kajiyoshi, S. Chen, Inducing [100]-orientated plate-like α -MoO₃ to achieve regularly exfoliated layer structure enhancing Li storage performance, *J. Mater. Sci. Mater. Electron.* 32 (2021) 3006–3018. <https://doi.org/10.1007/s10854-020-05052-5>.

- [98] B. Gowtham, V. Ponnuswamy, G. Pradeesh, J. Chandrasekaran, D. Aradhana, MoO₃ overview: hexagonal plate-like MoO₃ nanoparticles prepared by precipitation method, *J. Mater. Sci. Mater. Electron.* 29 (2018) 6835–6843. <https://doi.org/10.1007/s10854-018-8670-7>.
- [99] C.Y. Chot, M.N. Chong, A.K. Soh, K.W. Tan, J.D. Ocon, C. Saint, Facile synthesis and characterisation of functional MoO₃ photoanode with self-photorechargeability, *J. Alloys Compd.* 838 (2020) 155624. <https://doi.org/10.1016/j.jallcom.2020.155624>.
- [100] A.M. Tamboli, M.S. Tamboli, P.K. Dwivedi, C.S. Praveen, I. Karbhal, M. V. Shelke, B. Kim, C. Park, B.B. Kale, Engineering microstructure of LiFe(MoO₄)₂ as an advanced anode material for rechargeable lithium-ion battery, *J. Mater. Sci. Mater. Electron.* 32 (2021) 24273–24284. <https://doi.org/10.1007/s10854-021-06892-5>.
- [101] E. Söderhjelm, M.P. House, N. Cruise, J. Holmberg, M. Bowker, J.O. Bovin, A. Andersson, On the synergy effect in MoO₃-Fe₂(MoO₄)₃ catalysts for methanol oxidation to formaldehyde, *Top. Catal.* 50 (2008) 145–155. <https://doi.org/10.1007/s11244-008-9112-1>.
- [102] M. Dieterle, G. Weinberg, G. Mestl, Raman spectroscopy of molybdenum oxides - Part I. Structural characterization of oxygen defects in MoO_{3-x} by DR UV/VIS, Raman spectroscopy and X-ray diffraction, *Phys. Chem. Chem. Phys.* 4 (2002) 812–821. <https://doi.org/10.1039/b107012f>.
- [103] L.O. Alemán-Vázquez, E. Torres-García, J.R. Villagómez-Ibarra, J.L. Cano-Domínguez, Effect of the particle size on the activity of MoO_x C_y catalysts for the isomerization of heptane, *Catal. Letters* 100 (2005) 219–226. <https://doi.org/10.1007/s10562-004-3459-0>.
- [104] T. Siciliano, A. Tepore, E. Filippo, G. Micocci, M. Tepore, Characteristics of molybdenum trioxide nanobelts prepared by thermal evaporation technique, *Mater. Chem. Phys.* 114 (2009) 687–691. <https://doi.org/10.1016/j.matchemphys.2008.10.018>.
- [105] G. Mestl, N.F.D. Verbruggen, E. Bosch, H. Knözinger, Mechanically activated MoO₃. 5. Redox behavior, *Langmuir* 12 (1996) 2961–2968. <https://doi.org/10.1021/la950788c>.
- [106] Z. Li, Y. Li, E. Zhan, N. Ta, W. Shen, Morphology-controlled synthesis of α-MoO₃ nanomaterials for ethanol oxidation, *J. Mater. Chem. A* 1 (2013) 15370–15376. <https://doi.org/10.1039/c3ta13402d>.
- [107] T.C. Xiao, A.P.E. York, H. Al-Megren, C. V. Williams, H.T. Wang, M.L.H. Green,

- Preparation and characterisation of bimetallic cobalt and molybdenum carbides, *J. Catal.* 202 (2001) 100–109. <https://doi.org/10.1006/jcat.2001.3247>.
- [108] S. Jiebing, X. Rui, W. Shimin, T. Wufeng, T. Hua, S. Jing, Preparation and characterization of molybdenum oxide thin films by sol-gel process, *J. Sol-Gel Sci. Technol.* 27 (2003) 315–319. <https://doi.org/10.1023/A:1024021003825>.
- [109] A. Nirmal Paul Raj, R. Biju Bennie, C. Joel, S. Hari Kengaram, S. Daniel Abraham, Systematic analysis and the effect of Mn doping on structural, optical and magnetic properties of MoO₃ nanoparticles, *Solid State Commun.* 341 (2022). <https://doi.org/10.1016/j.ssc.2021.114532>.
- [110] S. Malo, A. Maignan, S. Marinel, M. Hervieu, K.R. Poeppelmeier, B. Raveau, Structural and magnetic properties of the solid solution ($0 \leq x \leq 1$) YMn_{1-x}(Cu_{3/4}Mo_{1/4})_xO₃, *Solid State Sci.* 7 (2005) 1492–1499. <https://doi.org/10.1016/j.solidstatesciences.2005.07.003>.
- [111] F.C. Coomer, E.J. Cussen, Structural and magnetic study of order-disorder behavior in the double perovskites Ba₂Nd_{1-x}Mn_xMoO₆, *Inorg. Chem.* 53 (2014) 746–755. <https://doi.org/10.1021/ic4017799>.
- [112] K. SAILAKSHMI, B. RAMESH, A.D.P. RAO, P.R.M. RAO, S.B. RAJU, Effect of Sb⁵⁺/Mo⁶⁺ On Magnetic properties of Mn-Zn Ferrites, *J. Magn. Soc. Japan* 22 (1998) S1_37-39. https://doi.org/10.3379/jmsjmag.22.S1_37.
- [113] H.-K. Fun, P. Yang, M. Sasaki, M. Inoue, H. Kadomatsu, Rietveld refinement of the crystal structure of y-Mo 4O₁₁, *Int. Tab* 3 (1999) 284–288.
- [114] B.H. Toby, R.B. Von Dreele, GSAS-II: The genesis of a modern open-source all purpose crystallography software package, *J. Appl. Crystallogr.* 46 (2013) 544–549. <https://doi.org/10.1107/S0021889813003531>.
- [115] R. Benchrif, R. De Pape, Isotypism of the triclinic Ti₈Mo₁₀O₃₄ and (NH₄)₈Mo₁₀O₃₄ molybdates, *Acta Crystallogr. Sect. C* 46 (1990) 728–728. <https://doi.org/10.1107/S0108270189013284>.
- [116] R.D.P. R. BENCHRIFA, M. LEBLANC, Synthesis and crystal structure of two polymorphs of (NH₄)₂Mo₄O₁₃, orthorhombic (o) and triclinic (t), (1989) 1989.
- [117] H. Sitepu, B.H. O'Connor, D. Li, Comparative evaluation of the March and generalized spherical harmonic preferred orientation models using X-ray diffraction data for molybdate and calcite powders, *J. Appl. Crystallogr.* 38 (2005) 158–167.

<https://doi.org/10.1107/S0021889804031231>.

- [118] D.B. Rogers, R.D. Shannon, A.W. Sleight, J.L. Gillson, Crystal chemistry of metal dioxides with rutile-related structures, *Inorg. Chem.* 8 (1969) 841–849. <https://doi.org/10.1021/ic50074a029>.
- [119] A. Magnéli, G. Andersson, G. Sundkvist, G. Sundkvist, On the MoO₂ Structure Type., *Acta Chem. Scand.* 9 (1955) 1378–1381. <https://doi.org/10.3891/acta.chem.scand.09-1378>.
- [120] J. Zhang, D.M. Zhang, R.R. Zhang, Temperature-dependent Raman spectroscopic study of ferroelastic K₂Sr(MoO₄), *Chinese Phys. B* 27 (2018). <https://doi.org/10.1088/1674-1056/27/11/117801>.
- [121] C.L. Huang, C.C. Tsai, M.H. Tsai, W.C. Huang, High-Q Li₂Mg₂(MoO₄)₃ dielectrics for LTCC applications at microwave frequencies, *J. Asian Ceram. Soc.* 8 (2020) 430–436. <https://doi.org/10.1080/21870764.2020.1749374>.
- [122] P. Saha, A.J. Anderson, T. Lee, M. Klemm, The Solubility of Tugarinovite (MoO₂) in H₂O at Elevated Temperatures and Pressures, *Geofluids* 2017 (2017). <https://doi.org/10.1155/2017/5459639>.
- [123] L. Kumari, Y.R. Ma, C.C. Tsai, Y.W. Lin, S.Y. Wu, K.W. Cheng, Y. Liou, X-ray diffraction and Raman scattering studies on large-area array and nanobranched structure of 1D MoO₂ nanorods, *Nanotechnology* 18 (2007). <https://doi.org/10.1088/0957-4484/18/11/115717>.
- [124] M. Kumar Trivedi, Rama Mohan Tallapragada, Alice Branton, Dahryn Trivedi, Gopal Nayak, Omprakash Latiyal, Snehasis Jana, Analysis of Physical, Thermal, and Structural Properties of Biofield Energy Treated Molybdenum Dioxide, *Int. J. Mater. Sci. Appl.* 4 (2015) 354. <https://doi.org/10.11648/j.ijmsa.20150405.21>.
- [125] L. Seifikar Gomi, M. Afsharpour, Porous MoO₃@SiC hollow nanosphere composite as an efficient oxidative desulfurization catalyst, *Appl. Organomet. Chem.* 33 (2019) 1–9. <https://doi.org/10.1002/aoc.4830>.
- [126] G. Alnagar, R.K. Ramesh, S. Ananda, Electrochemical Synthesis of Large Area MoO₂ Nanosheets and their Photocatalytic Activity, *Asian J. Chem.* 31 (2019) 360–366. <https://doi.org/10.14233/ajchem.2019.21751>.
- [127] M. Ghorbanloo, A.M. Alamooti, Encapsulation of molybdenum(VI) complex with thiazole-hydrazone ligand in zeolite Y: an efficient reusable catalyst for oxidation of

- primary alcohols and hydrocarbons, *J. Porous Mater.* 24 (2017) 769–777. <https://doi.org/10.1007/s10934-016-0314-9>.
- [128] C.D.A. Lima, T.C.V. de Carvalho, C.D. Mendoza, M.E.H. Maia da Costa, G. de S. Pinheiro, C. Luz-Lima, B.G. Silva, R.L. Sommer, J.F.D.F. Araujo, Magnetic transition in MoO₃: Influence of Mo⁵⁺/Mo⁶⁺ ratios on paramagnetic to diamagnetic behavior, *Solid State Sci.* 162 (2025). <https://doi.org/10.1016/j.solidstatesciences.2025.107866>.
- [129] L. Barkat, M. Hssein, Z. El Jouad, L. Cattin, G. Louarn, N. Stephant, A. Khelil, M. Ghamnia, M. Addou, M. Morsli, J.C. Bernède, Efficient hole-transporting layer MoO₃:CuI deposited by co-evaporation in organic photovoltaic cells, *Phys. Status Solidi Appl. Mater. Sci.* 214 (2017). <https://doi.org/10.1002/pssa.201600433>.
- [130] V. Sannasi, P. Thangasamy, J.A. Raj, M. Sathish, Transformation of sluggish higher valent molybdenum into electrocatalytically active amorphous carbon doped MoO₂/MoO₃-x nanostructures using phyllanthus reticulatus fruit extract as natural reducing agent in supercritical fluid processing, *Int. J. Hydrogen Energy* 44 (2019) 21692–21702. <https://doi.org/10.1016/j.ijhydene.2019.06.123>.
- [131] S.K. Sen, M.R. Munshi, A. Kumar, A.A. Mortuza, M.S. Manir, M.A. Islam, M.N. Hossain, M.K. Hossain, Structural, optical, magnetic, and enhanced antibacterial properties of hydrothermally synthesized Sm-incorporating α -MoO₃ 2D-layered nanoplates, *RSC Adv.* 12 (2022) 34584–34600. <https://doi.org/10.1039/d2ra05304g>.
- [132] W.D. Callister JR, D.G. Rethwisch, *Material Science and Engineering: An introduction* Chapter 20 Magnetic Properties, (2018) W19–W56.
- [133] A. Mittal, I. Roy, S. Gandhi, *Magnetic Nanoparticles : An Overview for Biomedical Applications*, (2022).

7 Appendix

Appendix A: Raman

Raman spectroscopy is a high-resolution photon-based method that serves to decipher the chemical and structural composition of materials by emitting monochromatic light that scatters upon reaching a sample, generating light of either identical or differing energy levels compared to the incident light. The two types of scattering—elastic and inelastic—offer distinct insights into the sample. Elastic scattering lacks compositional data, while inelastic scattering, particularly through energy level discrepancies, provides crucial details regarding the sample's chemical composition. This energy variation between incident and scattered radiation is linked to the vibrational energy of atoms, revealing intricate information about atomic bonding, molecular structure, and interactions among various chemical species.

Initially verified by the Indian physicist Chandrasekhara Venkata Raman and his associate Krishnam in 1928, this discovery earned Raman the Nobel Prize in Physics in 1930. Raman spectroscopy is rooted in the inelastic scattering of light, related to the induced dipole moment through the electric field of the radiation, functioning as a perturbing system. Beyond presenting the sample's vibrational spectrum, it uncovers rotational spectra and other low-frequency modes within the system.

Photon dispersion onto the sample molecule occurs through three avenues: Rayleigh scattering, Stokes scattering, and anti-Stokes scattering. While Rayleigh scattering, an elastic process, doesn't offer sample information, the latter two, as inelastic processes, provide insights into molecular composition. Variances in frequency $\nu = \nu_0 + \nu_r$ and $\nu = \nu_0 - \nu_r$ correspond to Raman Stokes and Raman anti-Stokes scattering, respectively. The scattered light with wavenumbers different from the incident radiation $\nu = \nu_0 \pm \nu_r$ reveals information about molecular composition, with each material possessing characteristic ν_r values rooted in its polyatomic structure and chemical interactions. Figure A1 presents a schematic illustration of Rayleigh, Stokes and Anti-Stokes Raman scattering.

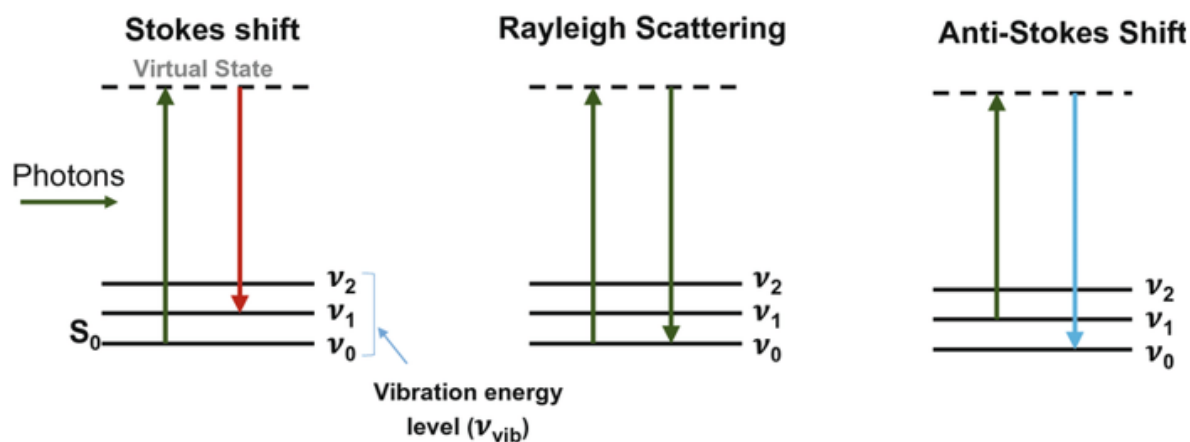


Figure A1: Graphical Representation of Raman scattering. Adapted from [1].

Within the Raman spectrum, information is obtained from vibrational changes often associated with the infrared range, while rotational transitions are typically linked to the microwave region. The x-axis displays the displacement of Raman wavenumbers concerning the incident wavenumber ν_0 , with the Rayleigh band center as the origin, while the y-axis represents Raman intensity. In Figure 5, the text highlights the greater intensity of Raman Stokes scattering compared to Raman anti-Stokes scattering, largely due to the prevalence of molecules existing in a lower vibrational energy state at room temperature. Consequently, the intensity of Raman Stokes scattering surpasses that of anti-Stokes scattering by around 100 times (Figure A2).

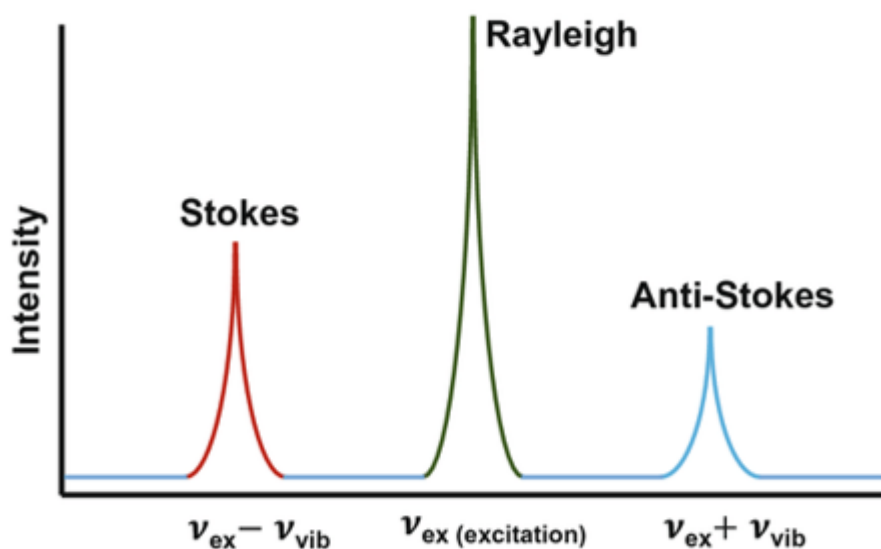


Figure A2: Graphical Representation of Raman pattern of Rayleigh, Stokes and Anti-Stokes scattering. Adapted from [1].

In classical electromagnetic radiation theory, oscillating electric and magnetic fields at a specific frequency can emit electromagnetic radiation of the same frequency. Electromagnetic radiation theory can be employed to explain light scattering phenomena. In most systems, only the induced electric dipole moment (μ) is typically considered. This dipole moment, induced by the electric field (E), can be expressed as a power series [1].

$$\mu = \mu^{(1)} + \mu^{(2)} + \mu^{(3)} + \dots \quad (1)$$

Where:

$$\mu^{(1)} = \alpha \cdot E \quad (2)$$

$$\mu^{(2)} = \frac{1}{2} \beta \cdot EE \quad (3)$$

$$\mu^{(3)} = \frac{1}{6} \gamma \cdot EEE \quad (4)$$

The polarizability tensor, designated as α , is a second-rank tensor. In most cases, the magnitudes of the components for α , β , and γ are insignificant unless the electric field is of an exceptionally strong intensity. Rayleigh and Raman scattering can be observed at considerably lower electric field intensities. These phenomena can typically be explained in terms of $\mu^{(1)}$ alone [1].

The interaction of a molecular system with a harmonically oscillating electric field at frequency ω_0 is now considered. To simplify the explanation, rotational motion is disregarded, focusing only on the vibrational aspect. The polarizability is expected to depend on the nuclear coordinates, and the variation of the polarizability tensor components with respect to the vibrational coordinates is expressed through a Taylor series expansion [1]:

$$\alpha_{ij} = (\alpha_{ij})_0 + \sum_k \left(\frac{\delta \alpha_{ij}}{\delta Q_k} \right)_0 Q_k + \frac{1}{2} \sum_{k,l} \left(\frac{\delta^2 \alpha_{ij}}{\delta Q_k \delta Q_l} \right)_0 Q_k Q_l + \dots \quad (5)$$

Here, $(\alpha_{ij})_0$ represents the value of α_{ij} at the equilibrium configuration, while Q_k and Q_l denote the normal vibrational coordinates at frequencies ω_k and ω_l , respectively. A harmonic approximation is applied, neglecting terms involving powers of Q higher than the first. By focusing on a single normal mode, Q_k , the resulting simplified expression can be derived [1].

$$\alpha_{ij} = (\alpha_{ij})_0 + \left(\frac{\delta\alpha_{ij}}{\delta Q_k}\right)_0 Q_k \quad (6)$$

As for a harmonic vibration,

$$Q_k = Q_{k0} \cos(\omega_k t + \delta_k) \quad (7)$$

The expression for the α tensor resulting from the k-th vibration can then be derived [1].

$$\alpha_k = \alpha_0 + \left(\frac{\delta\alpha_k}{\delta Q_k}\right)_0 Q_{k0} \cos(\omega_k t + \delta_k) \quad (8)$$

The induced electric dipole moment $\mu^{(1)}$ is expressed as a function of electromagnetic radiation at frequency ω_0 and its associated frequency ω_k , as follows [1]:

$$\begin{aligned} \mu^{(1)} = \alpha_k \cdot \mathbf{E}_0 \cos(\omega_0 t) &= \alpha_0 \cdot \mathbf{E}_0 \cos(\omega_0 t) + \left(\frac{\delta\alpha_k}{\delta Q_k}\right)_n \cdot \mathbf{E}_0 Q_{k0} \cos \omega_0 t (\omega_k t + \delta_k) t = \\ &\alpha_0 \cdot \mathbf{E}_0 \cos(\omega_0 t) + \frac{1}{2} \left(\frac{\delta\alpha_k}{\delta Q_k}\right)_n \cdot \mathbf{E}_0 Q_{k0} \cos(\omega_0 t + \omega_k t + \delta_k) + \frac{1}{2} \left(\frac{\delta\alpha_k}{\delta Q_k}\right)_n \cdot \\ &\mathbf{E}_0 Q_{k0} \cos(\omega_0 t - \omega_k t - \delta_k) \end{aligned} \quad (9)$$

The linear induced dipole moment $\mu^{(1)}$ comprises three components with different frequencies. The term $\alpha_0 \cdot \mathbf{E}_0 \cos(\omega_0 t)$ corresponds to radiation at frequency ω_0 and accounts for Rayleigh scattering [1].

$$\frac{1}{2} \left(\frac{\delta\alpha_k}{\delta Q_k}\right)_0 \cdot \mathbf{E}_0 Q_{k0} \cos(\omega_0 t + \omega_k t + \delta_k) \quad (10)$$

This phenomenon gives rise to radiation at $\omega_0 + \omega_k$, which accounts for anti-Stokes Raman scattering. Similarly, it gives rise to radiation at $\omega_0 - \omega_k$, which accounts for Stokes Raman scattering [1].

$$\frac{1}{2} \left(\frac{\delta\alpha_k}{\delta Q_k}\right)_0 \cdot \mathbf{E}_0 Q_{k0} \cos(\omega_0 t - \omega_k t - \delta_k). \quad (11)$$

Appendix B: XRD

1. Crystal Geometry

Crystals are solids composed of atoms, ions, or molecules arranged in a periodic and ordered three-dimensional structure. This ordered arrangement allows crystals to act as diffraction gratings for X-rays, making them essential for identifying crystalline substances. The study of crystal geometry is fundamental to understanding how X-ray diffraction (XRD) works.

- **Crystal Lattice and Unit Cell:** The crystal lattice is a mathematical representation of the periodic arrangement of points in space, while the unit cell is the smallest repeating unit that defines the crystal structure. The unit cell is characterized by its dimensions along the crystallographic axes (a , b , c) and the angles (α , β , γ) between these axes, known as lattice parameters.

- **Crystal Systems:** There are seven crystal systems, each defined by unique lattice parameters and symmetry:

1. Cubic: $a=b=c$, $\alpha=\beta=\gamma=90^\circ$
2. Tetragonal: $a=b \neq c$, $\alpha=\beta=\gamma=90^\circ$
3. Orthorhombic: $a \neq b \neq c$, $\alpha=\beta=\gamma=90^\circ$
4. Trigonal/Rhombohedral: $a=b=c$, $\alpha=\beta=\gamma \neq 90^\circ$
5. Hexagonal: $a=b \neq c$, $\alpha=\beta=90^\circ$, $\gamma=120^\circ$
6. Monoclinic: $a \neq b \neq c$, $\alpha=\gamma=90^\circ$, $\beta \neq 90^\circ$
7. Triclinic: $a \neq b \neq c$, $\alpha \neq \beta \neq \gamma \neq 90^\circ$

- **Bravais Lattices:** In 1848, Auguste Bravais demonstrated that there are 14 possible lattice types in three dimensions, known as Bravais lattices. These lattices are classified based on their centering: primitive (P), body-centered (I), face-centered (F), and base-centered (C).

2. Crystal Planes and Miller Indices

Crystal planes are defined by their intercepts with the crystallographic axes. The orientation of these planes is described using Miller Indices, which are a set of integers (hkl) derived from the reciprocals of the intercepts of the plane with the axes.

- **Weiss Parameters:** The intercepts of a plane with the crystallographic axes are initially described using Weiss parameters. However, these parameters can result in fractional or infinite values, making them impractical for representation.

- **Miller Indices:** Miller Indices simplify the representation of crystal planes by using integers. For example, a plane with intercepts at $1/2a$, $1/3b$, and $1/4c$ would have Miller Indices of (2 3 4). A plane parallel to an axis has a Miller Index of 0 for that axis.

- **Interplanar Distance:** The distance between parallel crystal planes, known as the interplanar distance (d), is crucial for X-ray diffraction. For cubic crystals, the interplanar distance can be calculated using the formula:

$$d = \frac{a}{\sqrt{h^2 + k^2 + l^2}} \quad (12)$$

where a is the lattice parameter, and h, k, l are the Miller Indices.

3. Principles of X-ray Diffraction (XRD)

X-ray diffraction (XRD) is a non-destructive technique that is employed to analyse a range of material properties, including phase composition, structure, and texture, in powder, solid, or liquid samples. Phase identification is achieved by comparing the XRD pattern of an unknown sample with reference patterns from a database, in a manner analogous to the matching of fingerprints in criminal investigations. Alternatively, a bespoke database can be constructed using experimental diffraction patterns of pure phases, published data, or measurements from individual studies.

The primary subjects of X-ray diffraction encompass qualitative and quantitative phase analysis of both pure substances and mixtures, in addition to the examination of the impact of temperature and other non-ambient factors, such as humidity or applied pressure, on materials. Furthermore, the analysis of the microstructure of materials is undertaken, with particular attention paid to crystallite size, preferred orientation effects, and residual stress in polycrystalline

engineered materials. X-ray powder diffraction is a technique that is widely applied in both research and process control environments. For instance, it is employed in academic institutions and research facilities for the characterization of novel materials, and in industries such as construction, chemicals, and pharmaceuticals for process control, including phase composition and content analysis. Furthermore, it is utilized for phase identification in geological samples, the optimization of fabrication parameters for wear-resistant ceramics and biomaterials, the assessment of crystallinity in phases, and the measurement of amorphous phase contents in mixtures.

X-rays were discovered in 1895 by Wilhelm Conrad Roentgen during his investigation of cathode rays emitted from a Crookes tube. Roentgen observed that an invisible type of radiation caused a fluorescent screen to glow, which he subsequently termed "X-radiation." In 1913, Lawrence Bragg and his father, William Henry Bragg, introduced the concept that constructive interference occurs when X-rays scatter off planes within crystalline materials, producing a characteristic diffraction pattern now known as Bragg's diffraction [3]. This phenomenon arises because the wavelength of X-rays is on the same order of magnitude as the interplanar spacing within the crystal. X-rays are a form of electromagnetic radiation, defined by their wavelength, or alternatively, as beams of photons with specific energies. The wavelength range of X-rays is from 0.01 nm to 10 nm, corresponding to energies between 0.125 keV and 125 keV (Figure A3).

The energy (E) of X-rays is defined by Planck's equation and is directly proportional to the frequency (f), as expressed by the formula [3]:

$$E = hf \quad (13)$$

where h is Planck's constant (approximately 6.626×10^{-34} J·s).

Additionally, using equation $f = c/\lambda$,

$$E = \frac{hc}{\lambda} \quad (14)$$

Where E is photon energy, λ is the photon's wavelength, c is the speed of light in a vacuum, and h is the Planck constant.

Due to the regular atomic arrangement in solid matter, coherent scattering of X-rays by atoms leads to constructive interference at specific, well-defined angles. This phenomenon resembles the diffraction of visible light by gratings with nanometer-scale spacing comparable to the light's wavelength (Figure A4). In this context, a crystal can be regarded as a three-dimensional grating with atomic spacing on the order of a few Å, enabling diffraction effects to occur when the wavelength of the incident X-ray photons is of comparable magnitude.

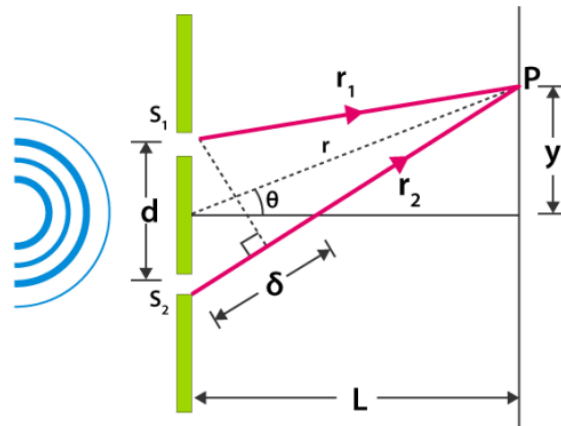


Figure A3: Visualization of the double-slit experiment. Figure taken from: [3].

Bragg proposed that the diffraction and interference of X-rays in a crystal can be understood as reflections occurring at the atomic planes within the crystal lattice. The positions of these reflections are determined by calculating the optical path difference, $2s$ ($s = d \sin(\theta)$), between two rays reflected from adjacent interplanar spacings, where s is the distance between the two rays and θ is the angle of incidence. As with the behavior observed in visible light optics, intensity maxima are observed when the path difference is an integer multiple of the wavelength, λ [3].

It follows:

$$2d \sin(\theta) = n\lambda \quad (15)$$

Here, d represents the interplanar spacing, denoted as d_{hkl} (where hkl are the Miller indices). The angle θ is the Bragg angle, 2θ representing the angle between the incident and reflected beams. The term n denotes the "order" of the interference, where $n = 1, 2, 3, \dots$, with $n=1$ commonly referred to as the "first-order reflection." Finally, λ represents the wavelength of the X-rays.

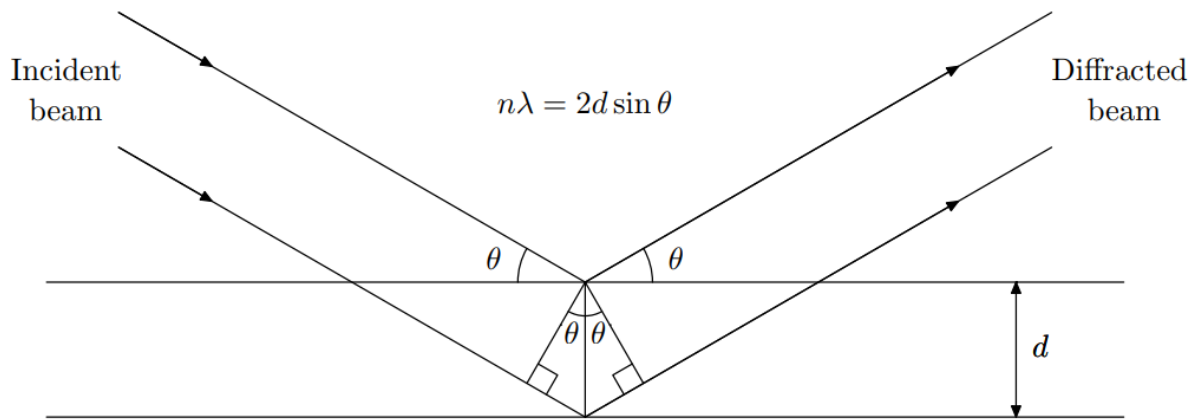


Figure A4: Graphical representation of Bragg's law. Figure taken from: [4].

A powder diffraction pattern presents the scattered intensity as a function of the Bragg angle (2θ) and displays multiple peaks, or reflections. The aforementioned peaks are distinguished by their position, and intensity, thereby furnishing indispensable data for analysis. In X-ray powder diffraction, both the peaks and the background signal serve as the primary sources of information. The peak positions, influenced by the periodic atomic arrangement and the wavelength used, provide essential information for qualitative phase analysis, lattice parameters, and residual stress. Peak intensities, determined by the crystal structure, wavelength, and sample preparation, yield insights into quantitative phase analysis, crystal structure, and preferred orientations within the sample.

4. The Laue Experiment

The Laue experiment, conducted by Max von Laue in 1912, was the first experimental demonstration of X-ray diffraction by crystals. It confirmed the wave nature of X-rays and the periodic arrangement of atoms in crystals.

Experimental Setup: In the Laue experiment, a polychromatic X-ray beam (containing multiple wavelengths) is directed at a single crystal. The crystal diffracts the X-rays in specific directions, depending on the orientation of its atomic planes.

Laue Pattern: The diffracted X-rays are recorded on a photographic film or detector, producing a pattern of spots known as the Laue pattern. Each spot corresponds to a specific set of crystal planes that satisfy Bragg's Law for a particular wavelength.

Significance of the Laue Experiment: The Laue experiment provided the first direct evidence of: The wave nature of X-rays, the periodic arrangement of atoms in crystals, the potential of X-rays for studying crystal structures.

5. Key Points of X-ray Diffraction (XRD)

XRD is a cornerstone technique in materials science, chemistry, and physics. Here are some of the most important aspects of XRD:

Crystal Structure Determination: XRD is the primary method for determining the atomic arrangement in crystals. By analyzing the diffraction pattern, researchers can determine the unit cell dimensions, symmetry, and atomic positions.

Phase Identification: XRD is used to identify the phases present in a material. Each crystalline phase produces a unique diffraction pattern, allowing for the identification of unknown substances.

Quantitative Analysis: XRD can be used to quantify the relative amounts of different phases in a mixture. This is particularly useful in studying phase transformations and material purity.

Texture Analysis: XRD can reveal the preferred orientation of crystals in a material, known as texture. This is important in understanding the mechanical properties of materials, especially in metals and alloys.

Residual Stress Measurement: XRD can measure residual stresses in materials by analyzing changes in the interplanar distances. This is crucial for assessing the structural integrity of components in engineering applications.

Thin Film Analysis: XRD is used to study the structure and properties of thin films, including their thickness, crystallinity, and strain.

High-Resolution XRD: Advanced XRD techniques, such as high-resolution XRD, allow for the study of epitaxial layers, superlattices, and nanostructures with high precision.

The study of crystal geometry, the principles of X-ray diffraction, and the Laue experiment are fundamental to understanding the structure and properties of crystalline materials. XRD is an indispensable tool in materials science, enabling the determination of crystal structures, phase identification, and the analysis of material properties. The Laue experiment, in particular, marked the beginning of X-ray crystallography, paving the way for countless discoveries in science and technology. Today, XRD continues to be a vital technique for advancing our understanding of materials at the atomic level.

Appendix C: Magnetic properties

The magnetic force on a charged particle moving with velocity (v) in a magnetic field (B) is given by the Lorentz force law [132]:

$$F = q (v \times B) \quad (16)$$

where:

- F is the force on the particle,
- q is the charge of the particle,
- v is the velocity of the particle,
- B is the magnetic field.

The magnetic field (B) itself can be expressed in terms of the magnetic flux (Φ_B) through a surface area A [132]:

$$\Phi_B = \int_A B \cdot dA \quad (17)$$

where dA is an infinitesimal vector area element of the surface.

The magnetization (M) of a material is related to the magnetic field intensity (H) and the magnetic susceptibility (χ_m) by [132]:

$$M = \chi_m H \quad (18)$$

where:

- M is the magnetization (magnetic moment per unit volume),
- χ_m is the magnetic susceptibility (dimensionless),
- H is the magnetic field intensity.
- The magnetic field (B) inside a material is related to the magnetization (M) and the applied magnetic field intensity (H) by [132]:

$$B = \mu_0 (H + M) \quad (19)$$

where:

- B is the magnetic flux density,
- μ_0 is the permeability of free space.

For linear, non-magnetic materials, M is directly proportional to H , so we can write [132]:

$$B = \mu_0 (1 + \chi_m) H = \mu H \quad (20)$$

where μ is the magnetic permeability of the material [132]:

$$\mu = \mu_0 (1 + \chi_m) \quad (21)$$

In general, for linear magnetic materials where magnetization is proportional to the magnetic field, we have [132]:

$$M = \chi_m H \quad (22)$$

and the total magnetic field (B) is [132]:

$$B = \mu_0 (1 + \chi_m) H \quad (23)$$

where μ_0 is the permeability of free space, and χ_m is the magnetic susceptibility of the material.

Magnetic materials exhibit different types of magnetization depending on how their magnetic domains behave in response to an external magnetic field.

Ferromagnetism:

In an unmagnetized state, the material consists of multiple randomly oriented magnetic domains, canceling each other's effects. When an external field is applied, domains aligned with the field grow, while others shrink. With a strong enough field, the material becomes a single-domain state (saturation). Even after the field is removed, some domain alignment remains, resulting in permanent magnetization.

Ferrimagnetism:

Like ferromagnetic materials, ferrimagnetic materials also have well-defined domains. However, the magnetic moments in different sublattices are oppositely aligned but unequal, resulting in a net magnetization. They exhibit spontaneous magnetization but weaker than ferromagnets. Used in ferrites, which have high electrical resistance and low eddy current losses.

Antiferromagnetism:

In antiferromagnetic materials, magnetic domains exist, but neighboring atomic spins are aligned in opposite directions and cancel each other out. As a result, there is no net magnetization in the absence of an external field. When exposed to a field, weak magnetization can appear due to slight spin canting (weak ferromagnetism). Above the Néel temperature, antiferromagnetic materials become paramagnetic.

Paramagnetism:

No permanent magnetic domains exist in paramagnetic materials. Individual atomic magnetic moments are randomly oriented, leading to zero net magnetization. When an external field is applied, the atomic moments align weakly with the field, creating a small magnetization. Once the field is removed, they return to random orientations, losing their magnetization.

Diamagnetism:

No magnetic domains exist in diamagnetic materials. When exposed to an external field, they develop weak induced magnetic moments in the opposite direction of the field. This results in a very weak repulsion from the external magnet. The effect is present in all materials, but it is overshadowed by other forms of magnetism in ferro-, ferri-, and paramagnetic materials.

The vibrating sample magnetometer (VSM) is widely recognized as an effective and robust technique for measuring sample magnetization. Compared to alternative magnetometers, the VSM exhibits minimal sensitivity to sample mass and size over a significant range. In this method, a sample is placed in a uniform external magnetic field, resulting in induced magnetization within

the sample. vibration of the magnetized sample creates perturbations in the surrounding magnetic field. A series of coils or magnetic field sensors positioned around the sample detect these perturbations. In the case of coils, for example, changes in the magnetic flux through the coils generate an electromotive force (EMF) within the coils. For a given coil configuration, the EMF generated depends on amplitude and frequency of the vibration, external magnetic field, and the magnetization of the sample. By appropriately analyzing the EMF, the magnetization of the sample can be determined.

In a vibrating sample magnetometer (VSM), the sample is attached to one end of a rigid rod that allows a magnetic field to be applied either transverse or longitudinal to the direction of vibration. The opposite end of the rod is attached to the membrane of a vibrating system, which determines the vibration frequency of the sample. An amplifier is used to selectively amplify signals of a specific frequency and phase, greatly increasing the sensitivity of the measurement. The VSM is typically designed for magnetic field measurements at ambient temperature, but can be modified to facilitate measurements at low temperatures. Figure A6 shows a schematic diagram of vibrating sample magnetometer.

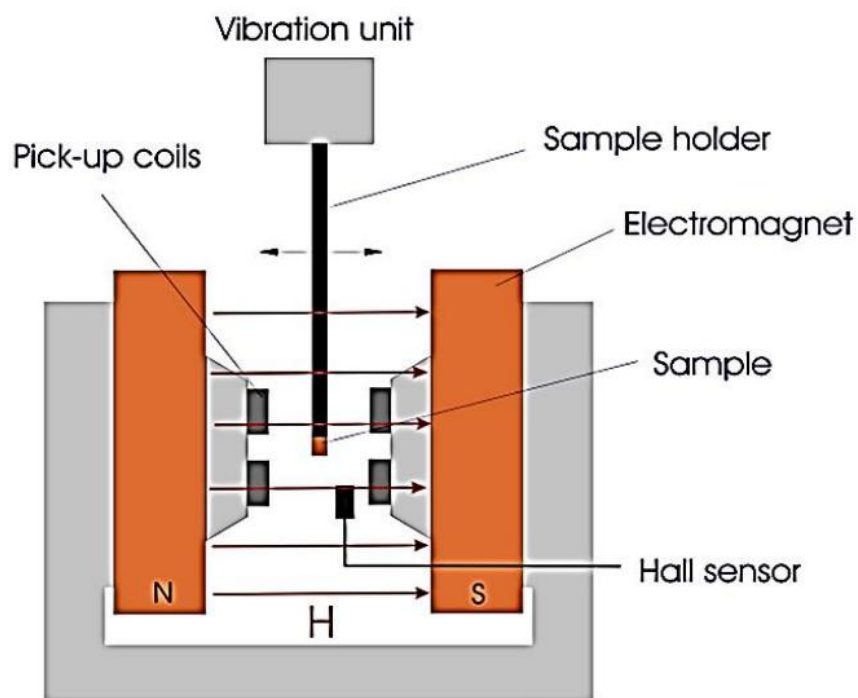


Figure A5: vibrating sample magnetometer Schematic diagram. Figure taken from: [5].

The data record the response of both the x- and y-axis coils as a function of the applied magnetic field at various angles (ψ) between the applied field and an initial arbitrary orientation (ψ_0) relative to the sample's easy axis of the sample. The $M_x(H_x)$ response demonstrates the

characteristic hysteresis loop typically seen in single-axis VSM measurements. In Value Stream Management (VSM), the X-axis typically displays the applied field in Oersted (Oe), while the Y-axis indicates the sample magnetization (emu).

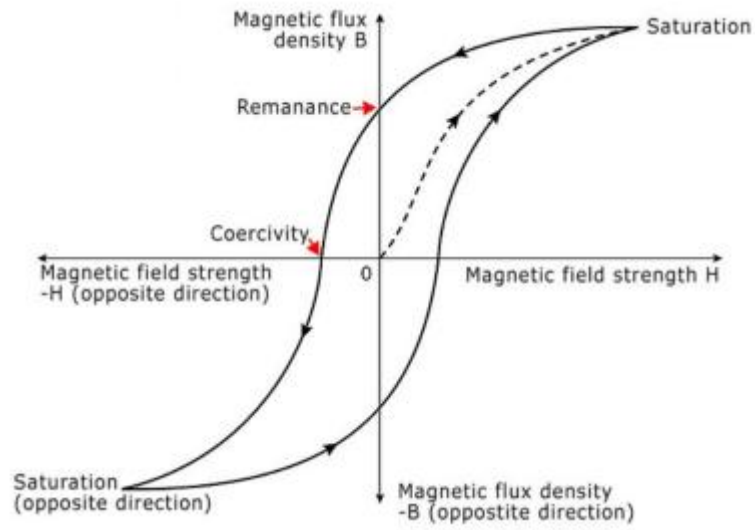


Figure A6: Typical hysteresis loop obtained by VSM. Figure taken from: [6].

Appendix D: XPS

X-ray Photoelectron Spectroscopy (XPS) is a surface-sensitive analytical technique that involves bombarding a material's surface with x-rays and measuring the kinetic energy of the emitted electrons. This method is particularly powerful due to two key features: its sensitivity to surface layers and its ability to provide chemical state information about the elements in the sample. In XPS, the sample is exposed to X-rays, and the kinetic energy of the emitted electrons is analyzed [Fig. A7(a)] [7]. The photoelectron emitted by this process, is a result of a transfer of X-ray to a core-level electron. Eq. (24) express this process [7]:

$$h\nu = BE + KE + \Phi_{\text{spec}} \quad (24)$$

($h\nu$) = the energy of the x-ray; (BE) = binding energy of the electron (representing how strongly it is bound to its atom or orbital); (KE) = kinetic energy (KE) of the electron that is emitted; (Φ_{spec}) = Spectrometer work function, which is a constant [7].

To calculate the binding energy of an electron, Eq. (24) can be rearranged to derive Eq. (25), where the terms ($h\nu$ and Φ_{spec}) are either known or measured during the XPS experiment (KE) [7]:

$$BE = -h\nu - KE - \Phi_{\text{spec}} \quad (25)$$

A picture of this concept is illustrated diagrammatically in Fig. A7(b).

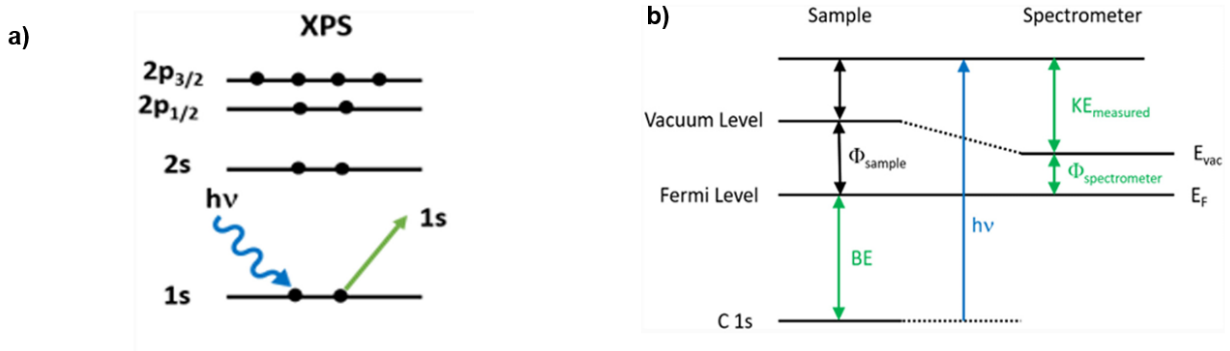


Figure A6: (a) Processes that results from photoelectron emission in XPS and (b) schematic of energy level diagram. Adapted from [7].

As a surface-sensitive technique, in XPS, it is essential to consider the physical processes affecting electrons traveling through solids. While the x-rays used in XPS can penetrate several micrometers into the sample, electrons generated at such depths undergo multiple inelastic collisions, losing energy until they can no longer escape the material. In A7(a), these deeply generated electrons are labeled “C”. Electrons produced closer to the surface may experience only one or two inelastic collisions before reaching the detector. As a result, they retain less kinetic energy than expected due to energy loss during travel. These electrons, labeled “B” in A7(a), contribute to the vertical step in the background signal observed in XPS spectra, as seen in Fig. A7(b) (shaded in orange). Only electrons that escape without any inelastic collisions contribute to the distinct photoelectron peaks used in XPS analysis (these electrons are labeled “A”) [7].

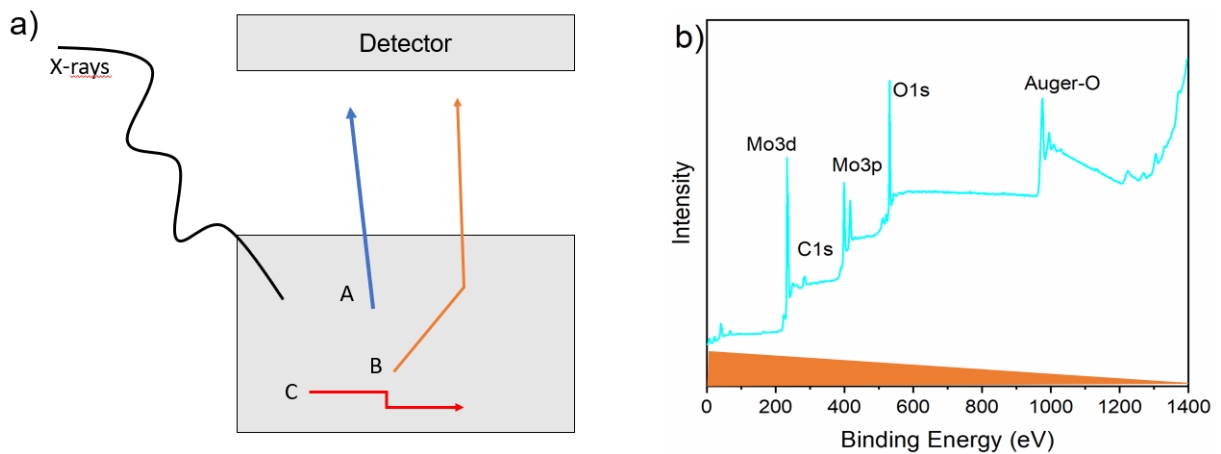


Figure A7: (a) Processes that results from photoelectron emission in XPS and (b) schematic of energy level diagram. Adapted from [7].

Appendix F: Additional References

- [1] Y.C. Cho, S. Il Ahn, Fabricating A Raman Spectrometer Using An Optical Pickup Unit And Pulsed Power, Sci. Rep. 10 (2020) 1–8. <https://doi.org/10.1038/S41598-020-68650-7>.
- [2] G.J. Verhoeven, The Reflection Of Two Fields – Electromagnetic Radiation And Its Role

- In (Aerial) Imaging, (2018) 10–18. <https://doi.org/10.5281/zenodo.3534245>.
- [3] A.M. Baraz, Double Slit Interference, (2022) 0–5. <https://doi.org/10.13140/Rg.2.2.16934.60485>.
- [4] T. Sochi, High Throughput Software For Powder Diffraction And Its Application To Heterogeneous Catalysis, 2010. <http://arxiv.org/abs/1012.4506>.
- [5] M. Rafique, Study Of The Magnetoelectric Properties Of Multiferroic Thin Films And Study Of The Magnetoelectric Properties Of Multiferroic Thin Films And Composites For Device Applications By CIIT / FA09-PPH-010 / ISB Phd Thesis In Physics COMSATS Institute Of Inform, 2014. <https://doi.org/10.13140/RG.2.2.23827.94245>.
- [6] V. Khemani, M.H. Azarian, M.G. Pecht, Efficient Identification Of Jiles–Atherton Model Parameters Using Space-Filling Designs And Genetic Algorithms, Eng 3 (2022) 364–372. <https://doi.org/10.3390/eng3030026>.
- [7] F. A. Stevie, C. L. Donley, Introduction to x-ray photoelectron spectroscopy, 2020. <https://doi.org/10.1116/6.0000412>.